/
Article / Book Information

( )	
Title(English)	Multi-point Wireless Energy Transmission to Realize Battery-less Sensor Networks
( )	
Author(English)	Daiki Maehara
( )	: ( ), : , : 10150 , :2016 3 26 , : , : , , , , ,
Citation(English)	Degree:Doctor (Engineering), Conferring organization: Tokyo Institute of Technology, Report number: 10150 , Conferred date:2016/3/26, Degree Type:Course doctor, Examiner:,,,,,
( )	
Type(English)	Doctoral Thesis

Doctoral Dissertation

Multi-point Wireless Energy Transmission to Realize Battery-less Sensor Networks

Supervisors   Associate Professor Kei Sakaguchi

Professor Makoto Ando

Department of Electrical and Electronic Engineering

Graduate School of Engineering

Tokyo Institute of Technology

Daiki Maehara

Contents

List of Figures

List of Tables

Abstract

Limited lifetime of sensor nodes has been a critical issue in WSNs (Wireless Sensor Networks). In WSNs, as numerous sensor nodes are deployed in a target field to perform specified applications, power-plugged or battery-powered sensors are not preferable due to their cost of power line installation or battery replacement. In recent years, sensor nodes activated via ambient energy become one of candidate solutions. However, such ambient energy can be easily influenced by its surrounding environments, which is hard to guarantee stable operation of WSNs. In contrast to conventional systems, this thesis employs microwave energy transmission to supply power to sensor nodes and proposes efficient transmission schemes. So far, the wireless energy transmission using microwave has been employed by RFID (Radio Frequency IDentification) systems. In these systems, Reader/Writers transmit microwave and receive information from ID tags activated by the energy of the microwave. In general, RFID systems employ single transmitter to avoid interference. As a result, the readability coverage is limited by the maximum allowable transmit power according to the radio regulation. With an extensive scope of seamless energy transmission to sensors distributed in indoor environment, a multi-point wireless energy transmission system named as wireless grid is constructed in this thesis. In this proposed wireless grid, a seamless coverage can be realized by the introduction of multiple transmitters together with a carrier shift diversity scheme employed to alleviate multi-point interferences. Beside theoretical analyses, the thesis also develops battery-less sensor nodes, conducts experimental investigation on the effectiveness of the proposed wireless energy transmission scheme in terms of both propagation characteristics as well as sensor activation capabilities and implements wireless grid to a real indoor environment. The experimental results and the system implementation show that the proposed wireless energy transmission system can realize a seamless coverage of energy supply field and also sensor activation, so that this thesis demonstrates the feasibility of battery-less sensor network.

Acknowledgments

First of all, I would like to express my sincere gratitude to my supervisor Assoc. Prof. Kei Sakaguchi for his continuous support and immense knowledge. Without his support, this thesis would not have been possible.

Besides my supervisor, I would like to express the deepest appreciation to the rest of my thesis committee members Prof. Makoto Ando, Prof. Junichi Takada, Prof. Jiro Hirokawa, Assoc. Prof. Atsuhiro Nishikata and Prof. Naoki Shinohara, for their insightful comments and encouragement.

From October 2013 to January 2014, I had a chance to be a visiting researcher at Georgia Institute of Technology. At that time, Prof. Gregory David Durgin was my supervisor, and supported my research. I wish to express my deep appreciation for his kindness and hospitality. Also, I would like to offer my special thanks to Dr. Christopher Valenta, Mr. Blake Marshall and the other laboratory members. In addition, from April 2013 to March 2014, I was studying at Osaka University. I would like to show my gratitude to Prof. Seiichi Sampei, Prof. Shinichi Miyamoto, and Assoc. Prof. Shinsuke Ibi for accepting me at the laboratory and giving insightful comments to my research.

There are also several people who have contributed their valuable time to my research work in this thesis. At first, I would like to show my greatest appreciation to Emeritus Prof. Kiyomichi Araki who always provides insightful comments and suggestions to my research. Also, I am deeply grateful to Assist. Prof. Gia Khanh Tran, who always gives me many useful advice, checks my manuscripts, and teaches me a lot of knowledge. In addition, I would like to offer my special thanks to Dr. Keiichi Mizutani, Dr. Namzilp Lertwiram, Mr. Gento Matsushita and the other members of Araki-Sakaguchi laboratory and Sampei laboratory for a lot of discussions of my research and helping me in the experiments of the thesis.

Finally, I am indebted to Mr. Minoru Furukawa from Nihon Dengyo Kosaku Co. Ltd., Mr. Hiroshi Iwai from Panasonic Cooperation and Mr. Masaaki Suzuki from TESSERA TECHNOLOGY INC. for helping the development of battery-less sensor node and the experiments.

Chapter 1

Introduction

1.1 Wireless sensor networks

In recent years, the number of sensors has been dramatically increased and closely related to our lives. Nowadays, portable devices, including smart phones and tablets, have several sensors [1] and it is easy to employ sensors owing to the evolution of CPU board, such as Arduino [2] or Raspberry Pi [3], even for personal use. Sensor Networks (SNs), which are sometimes called Internet of Things/Everything (IoT/IoE) or Machine to Machine (M2M) networks as well, are expected to realize many applications by using numerous sensors and related devices. [4] forecasts the demand of sensors will be growing up from billion in 2012 to trillion within the next decades. [5] also forecasts the number of connected devices to the Internet will be increased to 50 billions in 2020. Such networks are used for performing meter reading, Building/Home Energy Management Systems (BEMS/HEMS), health care, agricultural applications, localization, distribution systems and so on [6].

Meter reading
Gas, water and power meters can be remotely read to reduce the cost of reading and to immediately utilize the data [7]. In particular, the demand of power meter reading, which is called smart meter or smart grid [8], is dramatically increased because the data are expected to be used for reducing the energy consumption and CO_2.

BEMS/HEMS
InfraRed (IR), luminance, temperature and humidity sensors in buildings or homes are employed to monitor and record the environmental status and human behaviors. These data are

used to reduce consumed power of electrical appliances and to maintain comfort [9]- [11]. In particular, BEMS/HEMS for green applications are often treated as a part of smart grid.

Agricultural applications

The data of weather, i.e. temperature, humidity, rainfall, wind speed and air pressure, are automatically recorded to predict and improve quality and quantity of farm products [12]. In dairy farming, health conditions and behavior of livestock are monitored, recorded and managed by vital sensors.

Health care

ElectroCardioGram (ECG), heart rate and perspiration are monitored and recorded to manage physical condition or to detect abnormal state [13]. In recent years, for personal use, smart devices are equipped on their bodies such as wrists [14].

Localization

Global Positioning System (GPS) is also one of the SN applications. In recent years, GPS sensors are equipped in the mobile devices to find their locations and employ navigation systems. In indoor environments where GPS cannot exhibit the performance, the RF signal from WiFi can be used for the localization [15].

Distribution systems

In warehouse, supermarket and transportation, ID tags and shocked sensors are used to keep and manage their cargoes [16]. In most cases, the sensors are disposed of after they have been used.

Security/safety

Some kinds of gas sensors and flame sensors play roles of preventing or detecting disasters [17]. Cameras, embedding image sensors, human detection sensors and radar systems are employed to prevent, detect and record suspicious and criminal activities [18] [19].

The data of SNs can be gathered through wired link such as Local Area Network (LAN), Power Line Communication (PLC) while many SNs employ wireless technology for ease of installation. By employing wireless links, sensors are released from wires and numerous sensors can be arbitrarily distributed. For the standard of the data communication, several wireless protocols can be used. IEEE 802.15.4 [20] is standardized for low data rate, low power and low complexity, short-range communications in the framework of Wireless Personal Area Network (WPAN), typically Wireless

Sensor Networks (WSNs). The standard is basis for Zigbee. In addition, IEEE 802.15.4g [21] and 4e [22] are standardized for its PHYsical (PHY) layer and Mediam Access Control (MAC) layer respectively. IEEE 802.15.1 [23] called Bluetooth 1.1 is standardized for communications between mobile devices. Bluetooth Special Interest Group (SIG) extends the standard to Bluetooth 4.0LE for sensor networks called Bluetooth Low Energy (BLE).

One of the critical issues in WSNs is the requirements of powering a huge number of sensors. Table 1.1 shows advantages and disadvantages of each energy source. Power-plugged sensor nodes are suffered from the wiring cost and its complexity. Lifetime of battery-embedded sensor nodes is limited by the electric capacity. In general, wireless sensor node consists of sensors, MCUs and RFICs. Figure 1.1 shows lifetime of battery-embedded sensor and typical consumed current of sensors, Micro Controller Units (MCUs) and Radio Frequency Integrated Circuits (RFICs) [24]-[37]. According to demand, these devices can configure into sleep mode, by which the low-power consumption can be realized, so that the average power consumption is defined by the ratio between active and sleep period. However, the lifetime of 2000 and 200 mAh batteries, which are nominal electric capacity of AA size and coin batteries respectively, is limited by a few days, months or years. Therefore, the replacement cost increases in proportion to the number of sensors. In recent years, several researchers and companies have proposed that environmental energy can be employed to activate sensor nodes [38]. EnOcean alliance proposes to realize battery-less sensor networks using energy harvesting technology and standardizes their own wireless protocol for wireless applications with ultra-low power consumption [39]. However, such ambient power source can be easily affected by the surrounding environment, e.g. solar-powered sensor nodes cannot be activated or charged in the nighttime or motion-powered sensor nodes cannot be activated without external trigger such as human finger pushing. To deal with these powering problems, this thesis proposes to supply energy to sensor nodes by using microwave wireless energy transmission.

1.2 Wireless energy transmission

Wireless energy transmission methods are categorized into three types, i.e. inductive coupling, resonant coupling, microwave emission [40].

It is well known that inductive coupling method is used for IC card without any batteries to go through automatic ticket gate. In such High Frequency (HF) Radio Frequency IDentification (RFID) sytems, 13.56 MHz is mainly employed and [41] is one of the world standards. In addition, Qi for charging mobile devices without any cables is one of the applications of this method which

Table 1.1 Energy source for sensor node.

Source	Advantage	Disadvantage	
Electrical plug	Stable activation	Cable complexity / Wiring cost	
Electrical battery	Cable-less	Limited lifetime / Replacement cost	
Energy harvesting	Cable-less / Unlimited-lifetime	Unstable / Environment-dependent	

is standardized by Wireless Power Consortium (WPC). In Qi, maximum transmit power is limited by 5 W and the frequency band of 100 kHz to 200 kHz is employed. The principle of this method is explained as follow. When the electrical current flows through a transmitter (Tx) coil, magnetic field is generated as shown in Fig. 1.2 (a). Then, the electrical current also flows through a receiver (Rx) coil by the magnetic field. Since the received power is in proportion to the magnetic flux through the Rx coil, the powering range is limited by a few centi-meters.

In resonant coupling method, a Tx coil and a Rx coil can be employed as resonator. When the electrical current flows through the Tx coil, magnetic field is generated as shown in Fig. 1.2 (b). Then, if a Rx coil has a same resonant circuit of the Tx coil, the electrical current also flows through a Rx coil by the magnetic field. Different from the inductive coupling method, this method can supply power in a few meters. [42] firstly investigated this method and achieved to transmit 60 W with about 40% efficiency in 2 meters. However, because the powering range depends on the wavelength, the size of Rx coil would not be small to implement in sensor nodes, while this method is expected to be employed for charging electric vehicles [43].

In the microwave emission method as shown in Fig. 1.2 (c), energy emitted from Tx is collected at the Rx using rectenna (rectifying antenna) to receive and convert microwave into direct current. Compared with the other schemes, long range transmission can be realized by increasing transmit power or antenna gain. Space Solar Power Satellite (SSPS) [44] and Ultra High Frequency (UHF) RFID employ this scheme. In WSNs, numerous ubiquitous sensors are distributed in indoor environments. In order to supply energy to all of them, the radio wave emission is employed in this thesis and the details are discussed in the next chapter.

(a) Lifetime of battery-powered sensor node

(b) Trend of consumed current
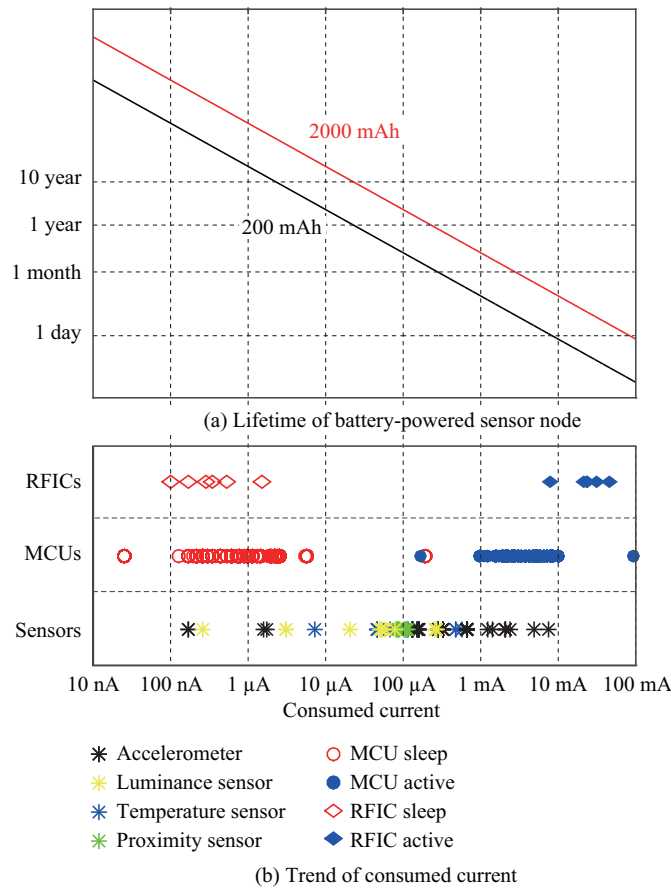
Figure 1.1   Lifetime of battery-powered sensor node
and trend of consumed current of sensors, MCUs, RFICs.

1.3   Wireless grid

Figure 1.3 shows the proposed wireless grid to realize battery-less sensor networks in indoor environments. Sensor nodes are activated by wireless energy transmission using microwave, so that sensor nodes can be deployed at their preferred placements. In order to supply energy to these arbitrarily distributed sensor nodes, wireless grid employs multiple energy transmitters to combat path-loss attenuation. In addition, carrier shift diversity is introduced to the multiple transmitters to avoid the interference among the multiple sources. In the battery-less sensor nodes, an intermittent operation is employed to reduce their consumed power and capacitor is equipped to manage the energy of the intermittent operation. By introducing the wireless grid, WSNs can be released from batteries and expected to be easily installed in indoor environments.

(a) Inductive coupling
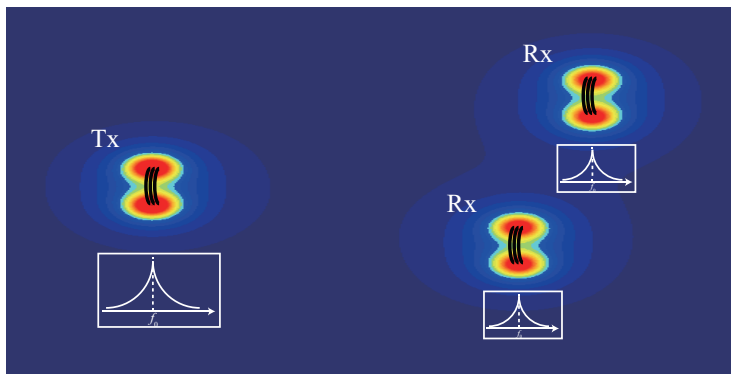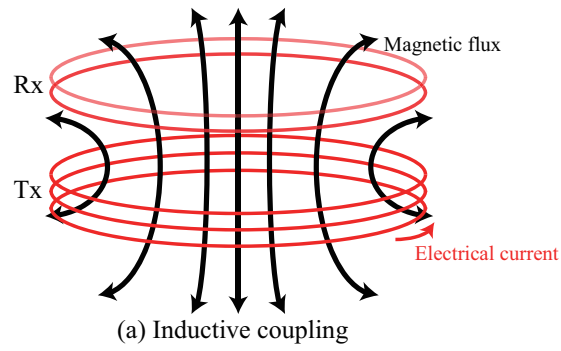
(b) Resonant coupling

(c) Microwave emission
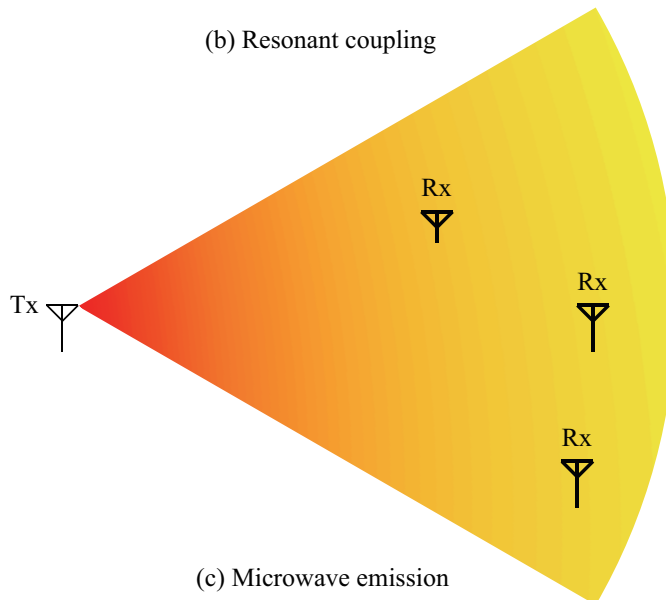
Figure 1.2   Wireless energy transmission schemes.
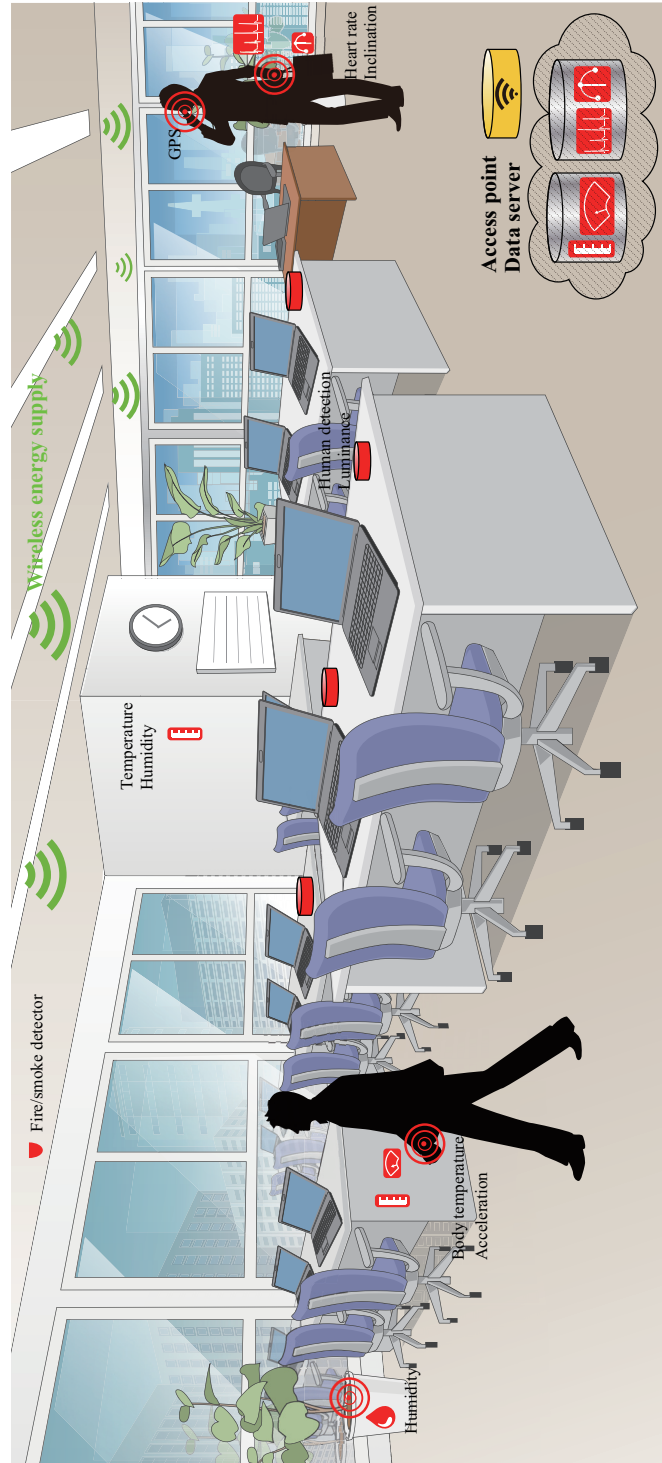
Figure 1.3 An example of wireless grid in an indoor environment.

1.4   Outline of this thesis

This thesis aims to realize battery-less sensor networks in indoor environments, and theoretically and experimentally validate the effectiveness the proposed wireless energy transmission system. Figure 1.4 shows the structure of the thesis and Tab. 1.2 shows experimental configurations of Chs. 3-5.

Chapter 2 introduces RFID systems as conventional systems of wireless energy transmission using microwave, compares the thesis with the other researches and illustrates the radio regulation of wireless energy transmission and wireless sensor networks.

Chapter 3 proposes multi-point wireless energy transmission with carrier shift diversity to realize seamless coverage of energy supply field, gives theoretical analysis on the received power and conducts indoor experiments to validate the effectiveness of the proposed system in terms of the RF propagation. In the experiments, an application of RFID systems is assumed and RFID R/Ws and an antenna of IC tag are employed to measure the RF received power. In addition, 2 transmitters and 1 receiver, which is located and moved between the 2 transmitters in horizontal and vertical plane, are set along the straight line to easily conduct the experiments because the antenna directivity is not needed to be considered and horizontal polarization is employed to easily observe multipath effect.

Chapter 4 provides the designed concept of battery-less sensor nodes, develops real battery-less sensor nodes equipped with human detection sensor by off-the-shelf devices, and conducts indoor experiments using the developed sensor node to validate the effectiveness of the proposed system in terms of the activation of the sensor node. In the experiments, an application of human detection is assumed and the antenna height of Txs and Rx is the same as the height of the desks. As with the experiments of Ch. 3, 2 transmitters and 1 receiver, which is moved between the 2 transmitters, are set along the straight line and vertical polarization is employed to mitigate the multipath effect and to achieve 100% coverage.

Chapter 5 provides design criteria of wireless energy transmission coverage in real indoor environments, implements wireless grid into a real indoor environment with the developments of wireless energy transmitters embedded in LED ceiling lights, battery-less sensor nodes and wireless sensor network, and conducts indoor experiments to verify the activation possibility of battery-less sensor nodes in a real indoor environment. In the experiments, an application of human detection in 2 dimensional space is assumed and 4 transmitters and 1 receiver are set to the ceiling and moved among these transmitters at the height of desks respectively.

Finally, Ch. 6 concludes the thesis.

The results of Ch. 3 are published in

- D. Maehara, G. K. Tran, K. Sakaguchi, K. Araki, M. Furukawa, "Experiment Validating the Effectiveness of Multi-point Wireless Energy Transmission with Carrier Shift Diversity," *IEICE Trans. on Commun.,* vol. E97-B, no. 09, pp.1928-1937, Apr. 2014.

- D. Maehara, G. K. Tran, K. Sakaguchi, K. Araki, T. Miyamoto, M.Furukawa, "Experimental Study on Multi-point Wireless Energy Transmission at 950MHz Band," in Proc. *IEEE ISSSE2012,* Oct. 2012.

The results of Ch. 4 are published in

- D. Maehara, G. K. Tran, K. Sakaguchi, K. Araki, "Experimental Study on Battery-less Sensor Network Activated by Multi-point Wireless Energy Transmission," *IEICE Trans. on Commun.,* vol.E99-B, no.04, 2016.

- D. Maehara, R. Akai, G. K. Tran, K. Sakaguchi, S. Sampei, K. Araki, H. Iwai, "Experiment on Battery-less Sensor Activation via Multi-point Wireless Energy Transmission," in Proc. *IEEE PIMRC2013,* Sep. 2013.

The results of Ch. 5 are published in

- D. Maehara, G. Matsushita, Y. Kuki, K. Sakaguchi, S. Sampei, K. Araki, "[Requested Talk] Development of Battery-less Sensor Networks for LED Light Control System," in *IEICE Technical Report, (SmartCom2014,)* SR2014-78, vol. 114, no. 284, pp. 109-116 Oct. 2014.

Chapter 2: Wireless Energy Transmission using Microwave

Chapter 3: Multi-point wireless energy transmission with carrier shift diversity
· Theory of multi-point wireless energy transmission
· Experiments on propagation characteristics to verify
  that the proposed scheme can mitigate
  path-loss attenuation, multi-path and interference between transmitters

Chapter 4: Activation of battery-less sensor nodes via wireless energy transmission
· Design and development of battery-less sensor node
· Experiments measuring both received power and activation status
  to verify the sensor activation by using real hardware
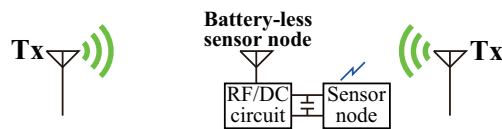
Chapter 5: Implementation of wireless grid in a real indoor environment
· Design of 2-D wireless energy transmission coverage
· Implement battery-less sensor network to a real indoor environment
· Experiments on coverage confirmation of sensor activation
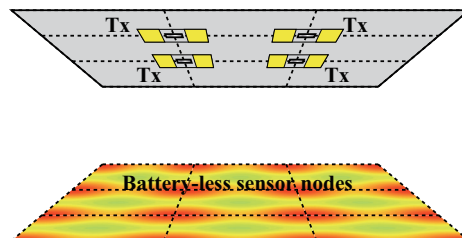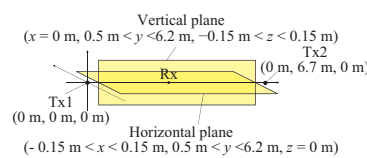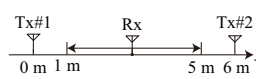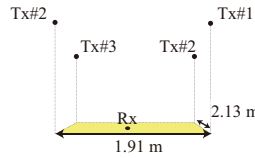
Figure 1.4   Structure of the thesis.

Table 1.2 Experimental configurations of Chs. 3-5.

Experiments in	Chapter 3	Chapter 4	Chapter 5
Measurement field	1 dimensional Horizontal 30 cm × 6.7 m Vertical 30 cm × 6.7 m 	1 dimensional 6 m 	2 dimensional 2.13 m × 1.91 m
Number of Txs	2	2	4
Polarization	Horizontal	Vertical	Circular
Rx power measurement	Yes	Yes	No
Activation measurement	No	Yes	Yes

Chapter 2

Wireless energy transmission using microwave

2.1 Introduction

The history of wireless energy transmission using microwave was started by Nikola Tesla. In 1904, he tried to transfer electrical energy wirelessly and conducted experiments. In the experiments, a transmit power of 300 kW over a radio wave of 150 kHz was transfered [45] [46]. However, the technology of microwave was employed for wireless communication system and radar application in World War II. Around 1960, based on Tesla's idea, W. C. Brown conducted experiments in which a transmit power of 400 W over a microwave of 2.45 GHz was transfered 5.5 m away from the transmitter. In addition, he firstly developed RF/DC conversion circuit and DC power of 100 W was received in the experiments [47]. After his works, around 1970, the technology of wireless energy transmission was focused on the 2 following applications. For low power application, Los Alamos National Laboratory developed passive RFID systems [48], while, for high power application, the idea of SSPS was proposed by P. E. Glaser [49] [50]. The original idea of RFID systems came from military demand to find the aircrafts by using radar technology. This chapter focuses on the UHF RFID systems as conventional wireless energy transmission system, briefly explains the principle, differentiates this thesis with other researches, and illustrates the radio regulations.

2.2 RFID systems

In the applications of distribution management, logistics and so on, ID tags are attached and the data of IDs are managed by the system. The RFID tags are categorized into 3 types, i.e. active tags, semi-passive tags, and passive tags [51]. Table 2.1 shows characteristics of these tags. Active tags, as shown in Fig. 2.1 (a), are activated by external battery. The data are transmitted by their transceivers. Therefore, active tags can transmit their data by their own initiative while passive or semi-passive tags cannot transmit the data without the signal of Reader/Writers (R/Ws). In addition, the communication range is larger than the other tag systems owing to the external batteries, which, however, results in limitation of their lifetime. Semi-passive tags, as shown in Fig. 2.1 (b), equip external batteries to activate their ICs. Different from active tags, there are no transceivers, while they employ backscatter signal to transmit the data. The backscatter signal can be created by the signal emitted from R/Ws. On the other hand, in passive tag systems as shown in Fig. 2.1 (c), R/Ws emits microwave signal to ID tags. ID tags are activated by converting the RF signal into DC power and transmit the data using backscatter signal to the R/Ws. The air interface is defined by [52]. Therefore, the cost and the consumed power of passive tags is lower than those of the other tags. For WSNs, semi-passive tags are usually employed because sensors and ICs can be easily activated and the consumed power can be lower than that of active tags. However, there is still a lifetime problem. In the proposed wireless grid, no additional batteries are employed as well as the passive tags. However the sensor node can transmit their sensing data by their own initiative like the active tags because capacitor embedded in the sensor node plays a role of rechargeable battery and can be charged by the energy of microwave. Therefore, the design of wireless energy supply and sensor node are similar to that of the passive tag and the active tag systems respectively.

One of the most critical issues of passive tags is coverage limitation. The coverage of energy supply field is restricted by the maximum transmit power limited by the radio regulation. By introducing Friis equation, in free space condition, the received power can be calculated as

$$P_{\mathrm{r}} = P_{\mathrm{t}} G_{\mathrm{t}} \left(\frac{\lambda}{4\pi l}\right)^2 G_{\mathrm{r}}, \tag{2.1}$$

where P_{t} is the transmit power, G_{t} is the Tx antenna gain, λ is the wavelength, l is the distance between Tx and Rx antenna, and G_{r} is the Rx antenna gain as shown in Fig. 2.2. Therefore, the maximum distance can be calculated as

$$l_{\mathrm{max}} = \frac{\lambda}{4\pi} \sqrt{\frac{P_{\mathrm{t}} G_{\mathrm{t}} G_{\mathrm{r}}}{P_{\mathrm{th}}}}, \tag{2.2}$$

where P_{th} is a threshold power to activate the ID tags. In general, the threshold power is calculated by the power consumption of IC and the RF/DC conversion efficiency.

Figure 2.3 shows the structure of RF/DC conversion circuit. RF signal received by antenna passes through Band Pass Filter (BPF), then is converted to DC signal by RF/DC conversion circuit and Low Pass Filter (LPF). The rectifying circuit employs a diode/diodes to rectify the RF signal. In general, Schottky diode is used for the circuit because it is is well known that this kind of diode consumes low power. Researchers design many kinds of rectifying circuit, i.e. single shunt type, Dickson charge pump, and so on [53]. A single shunt rectenna achieves 100% efficiency in ideal case [54]. However, in realistic case, the efficiency has non-linearity due to the diode parameters. In an ideal diode, the current flows only when positive voltage is applied. However, when the positive voltage is lower than the threshold voltage, the current does not flow. On the other hand, when the negative voltage is lower than a breakdown voltage, the current flows. By taking these two voltage values into account, the typical curve of the current characteristic is shown in Fig. 2.4. For rectifying microwave, Fig. 2.5 shows typical rectenna performance. RF/DC conversion efficiency in low power region is in proportion to input power due to the threshold voltage, while the efficiency in high power region is in inverse proportion to input power due to the breakdown voltage. In the RFID systems and the WSNs, the threshold voltage is generally induced. In addition to these parameters, impedance mismatch between antenna and rectifying circuit, harmonics generation and parasitic elements, e.g. series resistance, junction capacitor and junction resistance, also affect the efficiency. Thus, in the current passive RFID systems, the coverage is limited due to path-loss and the conversion efficiency of rectifying circuit.

Table 2.1   Active, semi-active and passive RFID tags.

	Active tag	semi-passive tag	passive tag
External battery	Yes	Yes	No
Data transmission	Transceiver	Backscatter	Backscatter
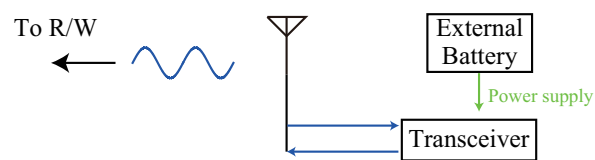
(a) Active tag
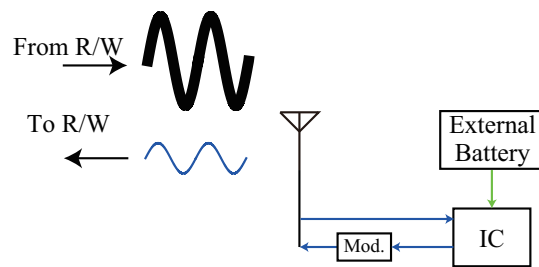
(b) Semi-passive tag
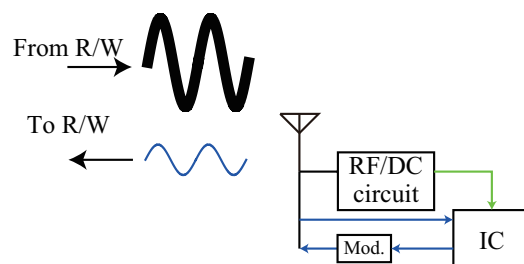
(c) Passive tag

Figure 2.1   ID tags for active, semi-passive and passive RFID systems.
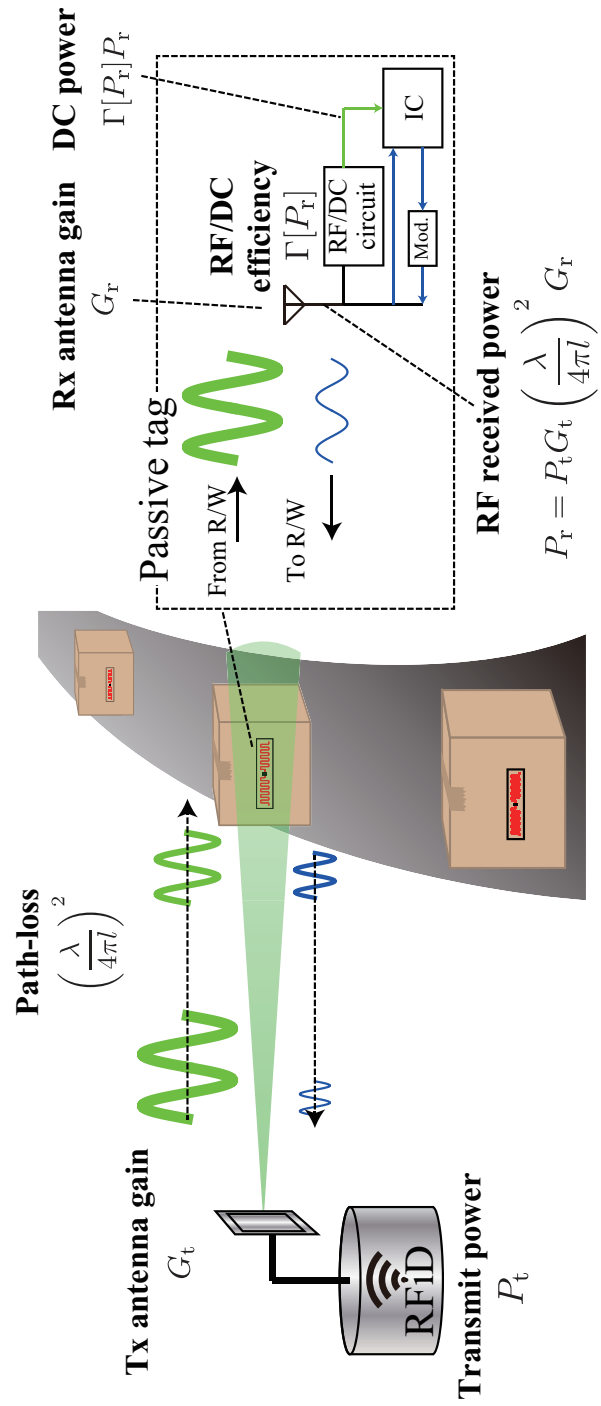
Figure 2.2   Passive RFID systems.
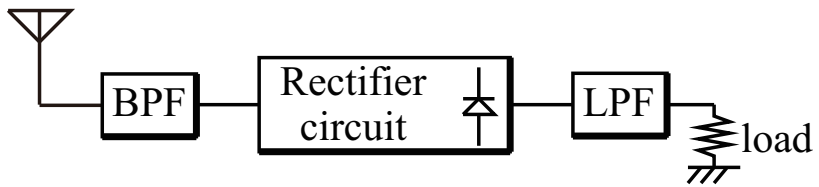
Figure 2.3   RF/DC conversion circuit.
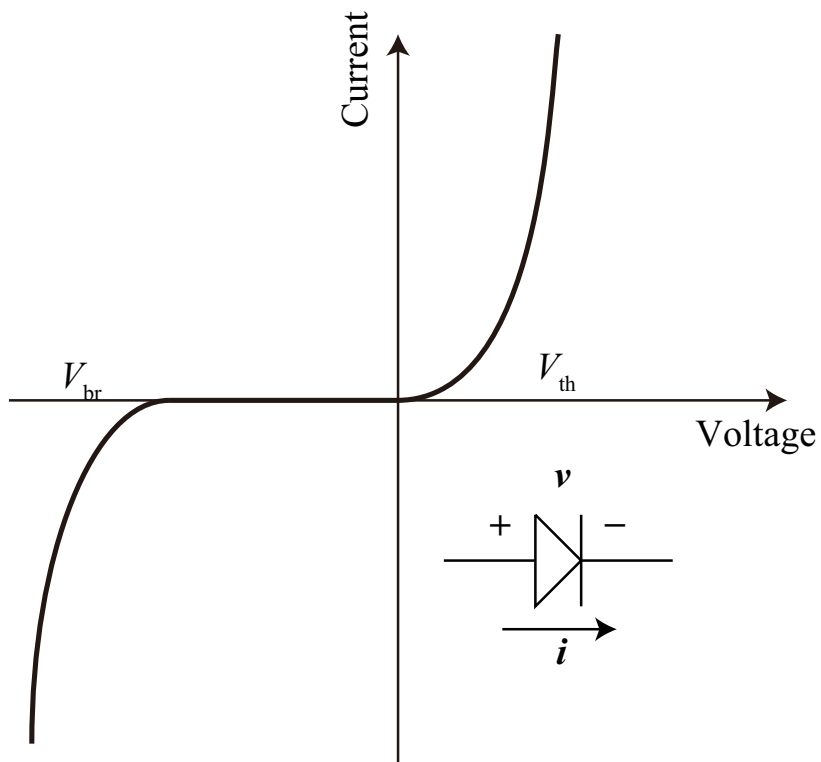
Figure 2.4   Diode I-V curve.
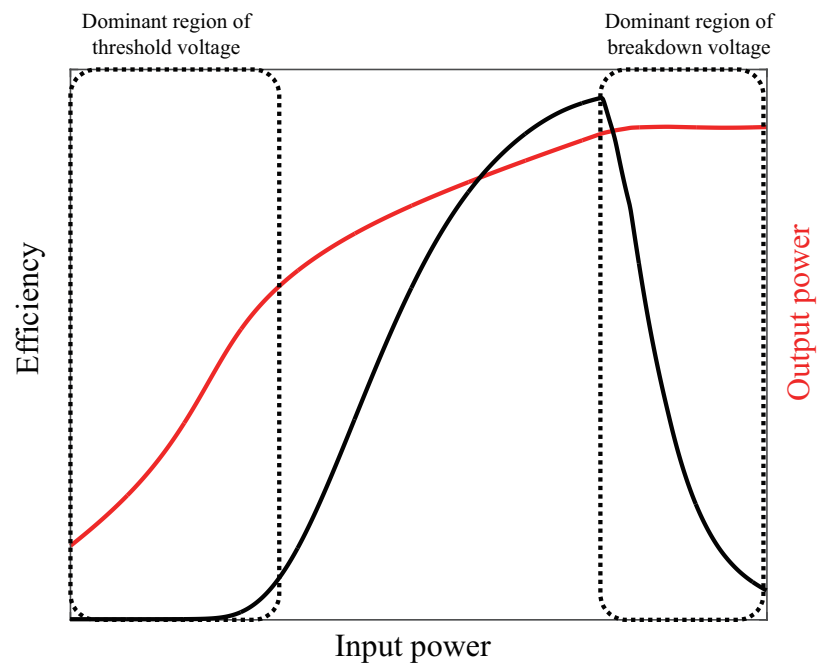
Figure 2.5 Non-linearity of rectifying performance.

2.3 Related works

Several researchers have attempted increasing wireless energy transmission coverage and introducing wireless energy transmission systems into WSNs. [55] proposed to transmit a special waveform to improve the RF/DC conversion efficiency by utilizing diode characteristics in low power region. [56] [57] proposed a scheduling scheme of wireless energy transmission and developed battery-less sensor system using IEEE802.11 based Wireless LAN (WLAN) system to avoid the interference between wireless power transmission system and data communication system. However, the single transmitter system is difficult to dramatically improve the coverage due to path-loss. [58] proposed to activate battery-less sensor nodes via ambient RF energy from TV tower. In other words, the system does not employ wireless energy transmitter. However, only several tens of μW can be harvested and the power depends on the environment.

To extend the coverage, multiple transmitters can be introduced to the systems. However, interference could occur between multiple transmitters. To avoid the interference, carrier sensing, such as Listen Before Talk (LBT), can be employed. However, this results in decreasing the time efficiency in terms of energy charging in proportion to the number of introduced transmitters. On the other hand, [59] employed multi-antenna systems, which simultaneously supply power, to improve the received power by phase control on each antenna. Therefore, the system can mitigate path-loss attenuation by increasing the number of antennas. However, the system can activate certain sensors with fixed location, so that a large number of sensor nodes cannot be simultaneously activated. [60] employed two orthogonal polarization and narrowband frequency modulation to improve the uniformity of the power density in a metallic over-moded waveguide cavity. However, this research focuses on charging mobile devices and assumes to supply energy in a small box like microwave oven.

From industrial companies, [61] produces RF/DC conversion circuits to work with 50 Ω antenna for various input power. [62] produces heat-, dust- and water-proof battery-less sensor node, whose rectenna maximally achieves more than 60% RF/DC conversion efficiency, to employ WSNs in harsh environments. [63] collaborated with [64] develops wireless energy transmission system charing portable deceives.

Different from the related works, the proposed wireless grid aims to realize seamless coverage of energy supply field to activate all sensor nodes distributed in indoor environments by the multipoint wireless energy transmission with carrier shift diversity. In the proposed scheme, multiple transmitters simultaneously and seamlessly supply energy to sensor nodes and the interference can

be avoided by the carrier shift diversity, in which different carrier frequency is allocated to multiple transmitters by dividing the dedicated frequency band. It is noted that this thesis focuses on wireless power supply system and the design of RF/DC conversion is out of scope.

2.4   Radio regulation

In 2005, 950 MHz band was allocated for the RFID systems in Japan [65]- [68]. Since 2012, 920 MHz band [69]- [71] has been available for the RFID systems, because the 950 MHz band was reallocated to LTE mobile systems. In this thesis, the experiments in Ch. 3 and from Ch. 4 are performed under the regulation of 950 MHz band and 920 MHz band respectively.

Figure 2.6 and Figure 2.7 show the spectrum mask at 950 MHz and 920 MHz bands. According to Japan's radio regulation, both 950 MHz and 920 MHz bands are categorized into 6 systems.

a, b Passive tag systems

    The number of channels is 21 (4 for **a**) where the bandwidth of each channel is 200 kHz. The maximum transmit power and the maximum Equivalent Isotropic Radiated Power (EIRP) are limited by 1 W (30 dBm) and 4 W (36 dBm) respectively. In addition, at **a**, LBT is not required.

c, d Specified low power radio station of passive tag systems

    The numbers of channels for **c** and **d** are 27 and 21 respectively. The bandwidth of each channel is 200 kHz. The maximum transmit powers are limited by 250 mW (24 dBm) and 10 mW (10 dBm) respectively.

e, f Specified low power radio station

    The numbers of channels for **e** and **f** are 17 and 33 respectively. The maximum transmit powers are limited by 10 mW (10 dBm) and 1 mW (0 dBm) respectively.

A, B Passive tag systems

    The number of channels is 6 (4 for **a**) where the bandwidth of each channel is 200 kHz. The maximum transmit power and the maximum EIRP are limited by 1 W (30 dBm) and 4 W (36 dBm) respectively. In addition, at **A**, LBT is not required.

C Specified low power radio station of passive tag systems.

    The number of channels is 19 where the bandwidth of each channel is 200 kHz. The maximum transmit power is limited by 250 mW (24 dBm).

D Convenience radio station of active tag systems

The number of channels is 15 where the bandwidth of each channel is 200 kHz. The maximum transmit power is limited by 250 mW (24 dBm).

E, F Specified low power radio station of active tag systems

The numbers of channels for **E** and **F** are 38 and 51. At 16 channels of **F**, the channel bandwidth is limited to 100 kHz while the bandwidth of the other channels is 200 kHz. The maximum transmit powers are limited by 20 mW (13 dBm) and 1 mW (0 dBm) respectively.

In the proposed wireless grid, 4 channels at **a** and **A** are employed for wireless energy transmission to perform continuous energy supply, while the channels at **f** and **F** are used for data communication.

Figure 2.8 shows frequency bands of passive RFID systems in the world [72]. In North and South America, East Asia and Australia, the bands are around 915 MHz, while, in European Union (EU), Africa and West Asia, those are around 865 MHz. Some countries support both 865 and 915 MHz bands. It is noted that the reallocation of Japan's UHF RFID systems aimed to be closely matched to the band of North America. In addition, the maximum transmit power is typically limited by 4 W EIRP or 2 W Equivalent Radiated Power (ERP). For the interference among multiple systems, Frequency Hopping Spread Spectrum (FHSS) and LBT are employed in countries which have large and small bandwidth respectively.
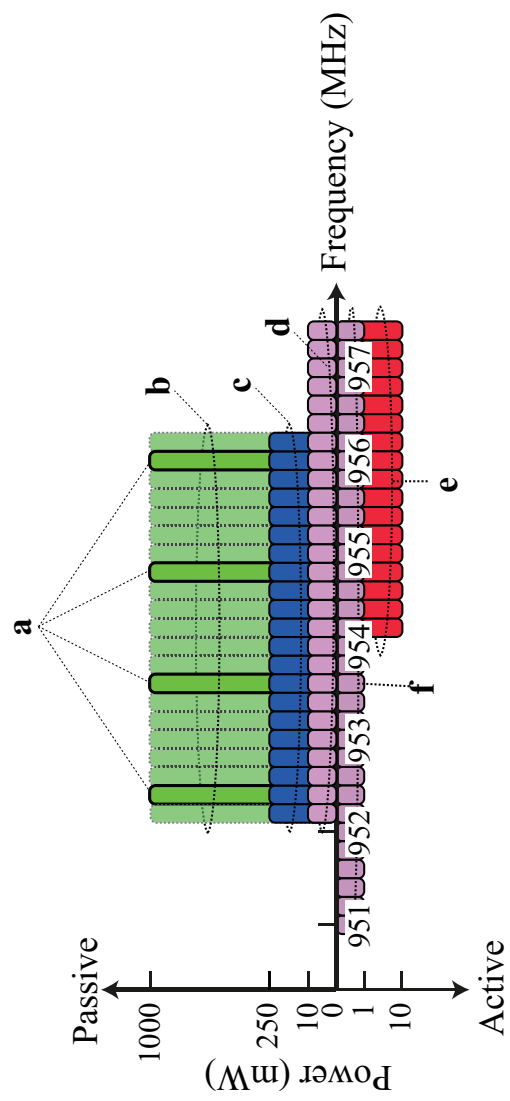
Figure 2.6 950 MHz band.
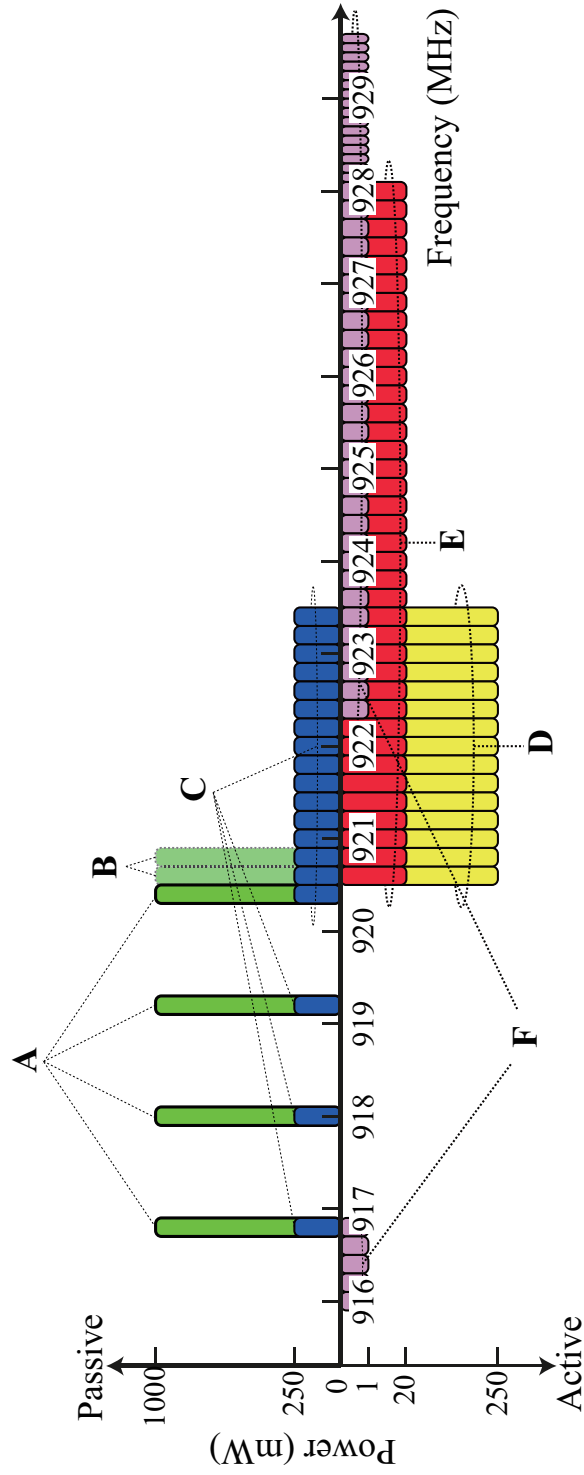
Figure 2.7 920 MHz band.
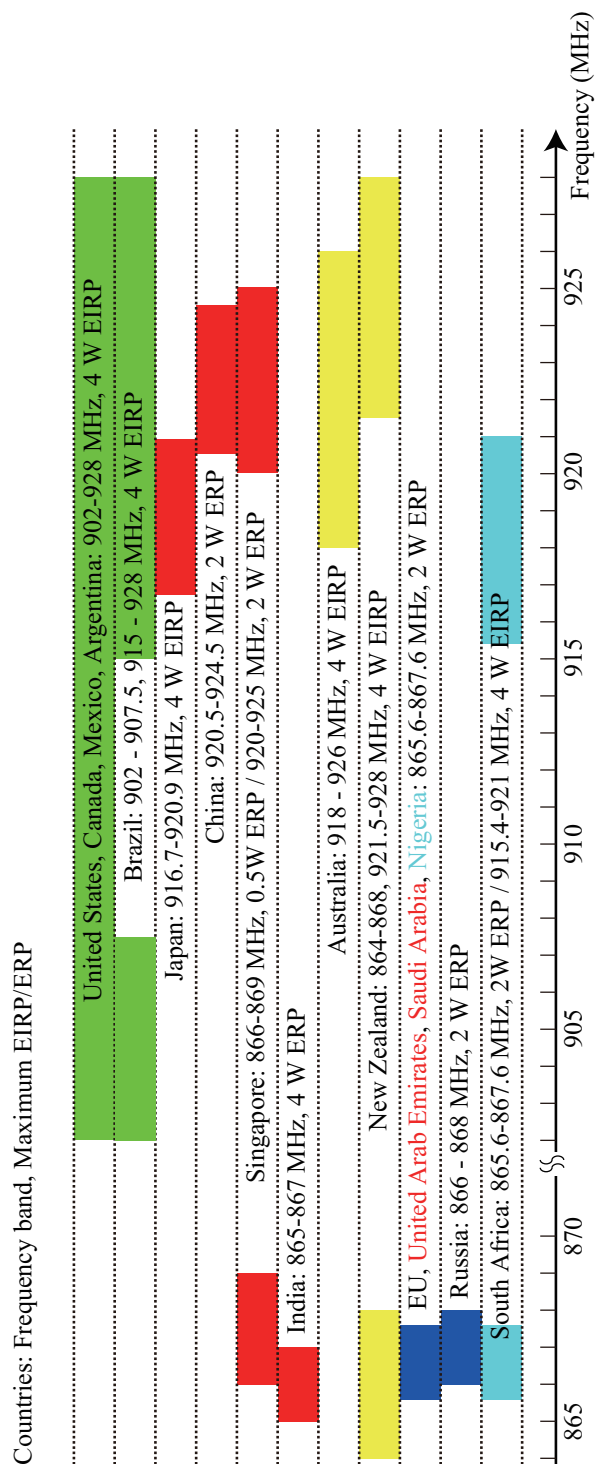
Figure 2.8   Frequency allocations for passive RFID systems in the world.

Chapter 3

Multi-point wireless energy transmission with carrier shift diversity

3.1 Introduction

As mentioned, the demand of WSNs is that numerous sensor nodes are employed. In order to seamlessly supply wireless energy to sensor nodes distributed arbitrarily in indoor environments, this chapter presents a novel multi-point wireless energy transmission scheme with carrier shift diversity, provides theoretical analysis and conducts indoor experiments in which we compare the power distribution and the coverage performance of different energy transmission schemes including conventional single-point, simple multi-point and our proposed multi-point scheme. To easily observe the effect of standing-wave caused by multipath and interference between multiple wave sources, the measurements are performed in both horizontal and vertical planes. The results together with those of numerical simulations that assumes a similar antenna setting show that the coverage of single-point and multi-point wireless energy transmission without carrier shift diversity are limited by path-loss, standing-wave created by multipath and interference between multiple wave sources. On the other hand, the proposed scheme can overcome power attenuation due to the path-loss as well as the effect of standing-wave created by multipath and interference between multiple wave sources. From this chapter, the conventional single-point, simple multi-point and our proposed multi-point are abbreviated as SP, MP and MPCSD respectively henceforth.

3.2   Concept of multi-point wireless energy transmission with carrier shift diversity

Figure 3.1-3.3 show the concepts of power distribution when employing SP, MP, MPCSD respectively. In Fig. 3.1, the coverage of SP is limited by the maximum transmit power defined by the radio regulation. In real indoor environments, the effect of standing-wave created by multipath becomes more remarkable in the case when the power difference between the direct and reflected waves is small. This effect will also occur due to reflections from floor and ceiling when horizontal polarized waves are concerned in RFID systems [51]. Due to this effect, it is difficult to provide seamless energy transmission to sensor nodes since the sensor nodes might be located at the deadspots.

To solve the coverage limitation due to path-loss in SP, multiple transmitters can be employed as shown in Figs. 3.2 and 3.3 to enhance the area of energy supply field. However, merely increasing the number of energy transmission points does not solve the limitation of the coverage as shown in Fig. 3.2. The effect of interference between multiple wave sources can be avoided by applying a Time Division Multiple Access (TDMA) scheme to MP. However, the time efficiency of energy supply decreases and the complexity of the system increases in proportion to the numbers of transmitters. To deal with the problem, we propose to apply carrier shift diversity to MP.

By using the carrier shift diversity, the destructive interference can be significantly alleviated as shown in Fig. 3.3 while energy can be simultaneously supplied by multiple transmitters. In other words, the proposed method can realize a seamless coverage extension without reducing the time efficiency of energy supply compared to that in MP.
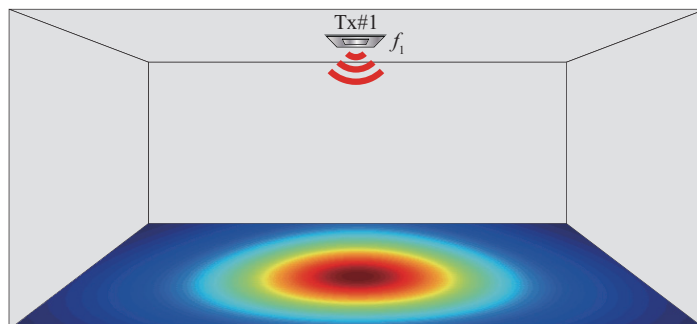
Figure 3.1   Power distribution of single-point wireless energy transmission.
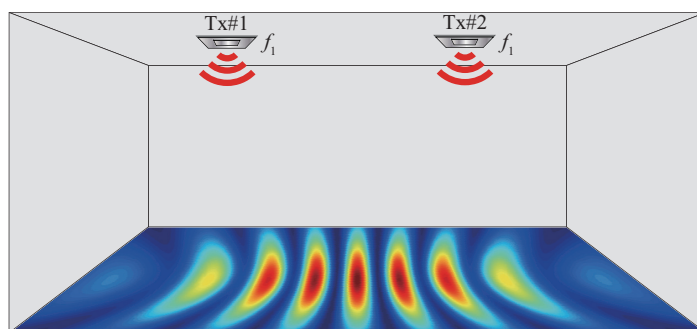
Figure 3.2   Power distribution of multi-point wireless energy transmission without carrier shift diversity.

Figure 3.3   Power distribution of multi-point wireless energy transmission with carrier shift diversity.

3.2.1 Spectrum allocation for carrier shift diversity

In the carrier shift diversity, when there are N Txs supplying energy to sensor nodes, 200 kHz of the available frequency band is divided into N orthogonal subcarriers as shown in Fig. 3.4, which is one of the channels of **a** and **A** in Figs. 2.6 and 2.7, at an interval of Δf by which the cycle of artificial fading can be configured as

$$T_{\mathrm{f}} = \frac{\mathrm{lcm}\left(\frac{1}{1}, \frac{1}{2}, \ldots, \frac{1}{N}\right)}{\Delta f} = 1/\Delta f, \tag{3.1}$$

where lcm( ) is the function of least common multiple. It is noted that the minimum cycle of peak-to-peak power becomes a reciprocal of bandwidth employing CSD. In addition, sensor node has a capacitor which plays a role of averaging its received power fluctuated by the artificial fading. It is noted that the frequency bandwidth in the case of CSD is as same as that in the cases of SP and MP because CSD merely divides the original dedicated channel into the subcarriers.
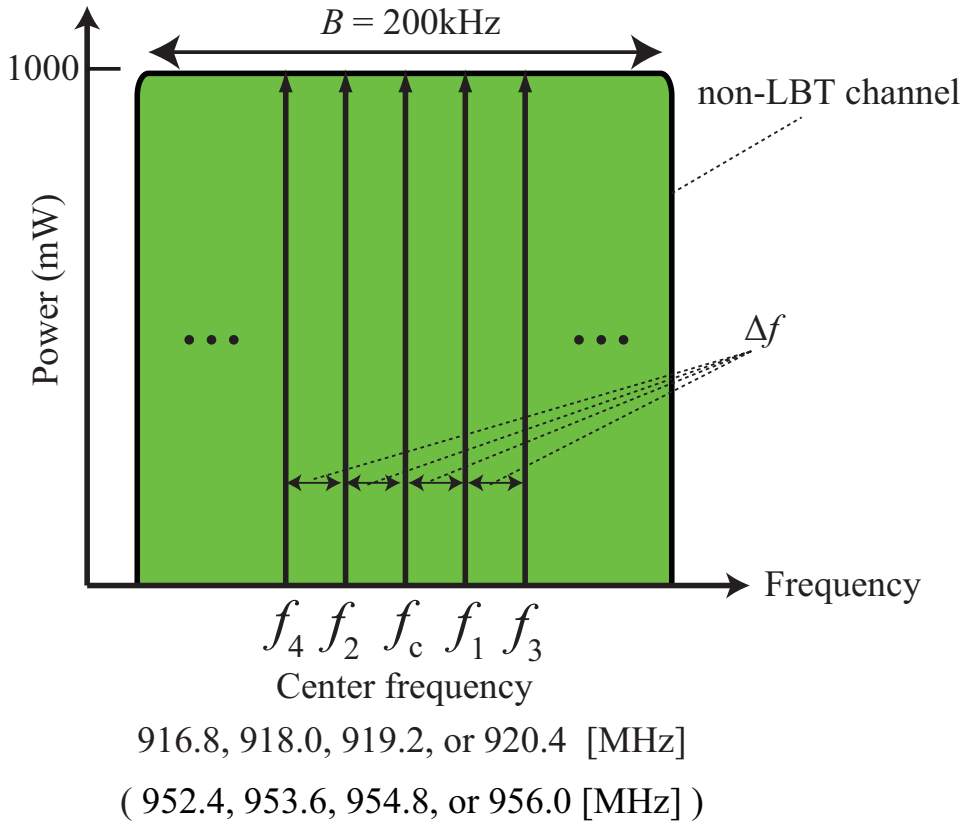
Figure 3.4 Frequency allocation for carrier shift diversity.

3.3 Multi-point wireless energy transmission

To confirm the concept of MPCSD, this section provides theoretical discussions. Assuming a system model for SP as shown in Fig. 3.5, the received signal at the sensor node from the i-th path ($i = 1, 2, \ldots, I$) is represented as

$$s_{1,i}(t) = \sqrt{P_{1,i}(l_1)} e^{j(\omega_1 t + \theta_{1,i}(l_1))}, \tag{3.2}$$

where l_1 is the location of the sensor node from the view point of Tx♯1, $P_{1,i}(l_1)$ is the power obtained from the i-th path, $\omega_1 = 2\pi f_1$ denotes the angular frequency with carrier frequency of f_1, and $\theta_{1,i}(l_1)$ is an initial phase. The received signal obtained from all of paths becomes

$$S_1(t) = \sum_{i=1}^{I} s_{1,i}(t). \tag{3.3}$$

According to [54], single-shunt rectenna converts RF signal into DC power with 100% efficiency by using a perfect matching network and an ideal diode with lossless property. Therefore, the received power can be described as

$$\begin{aligned} P_1 &= |S_1|^2 \\ &= \sum_{i=1}^{I} P_{1,i}(l_1) + \sum_{i=1}^{I} \sum_{j \neq i}^{I} \sqrt{P_{1,i}(l_1) P_{1,j}(l_1)} \cos\left[\theta_{1,i}(l_1) - \theta_{1,j}(l_1)\right]. \end{aligned} \tag{3.4}$$

This equation implies that the received power in SP is affected by the effect of standing-wave created by multipath as shown in the second term of Eq. (3.4). It is noted that when $i = 1$, the equation shows free space condition and the received power can be calculated by Eq. (2.1). In general, $P_{1,i}(l_1)$ ($i \neq 1$) is a function of the length of each path and its related reflection coefficients. According to Fresnel equations, reflection coefficient depends on polarization and incidence angle to the surface of obstacles. Therefore, the multipath components $P_{1,i}(l_1)$ with short path lengths or high reflection coefficient, are dominant in the received power P_1. In real RFID systems using horizontal polarization, reflected waves from the floor are dominant [51].

Assuming a system model for MP and MPCSD as in Figs. 3.6 and 3.7 respectively, the received signal at the sensor node obtained from the n-th Tx ($n = 1, 2, \ldots, N$) is represented as

$$S_n = \sum_{i=1}^{I} s_{n,i}. \tag{3.5}$$

To simplify this equation, we can convert Eq. (3.5) to the following equation

$$S_n = \sqrt{P_n(l_n)} e^{j(\omega_n t + \theta_n(l_n))}, \tag{3.6}$$

where l_n is the location of the Rx from the view point of n-th Tx, $P_n(l_n)$ is the average received power obtained from the n-th Tx including the multipath effect, $\omega_n = 2\pi f_n$ denotes the angular frequency with carrier frequency of f_n, and $\theta_n(l_n)$ is an initial phase as a result of standing-wave created by multipath. The received signal obtained from all the transmitters becomes

$$S = \sum_{n=1}^{N} S_n. \tag{3.7}$$

In the case when employing multiple transmitters, the total received power becomes

$$
\begin{aligned}
P(t) &= |S|^2 \\
&= \sum_{n=1}^{N} P_n(l_n) + \sum_{n=1}^{N}\sum_{m\neq n}^{N} \sqrt{P_n(l_n)P_m(l_m)} \times \cos\left[(\omega_n - \omega_m)t + \theta_n(l_n) - \theta_m(l_m)\right]
\end{aligned}
$$
$$\tag{3.8}$$

Here, the received power is averaged over a period of T_f, which is the cycle of the artificial fading of CSD. In the case of MP ($\omega_n = \omega_m$), the received power becomes

$$P^{\mathrm{MP}} = \sum_{n=1}^{N} P_n(l_n) + \sum_{n=1}^{N}\sum_{m\neq n}^{N} \sqrt{P_n(l_n)P_m(l_m)} \cos\left[\theta_n(l_n) - \theta_m(l_m)\right]. \tag{3.9}$$

In the case of MPCSD ($\omega_n \neq \omega_m$), on the other hand, the received power becomes

$$
\begin{aligned}
P^{\mathrm{MPCSD}} &= \sum_{n=1}^{N} P_n(l_n) + \sum_{n=1}^{N}\sum_{m\neq n}^{N} \sqrt{P_n(l_n)P_m(l_m)} \times \overline{\cos\left[(\omega_n - \omega_m)t + \theta_n(l_n) - \theta_m(l_m)\right]} \\
&= \sum_{n=1}^{N} P_n(l_n), \tag{3.10}
\end{aligned}
$$

where $\overline{[\ ]}$ is a function of time averaging. In this equation, the artificial fading created by carrier shift diversity cancels out the second term of Eq. (3.9) (the effect of interference between multiple wave sources) by time averaging. Therefore, the average received power turns into the summation of the power from all transmitters. Although the received power obtained from the n-th transmitter P_n is independently affected by standing-wave caused by multipath, the probability that all of the received powers become deadspots is significantly small in comparison to the case of SP.
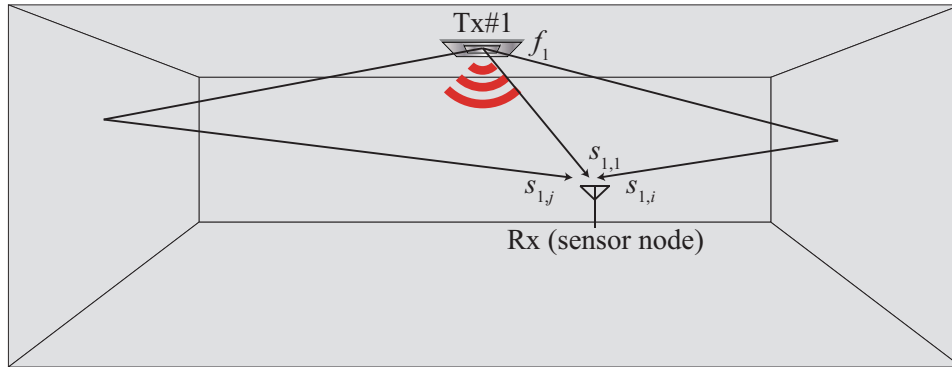
Figure 3.5   System model of single-point wireless energy transmission.

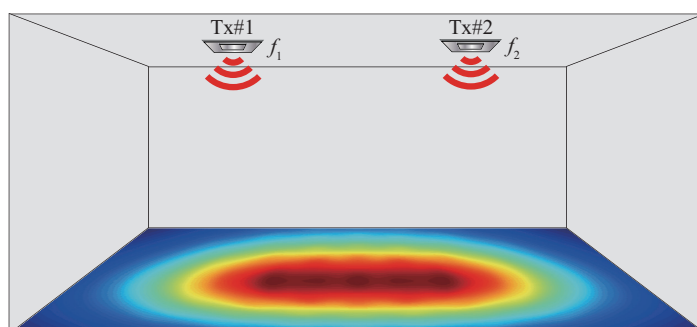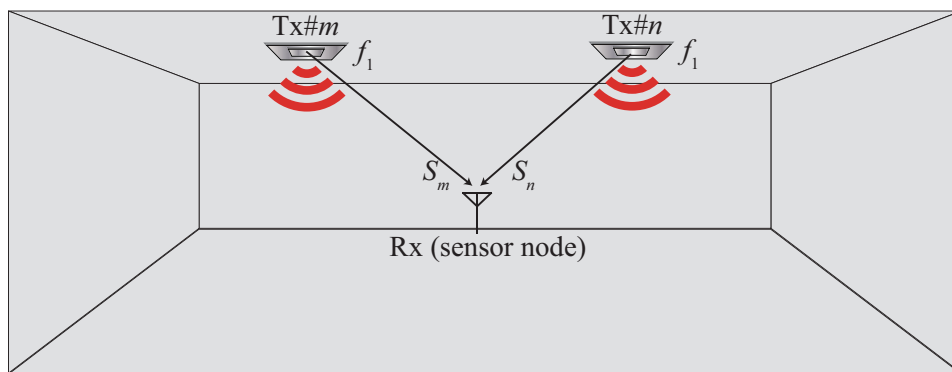**Figure 3.6**   System model of multi-point wireless energy transmission without carrier shift diversity.
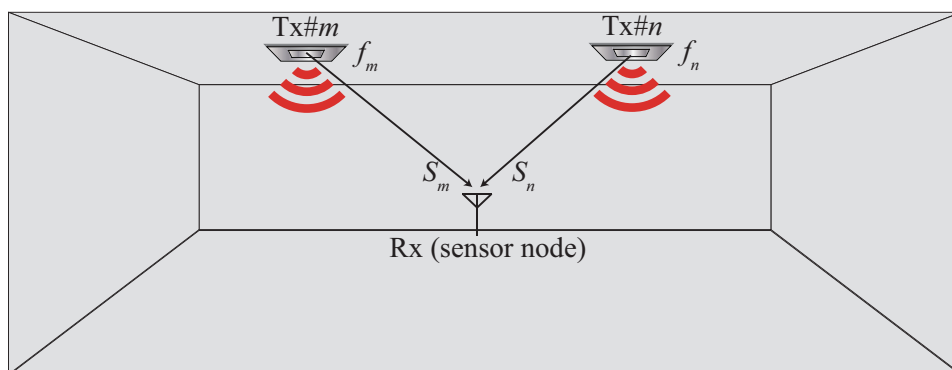
Figure 3.7   System model of multi-point wireless energy transmission with carrier shift diversity.

3.4 Experimental verification

In this section, in order to evaluate the concept of MPCSD in real environments, we conduct experiments in an indoor environment as shown in Fig. 3.8 assuming an application of RFID systems where 2 transmitters and 1 receiver, which is located and moved between the 2 transmitters, are set along the straight line to easily conduct the experiments because the antenna directivity is not needed to be considered. As mentioned, the effect of standing-wave created by multipath has an influence to the received power, so that the measurement is performed in both horizontal and vertical plane and horizontal polarization is employed in order to observe this effect. In addition, for comparison with the ideal case, we conduct numerical simulations.

3.4.1 Experiment method

The experimental system, environment and equipments are shown in Figs. 3.8, 3.9 and 3.10 respectively. A RFID R/W (Fig. 3.10 (a)) equipped with horizontal patch antennas (Fig. 3.10 (b)) of 6 dBi gain is employed to perform wireless energy transmission, while an IC tag antenna (Fig. 3.10 (c)) is used to receive energy. In addition, a variable phase shifter (Fig. 3.10 (d)) is used to produce carrier offset. The center frequency is 952.4 MHz and the transmit power per each antenna is 30 dBm. Both the Tx antenna $\sharp 1$ and $\sharp 2$ are set at the same height of 1.05 m from the floor. The measurement is performed in both horizontal and vertical planes. The coordinates of Tx$\sharp 1$ and Tx$\sharp 2$ are fixed as (0 m, 0 m, 0 m) and (0 m, 6.7 m, 0 m), while that of Rx is moved within the horizontal plane (-0.15 m $\leq x \leq 0.15$ m, 0.5 m $\leq y \leq 6.2$ m, $z = 0$ m) and the vertical plane ($x = 0$ m, 0.5 m $\leq y \leq$ 6.2 m, -0.15 m $\leq z \leq 0.15$ m) by a positioner with an interval of 3 cm to evaluate the coverage of wireless energy transmission as shown in Fig. 3.11. For SP, we consider both cases that wireless power are transmitted from either Tx antenna $\sharp 1$ or $\sharp 2$. For MP, signal from the RFID R/W is divided by a power divider, and then transmitted from both the Tx antenna $\sharp 1$ and $\sharp 2$. In the case of MPCSD, the carrier offset is produced by a variable phase shifter between the divider and the Tx antenna $\sharp 2$. The output phase can be changed by imposing different voltages controlled by a D/A board equipped on a PC. In this experiment, continuous constant phase change is created by setting the phase to repeatedly increase from 0 to 2π in a step of $2\pi/100$ as shown in Fig. 3.12 in which the phase difference between input and output of the phase shifter is measured by network analyzer. By this method, a carrier offset of 50 Hz apart from the center frequency 952.4 MHz can be generated. It is noted that because the arbitrary carrier offset cannot be performed by the R/W, the experiments substitute the phase shifter for frequency offset.
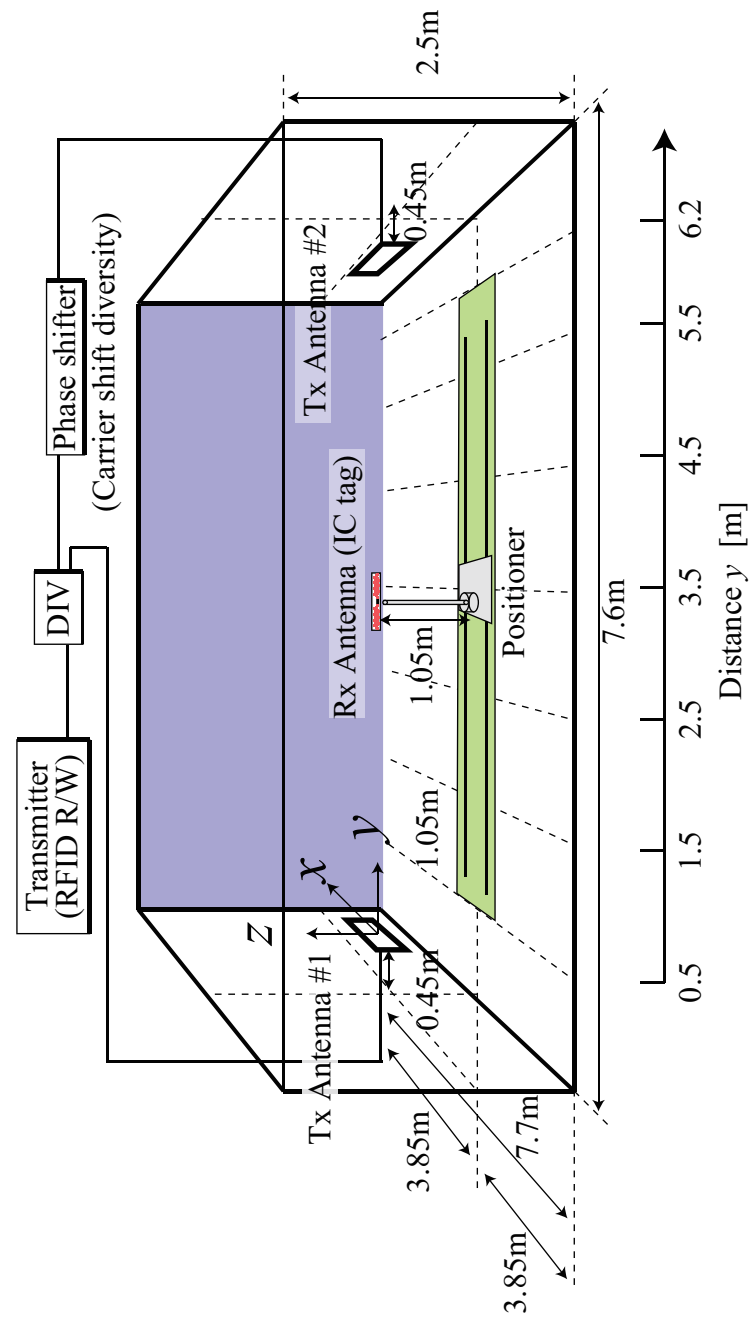
Figure 3.8 Experimental system for energy transmission.
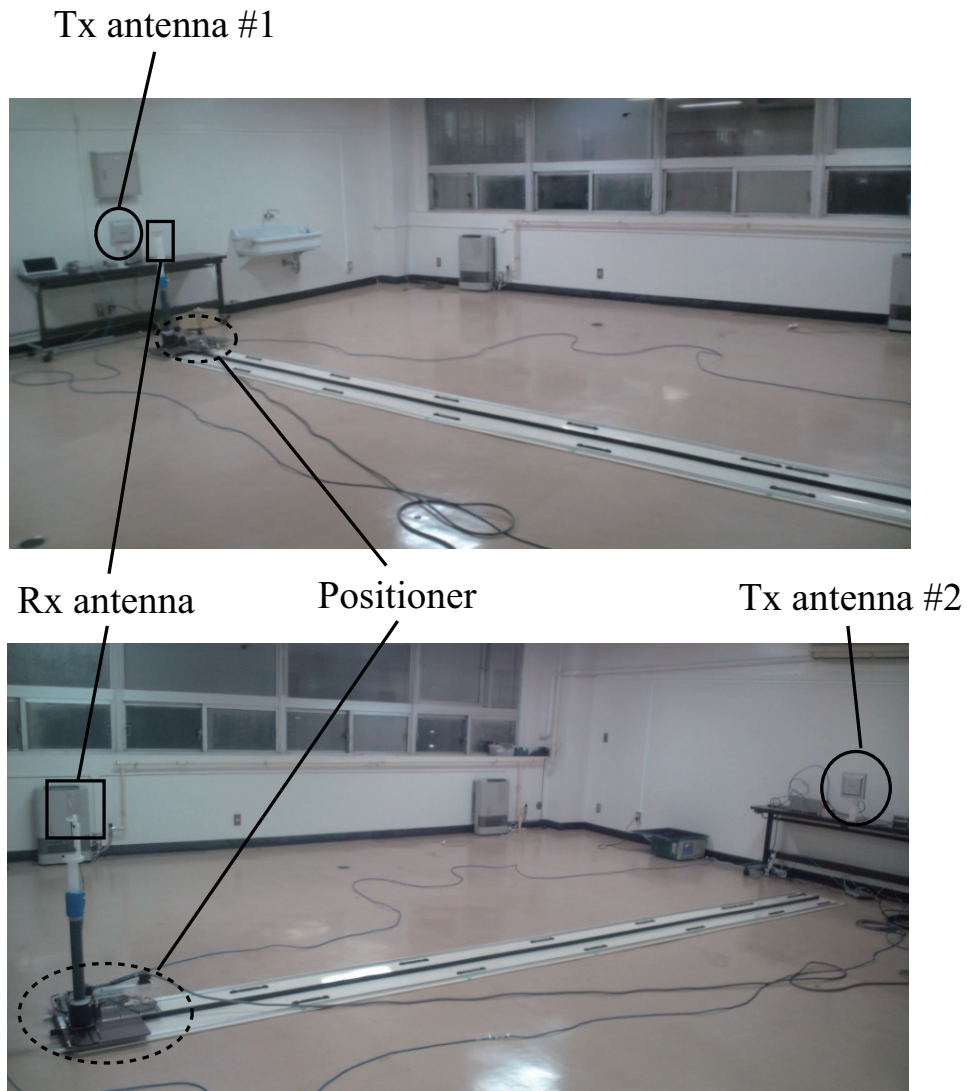
Figure 3.9   Experimental environment (Photo).

(a) RFID Reader/Writer

(b) Tx antenna

Antenna of IC tag ·······Balun

(c) Rx antenna

(d) Phase shifter
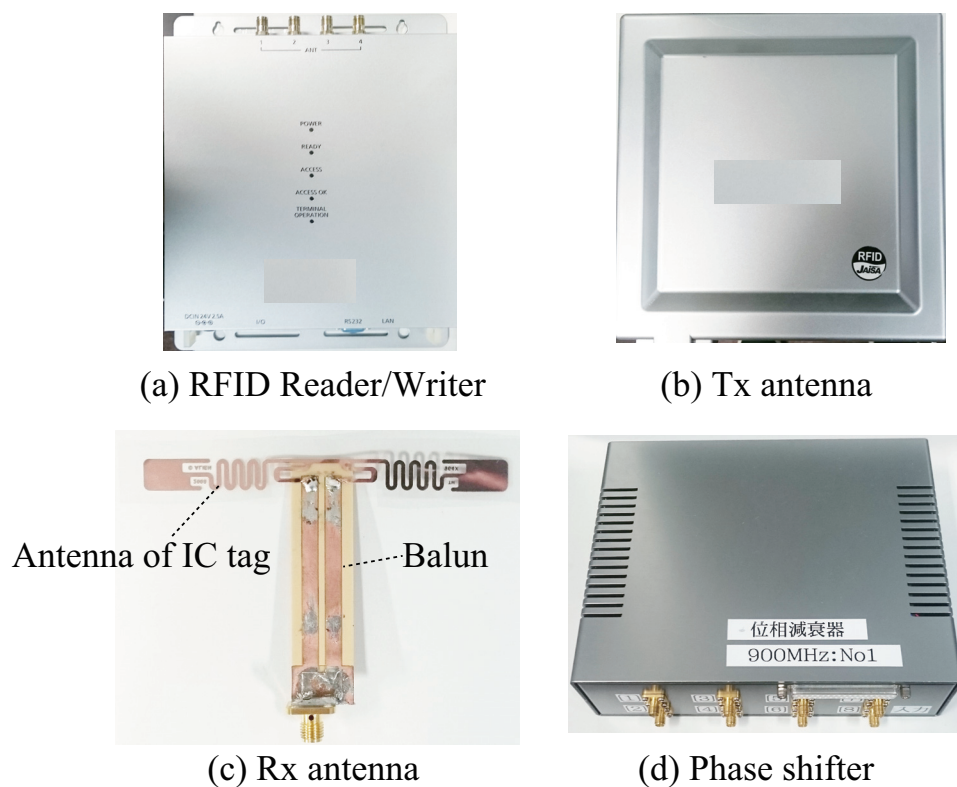
Figure 3.10　Experimental equipments.

Vertical plane
($x = 0$ m, 0.5 m $< y <6.2$ m, -0.15 m $< z < 0.15$ m)

z

x

Tx2
(0 m, 6.7 m, 0 m)

y

Tx1
(0 m, 0 m, 0 m)

Horizontal plane
($- 0.15$ m $< x < 0.15$ m, 0.5 m $< y <6.2$ m, $z = 0$ m)
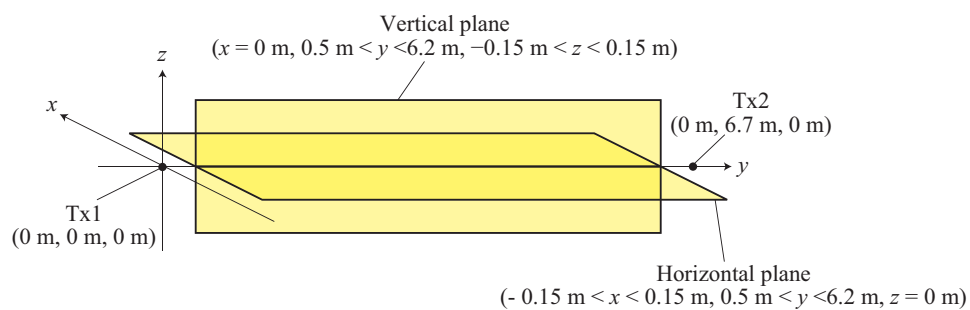
Figure 3.11　Measurement field.

Table 3.1   Experimental parameters.

Parameter	Value
Transmit power per each antenna	30 dBm
Center frequency	952.4 MHz
Carrier shift	50 Hz
Measurement point interval	3 cm≈ $\lambda/10$
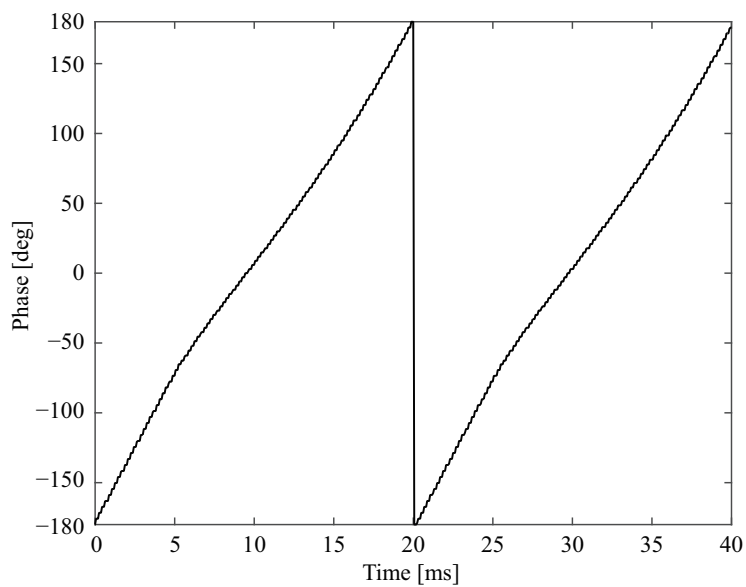
Figure 3.12   Relationship between phase and time in phase shifter.

3.4.2 Numerical simulation

In order to easily understand the power distribution property and coverage performance of the three schemes, we conduct a ray tracing simulation where the placement of Txs and Rx are the same as those of the experiments. Figure 3.13 shows the simulation model where 3 paths (direct path (1) and reflected paths from the floor (2) and wall (3)) are taken into account since it can be expected that these obstacles dominantly affect the power distribution.

Since each path length from Tx♯1 can be calculated as

$$l_{11}(y) = y, \quad l_{12}(y) = \sqrt{(2H)^2 + y^2}, \quad l_{13}(y) = 2L - y, \tag{3.11}$$

the received power obtained from each path in the case of Tx♯1 and Tx♯2 can be, respectively, expressed as

$$P_{11}(y) = P_t G_t(0) \frac{\lambda}{4\pi l_{11}} e^{-j2\pi \frac{l_{11}}{\lambda}} G_r(0) \tag{3.12}$$

$$P_{12}(y) = P_t G_t(\Theta_{12}) \frac{\lambda}{4\pi l_{12}} e^{-j2\pi \frac{l_{12}}{\lambda}} G_r(\Theta_{12}) \kappa(\frac{\pi}{2} - \Theta_{12}) \tag{3.13}$$

$$P_{13}(y) = P_t G_t(0) \frac{\lambda}{4\pi l_3} e^{-j2\pi \frac{l_{13}}{\lambda}} G_r(0) \kappa(0) \tag{3.14}$$

$$\cos \Theta_{12} = \frac{y}{2H} \tag{3.15}$$

$$P_{21}(y) = P_{11}(Y - y), \quad P_{22}(y) = P_{12}(Y - y), \quad P_{23}(y) = P_{13}(Y - y), \tag{3.16}$$

where P_t is the transmit power, G_t and G_r are, respectively, Tx and Rx antenna gains, and κ is the reflection coefficient calculated by Fresnel's law under the relative permittivity of 4.5. It is noted that the Rx antenna gain from Tx♯1 and ♯2 might be slightly different because the board of balun is implemented on the back of IC tag to measure the received power by 50 Ω port of the spectrum analyzer. However, in the simulation, the difference is ignored and it is assumed that the Rx antenna gain from Tx♯1 and ♯2 are the same. From Eqs. (3.2) and (3.3), the received signal from Tx♯1 and ♯2 can be, respectively, expressed as

$$S_1(y) = \sum_{i=1}^{I} \sqrt{P_{1,i}} e^{j(\omega_1 t + \frac{l_{1,i}}{\lambda})}, \quad S_2(y) = \sum_{i=1}^{I} \sqrt{P_{2,i}} e^{j(\omega_2 t + \frac{l_{2,i}}{\lambda})}, \tag{3.17}$$

where zero initial phase at each transmitter is assumed. From Eqs. (3.4)-(3.10), the received power distribution of SP, MP and MPCSD can be calculated by

$$P_r^{SP1}(y) = |S_1|^2, \quad P_r^{SP2}(y) = |S_2|^2, \tag{3.18}$$
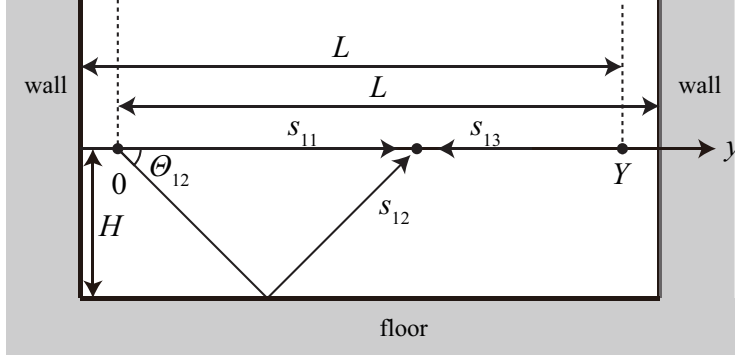
Figure 3.13 Three paths simulation model.

$$P_r^{MP}(y) \quad = \quad |S_1 + S_2|^2, \tag{3.19}$$

and

$$P_r^{MPCSD}(y) \quad = \quad |S_1|^2 + |S_2|^2, \tag{3.20}$$

respectively. It is noted that, although different frequencies are used at the two transmitters, its difference Δf is very small compared with the carrier frequency f_0, i.e. $\Delta f = 50$ Hz and $f_0 = 952.4$ MHz. Therefore, the difference on the wavelength is negligible in the simulation. Using these calculations, the numerical simulation is conducted in two cases of $I = 1$ (free space) and $I = 3$.

Figures 3.14 and 3.15 show the power distribution in free space and in ray tracing simulations respectively. In SP, when the Rx antenna is far from the corresponding Tx antenna, the received power attenuates in proportion to free space path-loss. In the case of 3 paths, different from the case in free space, standing wave is occurred due to the reflected waves. In MP, the area of energy supply field can be enhanced owing to the increased number of transmission points, as compared to that of SP. However, at the central area between the two Tx antennas, the received power is degraded by the effect of destructive interference between multiple wave sources in both the cases of free space and 3 paths. On the contrary, in MPCSD, the degraded received power at deadspots are remarkably improved in both cases.

3.4.3 Definition of coverage

In order to evaluate the energy transmission schemes, the following metric is introduced. Equation (3.21) shows our definition of coverage for wireless energy transmission.

$$c(P_{\text{req}}) = \frac{\sum_{k=1}^{K} a(k, P_{\text{req}})}{K}, \tag{3.21}$$

where k denotes a measurement point, K is the total number of measurement points, P_{req} denotes the required power to activate the sensor node, and $a(k, P_{\text{req}})$ is the activation condition which is defined as

$$a(k, P_{\text{req}}) = \begin{cases} 1 & (P_{\text{r}}(k) \geq P_{\text{req}}) \\ 0 & (P_{\text{r}}(k) < P_{\text{req}}) \end{cases}, \tag{3.22}$$

where $P_{\text{r}}(k)$ is the received power simulated or measured at point k. Therefore, the coverage expresses the ratio of area where the received power is higher than the required power P_{req} in the simulated or measured environment.

Figure 3.16 shows results of the coverage in the free space simulation. To evaluate each scheme, six special points are marked in the figure. Points (1) - (3) show the maximum available values of required powers to maintain 100% coverage in SP, MP, and MPCSD respectively. Points (4) - (6) show the crossing points among SP, MP, and MPCSD. The maximum available value in SP as seen from the point (1) is determined by transmit power, path-loss attenuation, and antenna gain. Since MP creates deadspots due to destructive interference between multiple wave sources, the maximum available value in MP is much less than that in SP and MPCSD as seen from the points (1) - (3). On the other hand, the maximum available value of MPCSD is 8.4 dB higher than that in SP as shown by the gap between point (1) and (3). In addition, the points (4) and (5) indicate that MP is only effective when supplying the power to certain sensors. Furthermore, all schemes converge to 0% at the same required power as shown from the point (6). Therefore, Fig. 3.16 shows that MPCSD is the most effective scheme to improve the uniformity of the coverage.

Figure 3.17 shows results of the coverage in the ray tracing simulation. The trend of all schemes are similar to that of free space simulation. As seen from the points (1) and (3), the coverage of SP and MPCSD is decreased compared to that of free space simulation. However, the maximum available value of MPCSD is 14.8 dB higher than that in SP. Since MPCSD can mitigate multipath effect, the gain is higher than that of free space.
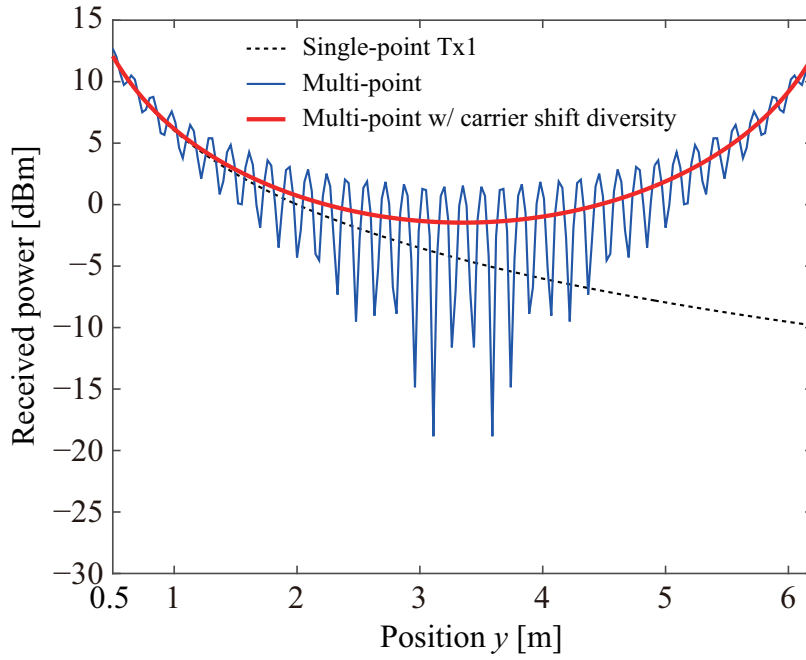
Figure 3.14 Simulation result of power distribution in free space.
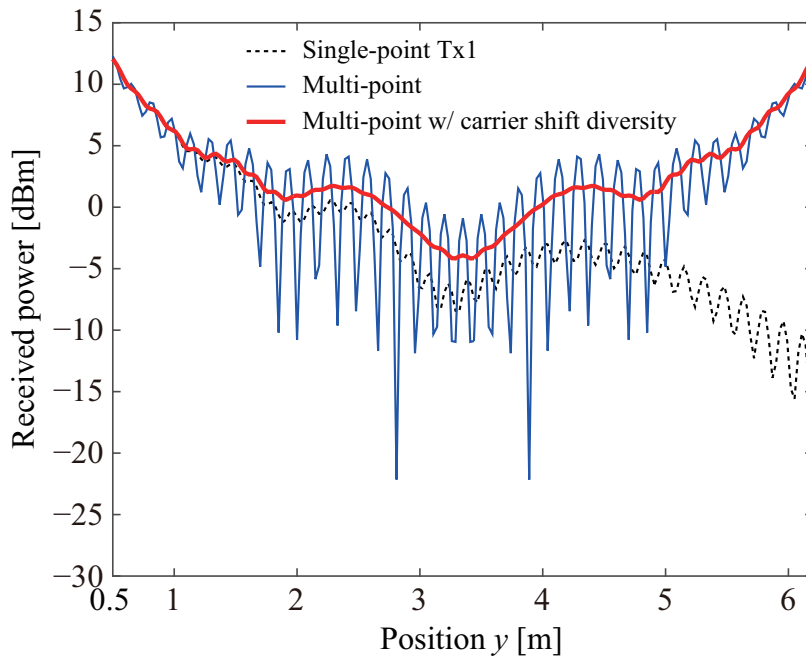
Figure 3.15 Simulation result of power distribution in 3 paths model.
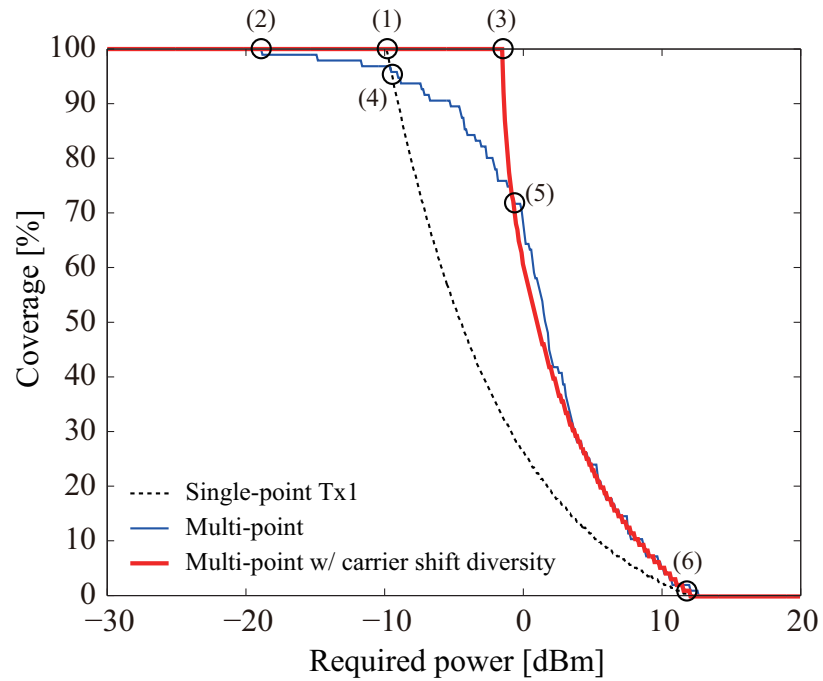
Figure 3.16   Simulation result of energy transmission coverage in free space.
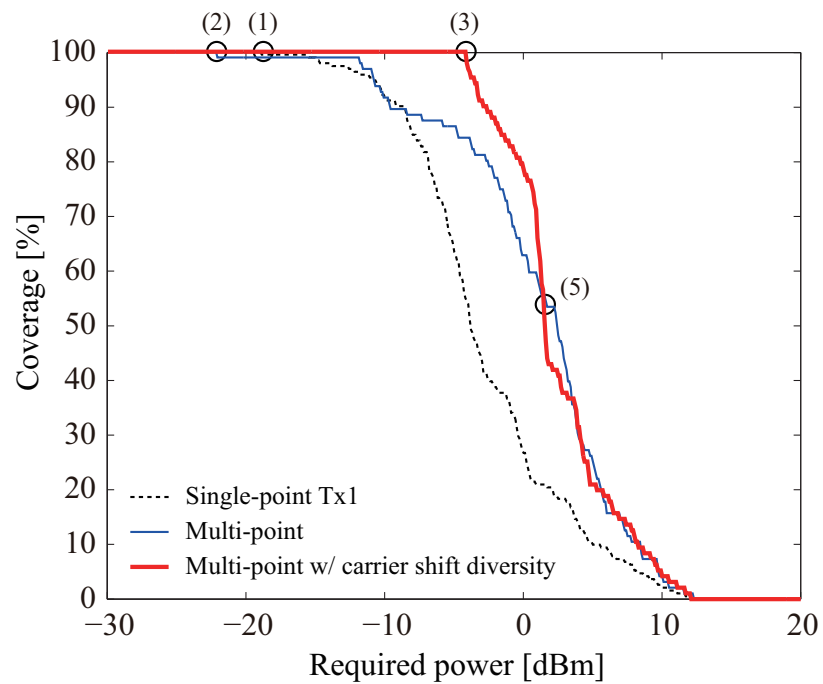
Figure 3.17   Simulation result of energy transmission coverage in 3 paths model.

3.4.4   Experiment results

Measurement results on power distributions of SP in horizontal plane and vertical plane are shown in Figs. 3.18, 3.19, 3.22 and 3.23 respectively. When the Rx antenna is far from the corresponding Tx antenna, the received power attenuates in proportion to free space path-loss in both horizontal and vertical cases. In addition, when the Rx antenna is close to the opposite wall of the Tx antenna, the received power is fluctuated due to the standing-wave effect caused by reflection from the wall. Furthermore, at the measurement point around 3.5 m in the both cases of Tx antenna $\sharp$1 and Tx antenna $\sharp$2, the received power degrades due to the standing-wave caused by the reflections from the floor (or ceiling) in horizontal plane. In vertical plane, the degraded point changes depending on Rx antenna height z, because of the phase difference between the direct wave and the reflected wave from the floor (or ceiling). The results show that the coverage is limited by path-loss attenuation and deadspots due to the standing-wave created by multipath.

The power distributions of MP in horizontal plane and vertical plane are shown in Figs. 3.20 and 3.24 respectively. In MP, the area of energy supply field can be enhanced owing to the increased number of transmission points, as compared to SP. In addition, since another Tx is additionally located at the opposite wall, the degradation due to the standing-wave caused by reflection from the wall can be reduced. However, at the central area between the two Tx antennas, the received power is severely degraded by destructive interference between the two wave sources. On the contrary, in the case of MPCSD, the degraded received power at deadspots are remarkably improved as shown in Figs. 3.21 and 3.25. In terms of the deadspots caused by multipath, the number of deadspots decreases compared with that of SP since deadspots of MPCSD occur only when both the received powers from the two single-points are degraded at the same time.

3.4.4.1   Coverage of wireless energy transmission

Figure 3.26 shows the coverage of each scheme measured in horizontal plane (x - y plane) at discrete $x = \{ -0.15, -0.12, \ldots, 0.15 \text{ m} \}$. The trend of all schemes are similar to that of free space simulation in Fig. 3.16. However, as seen from the points (1) and (3) in the figure, the coverage in SP and MPCSD is shrunken compared to that of free space simulation while the coverage in MP is almost the same value as seen from the point (2). It implies that the effect of standing-wave caused by multipath and interference between multiple wave sources decreases the coverage performances.

Figure 3.27 shows the coverage of each scheme measured in vertical plane (z - y plane) at discrete $z = \{ -0.15, -0.12, \ldots, 0.15 \text{ m} \}$. The trend of all schemes are similar to the results in

the case of free space simulation in Fig. 3.16. However, the maximum available values of required powers in SP and MPCSD vary with respect to z more remarkably as compared to the horizontal case, as seen at the points (1) and (3) in Fig. 3.27. It implies that power degradation due to reflections from the floor (or ceiling) depends on the Rx antenna height z. On the other hand, the maximum available values of required power in MP is similar to that in the horizontal case since the effect of interference between multiple wave sources is dominant compared to the effect of standing-wave caused by multipath, as seen from the point (2) in Fig. 3.27.

Finally, Fig. 3.28 shows the coverage of each scheme measured in the whole horizontal or vertical plane. In SP, the maximum available value of required power in vertical plane is lower than that in horizontal plane. It means that the effect of multipath is most dominant for SP. In MP, the values of the two cases are almost the same. It is because that the effect of interference between multiple wave sources is dominant compared to that of standing-wave created by multipath in MP. In MPCSD, the values of required power in both horizontal and vertical cases are also almost the same. It implies that the effect of standing-wave created by multipath can be reduced by MPCSD. In horizontal and vertical planes, the values in MPCSD are respectively 18.2 dB and 25.6 dB higher than that in SP as shown in the figure, so that the gain of MPCSD in this experiment is much higher than that in free space simulation. It is noted that since the results of experiments include all the reflected paths, the gain is also higher than that in 3 paths ray tracing simulation.

Due to the floor (or ceiling)

Due to the opposite wall
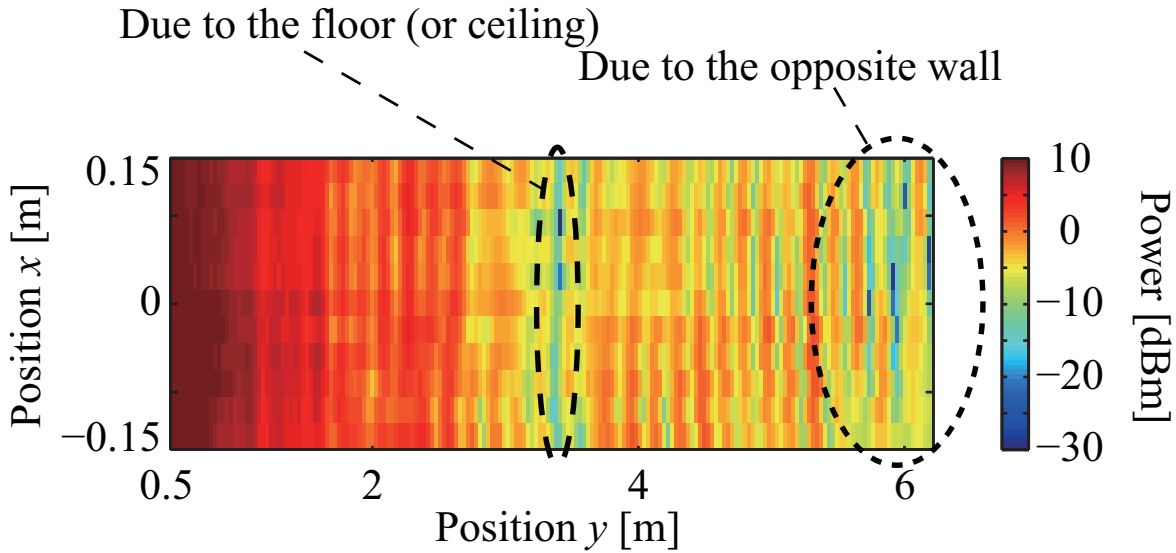
Figure 3.18   Experimental result of power distribution
of single-point wireless energy transmission (Tx♯1)
in horizontal plane.

Due to the floor (or ceiling)

Due to the opposite wall
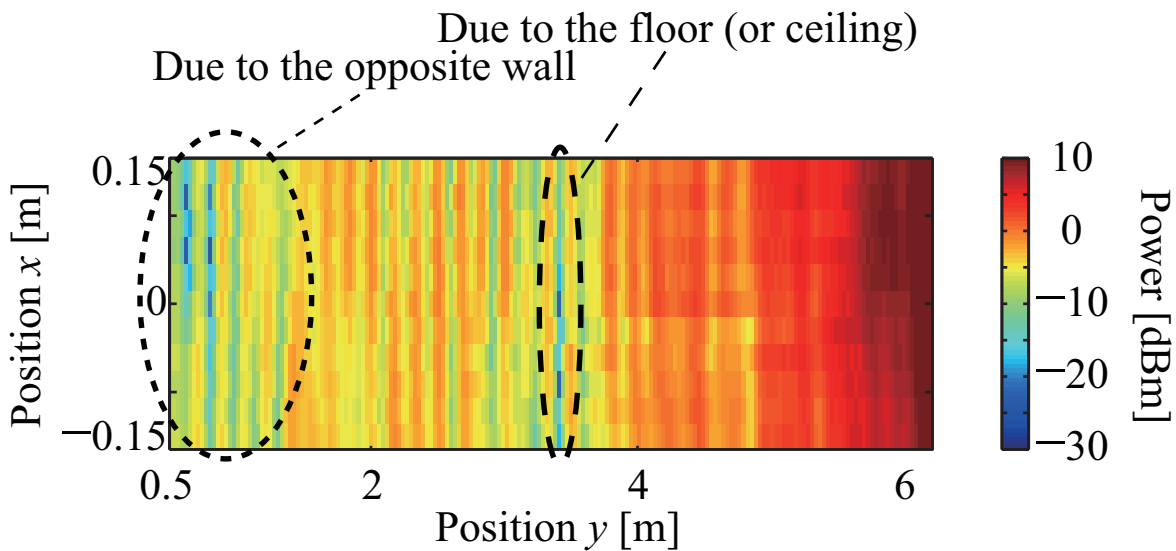
Figure 3.19   Experimental result of power distribution
of single-point wireless energy transmission (Tx♯2)
in horizontal plane.

Due to multiple wave sources
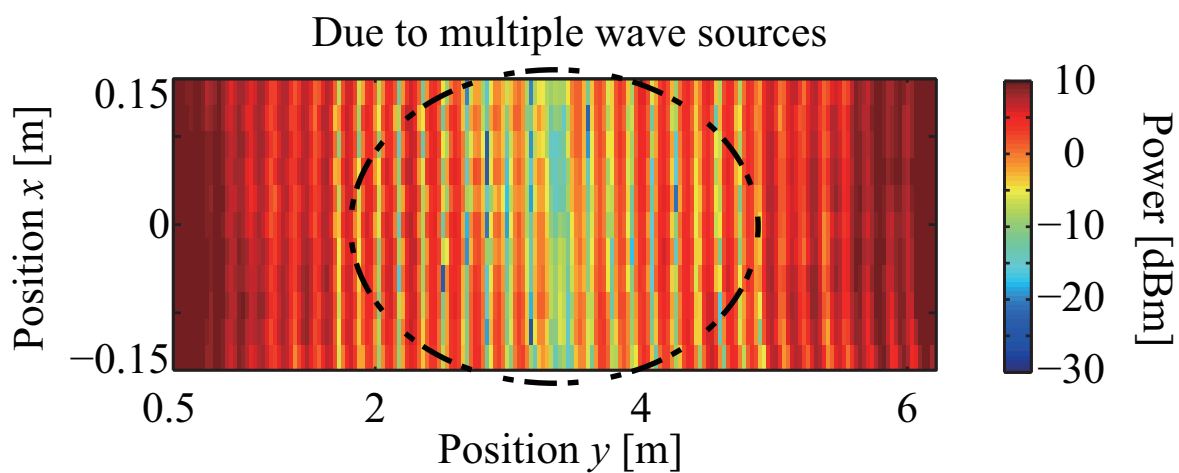
Figure 3.20 Experimental result of power distribution
of multi-point wireless energy transmission
without carrier shift diversity in horizontal plane.
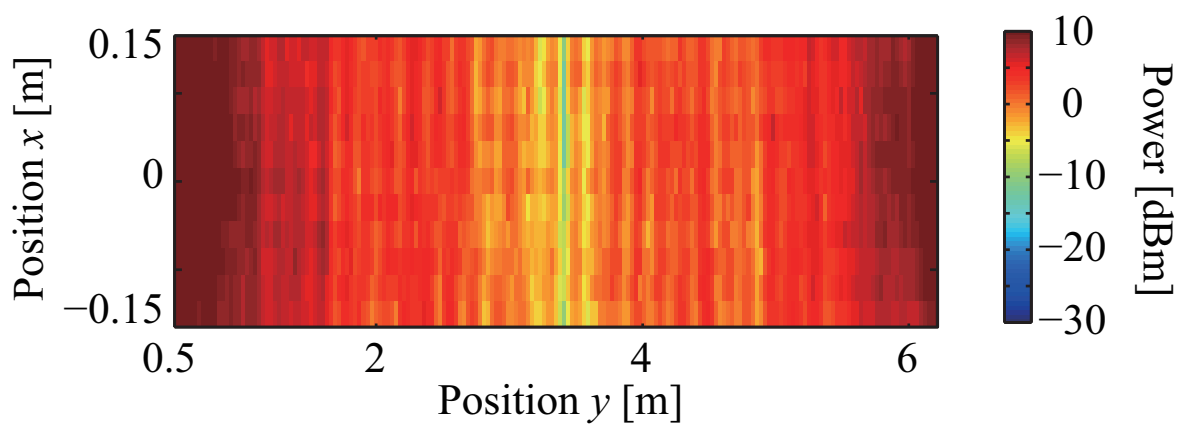
Figure 3.21 Experimental result of power distribution
of multi-point wireless energy transmission
with carrier shift diversity in horizontal plane.

Due to the floor (or ceiling)

Due to the opposite wall
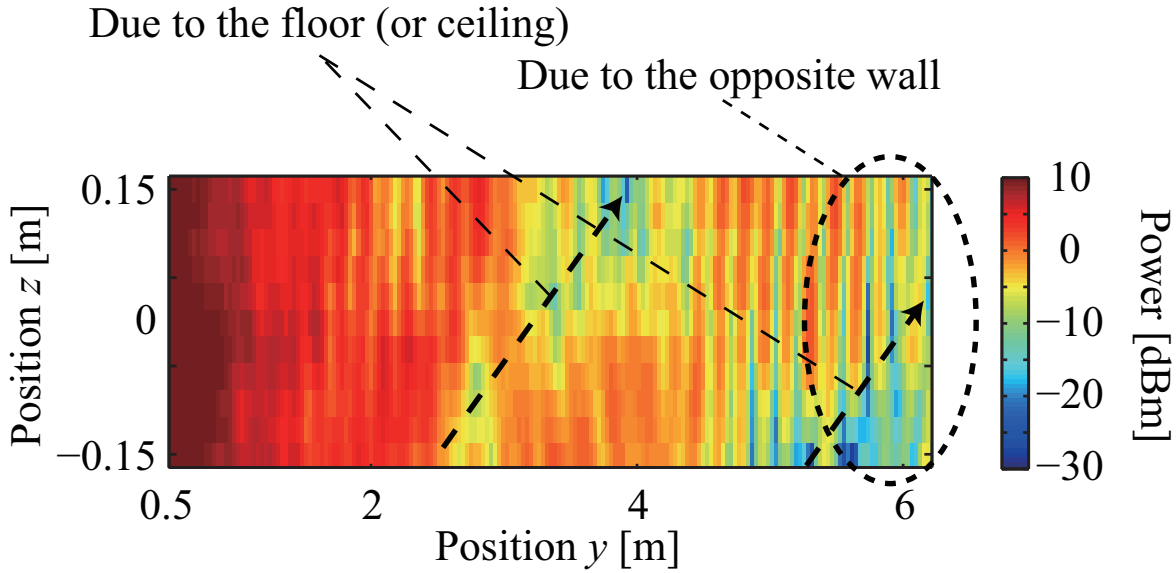
Figure 3.22　Experimental result of power distribution
of single-point wireless energy transmission (Tx♯1) in vertical plane.

Due to the floor (or ceiling)

Due to the floor (or ceiling)
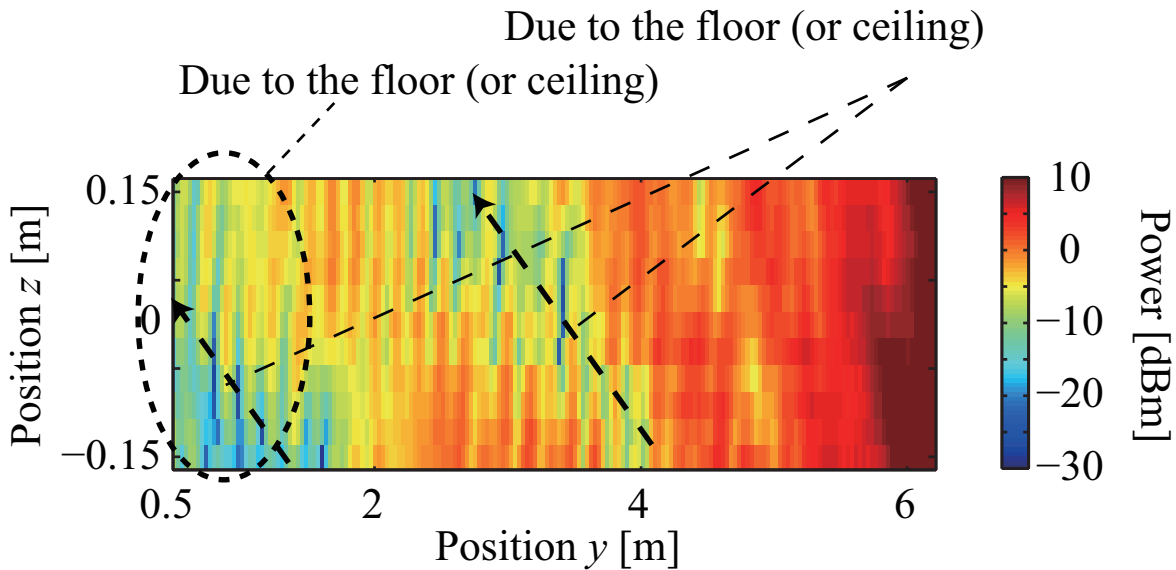
Figure 3.23　Experimental result of power distribution
of single-point wireless energy transmission (Tx♯2) in vertical plane.
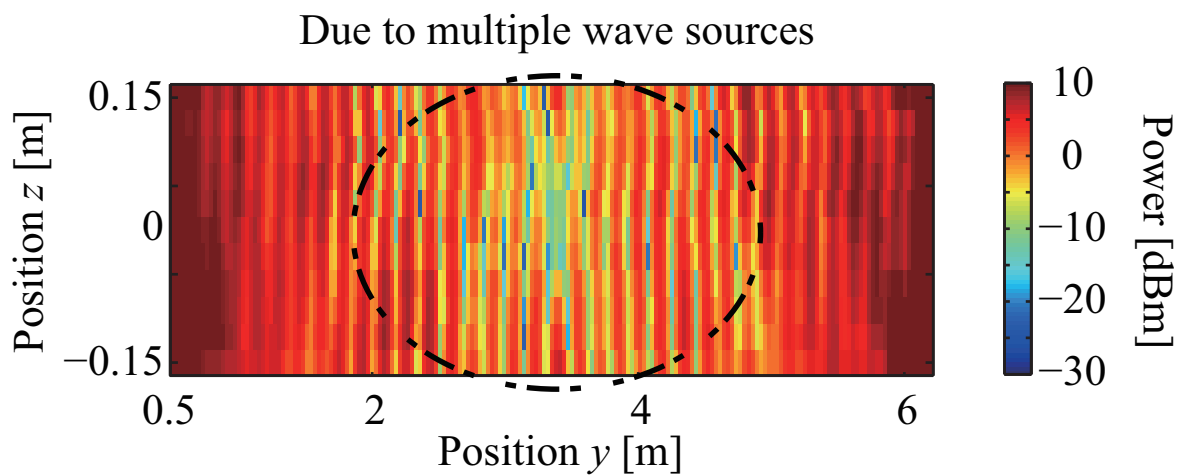
Figure 3.24 Experimental result of power distribution
of multi-point wireless energy transmission
without carrier shift diversity in vertical plane.
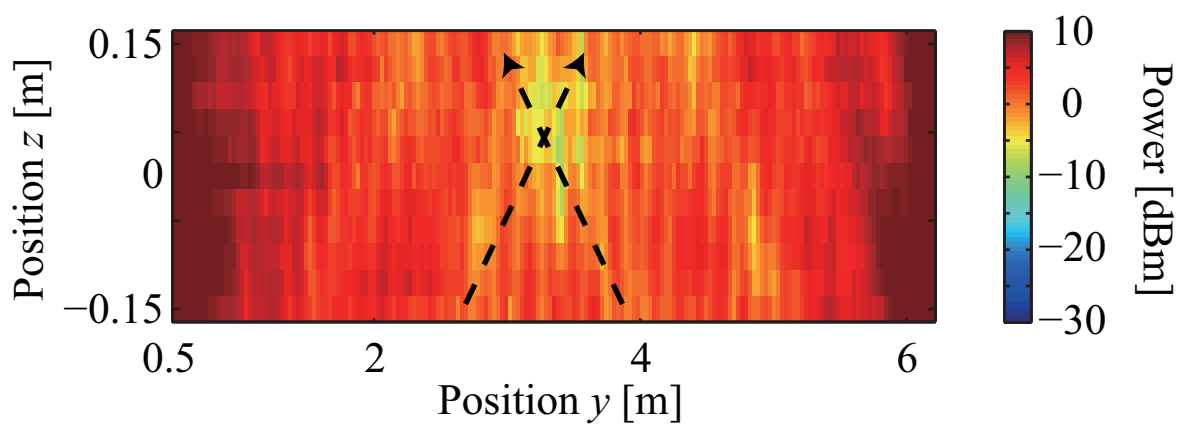
Figure 3.25 Experimental result of power distribution
of multi-point wireless energy transmission
with carrier shift diversity in vertical plane.
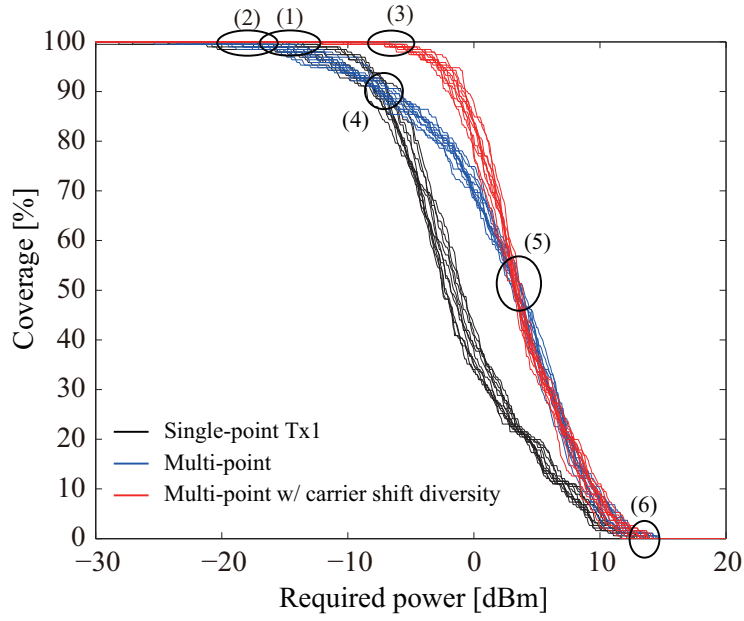
Figure 3.26   Experimental result of energy transmission coverage in horizontal plane.
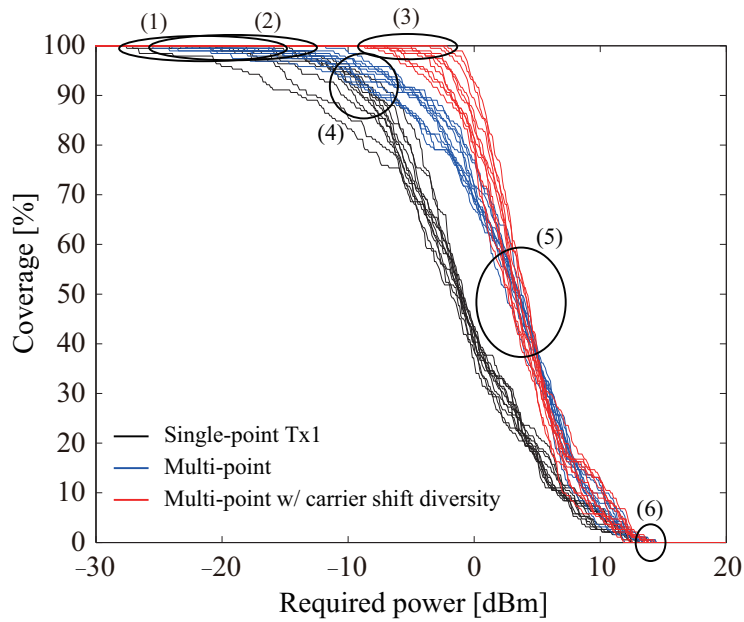
Figure 3.27   Experimental result of energy transmission coverage in vertical plane.
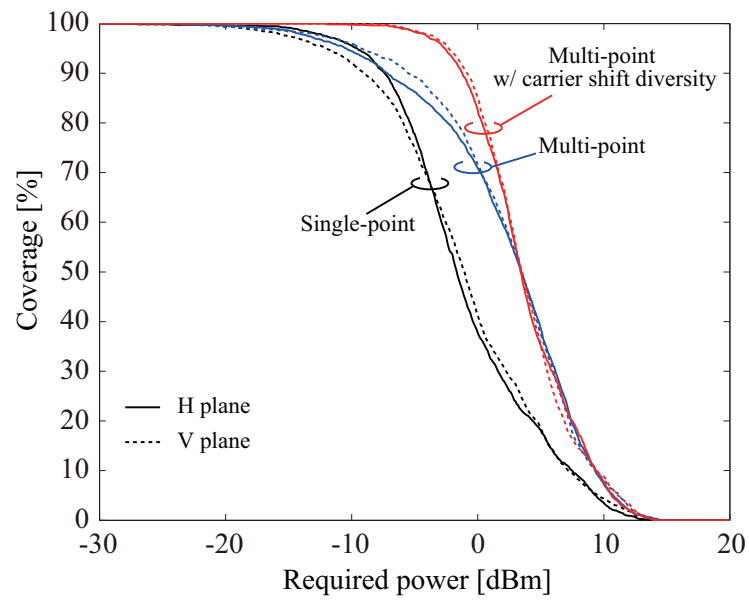
Figure 3.28 Experimental result of energy transmission coverage (overall performance).

3.5 Summary

This chapter presented the proposed multi-point wireless energy transmission with carrier shift diversity to realize seamless coverage of energy supply field, provided theoretical analysis, and conducted indoor experiments to verify the effectiveness of the proposed scheme in terms of RF propagation. We compared the received power distribution and the coverage performance of different energy transmission schemes including conventional single-point, simple multi-point and our proposed multi-point scheme. To easily observe the effect of standing-wave caused by multipath and interference between multiple wave sources, the measurements were performed in both horizontal and vertical planes and also simulated in free space and 3 paths conditions. The experimental results showed that standing-wave due to multipath and interference between multiple transmitters are dominant in the single-point scheme and in the simple multi-point scheme respectively. On the other hand, in the proposed multi-point scheme, the effect of standing-wave created by multipath and interference between multiple wave sources can be mitigated. In this experimental environment, the maximum available values of required power in the proposed scheme in horizontal and vertical planes are respectively 18.2 dB and 25.6 dB higher than that of the single-point scheme while the gain was 8.4 dB in free space simulation. It can be concluded that the proposed scheme can mitigate power attenuation due to the path-loss as well as the effect of standing-wave created by multipath and interference between multiple wave sources, so that the proposed scheme can improve the coverage of energy supply field.

Chapter 4

Activation of battery-less sensor nodes via wireless energy transmission

4.1 Introduction

Chapter 3 only conducted indoor experiments measuring the propagation characteristics using a receiving antenna of IC tag and spectrum analyzer. However, in the previous chapter, the coverage of sensor activation was not confirmed with real battery-less sensor nodes. In the scenario of real battery-less sensor node, RF/DC conversion efficiency is non-linear against received power and the consumed power varies according to the activation status of the sensor node. In this chapter, we develop battery-less sensor node composed of off-the-shelf devices and conduct indoor experiments by using the developed sensor node. In the experiments, we measure both received power and sensor activation using the developed battery-less sensor node whose consumed power and required power to activate sensor node are 140 μW and 400 μW respectively. The experimental results show that the coverage of sensor activation of the single-point scheme, the simple multi-point scheme without carrier shift diversity, and the proposed multi-point scheme are 84.4%, 83.7%, and 100% respectively.

4.2 Theory of wireless energy transmission coverage

Chapter 3 assumed that RF/DC conversion circuit was an ideal circuit of 100% conversion efficiency. However, the received power of MPCSD can be fluctuated against time and the RF/DC conversion efficiency has a non-linearity against power as mentioned in Ch. 2. Therefore, this sec-
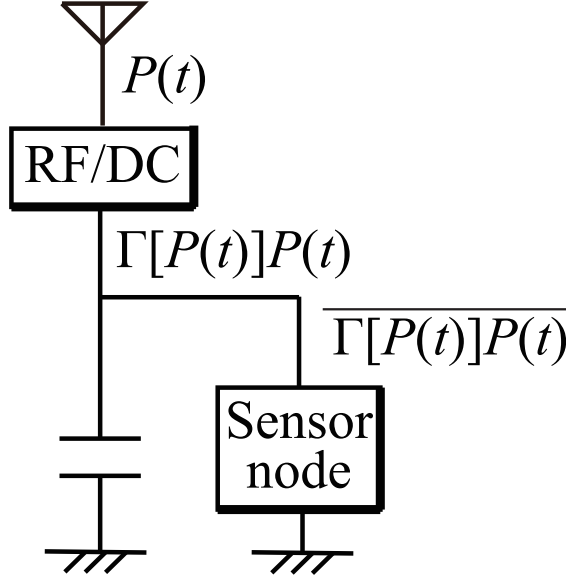
Figure 4.1   Receiver model for battery-less sensor node.

tion reconstructs the theory of the available power of sensor node by considering RF/DC conversion efficiency. The Rx model in the systems of Figs. 3.5-3.7 in Ch. 3 should be changed into Fig. 4.1 to include the concept of RF/DC conversion circuit. The RF received power $P(t)$ in Eq. (3.8) is converted into DC power as $\Gamma[P(t)]P(t)$ where $\Gamma[P(t)]$ is the RF/DC conversion efficiency at the RF received power $P(t)$. On the other hand, P_{csp} is the average consumed power of sensor node over the duty cycle T_{d}. It is noted that the consumed power is not constant against time because the sensor node employs an intermittent operation whose details will be presented in the next section. Since the MPCSD also creates fluctuation of received power over the cycle of T_{f}, the received power is averaged to $\overline{\Gamma[P(t)]P(t)}$ by a capacitor. Because the average received power should be higher than the average consumed power of the sensor node P_{csp} to permanently activate the sensor node, the activation condition Eq. (3.22) should be redefined as

$$\tilde{A}(k) = \begin{cases} 1 & \text{if } \overline{\Gamma[P(t)]P(t)} \geq P_{\text{csp}} \\ 0 & \text{if } \overline{\Gamma[P(t)]P(t)} < P_{\text{csp}}. \end{cases} \tag{4.1}$$

For further simplification of Eq. (4.1), we will introduce the low power operation of RF/DC conversion circuit, where $\partial^2\Gamma[P(t)]P(t)/\partial P(t)^2 \geq 0$ can be assumed since threshold voltage of the diodes is dominant for the efficiency in low power operation. If this assumption is satisfied, the following

inequality holds in accordance with the Jensen's inequality,

$$\Gamma[\overline{P(t)}]\overline{P(t)} \leq \overline{\Gamma[P(t)]P(t)}. \tag{4.2}$$

It is noted that [55] theoretically and experimentally verified that the output power of a time-varying signal is higher than that of its average signal in low power region. Therefore, the activation condition in Eq. (4.1) can be rewritten as

$$A(k) = \begin{cases} 1 & \text{if } \Gamma[\overline{P(t)}]\overline{P(t)} \geq P_{\text{csp}} \\ 0 & \text{if } \Gamma[\overline{P(t)}]\overline{P(t)} < P_{\text{csp}}. \end{cases} \tag{4.3}$$

From this equation, we can define the required power P_{req} to activate the sensor node as

$$P_{\text{req}} = P_{\text{csp}}/\Gamma[P_{\text{req}}]. \tag{4.4}$$

Finally, the coverage C of the activation area can be defined as

$$C = \frac{1}{K} \sum_{k=1}^{K} A(k). \tag{4.5}$$

It is noted that the derived coverage C is a lower bound due to the approximation of Eq. (4.2), especially for the case of MPCSD, while it gives the exact values of the theoretical coverage in the case of SP and MP, since the received power is constant against time as explained in Ch. 3.

4.3 Design criteria of battery-less sensor node

To extend the coverage where sensor nodes can be activated, the consumed power of the sensor node should be as low as possible. To reduce the power consumption, an intermittent operation of data transmission can be introduced and operated by MCU. Since the consumed power of sensor is generally much less than that of RF process, only RF process is performed periodically. On the other hand, because sensor often has initialization time for e.g. calibration, the sensor itself is always active. In addition, a capacitor equipped in the sensor node also plays the role of a rechargeable battery which recharges the surplus energy in the sleep mode so that the sensor nodes can be stably activated even when the consumed power of data transmission is larger than that of the output power of the rectifying circuit. Here, the consumed power of sensor node is described as

$$P_{\text{csp}}(t) = \begin{cases} P_{\text{s}} & (0 < t \leq T_{\text{s}}) \\ P_{\text{Tx}} & (T_{\text{s}} < t \leq T_{\text{d}}), \end{cases} \tag{4.6}$$

where $T_s (= T_d - T_{Tx})$ and T_{Tx} are the duration of the sleep and Tx modes respectively, T_d is the duty cycle, P_s is the consumed power in the sleep mode, and P_{Tx} is the consumed power in the Tx mode as shown in Fig. 4.2 (a). From Eq. (4.6), the average consumed power becomes

$$P_{csp} = \frac{1}{T_d} \left(\int_0^{T_s} P_s dt + \int_{T_s}^{T_d} P_{Tx} dt \right). \tag{4.7}$$

Based on this equation, the average consumed power P_{csp} can be reduced by increasing T_d or decreasing P_{Tx} and P_s. Because T_d is determined by the application of WSN, the other two factors should be as low as possible.

In order to manage the intermittent operation while reducing the size of sensor node, the value of capacitor should be designed carefully. In the capacitor, the stored energy should be higher than the required energy of Tx mode. When the received power is the same with required power $P_r = P_{req}$, the following condition should be hold at the capacitor to activate the sensor node,

$$
\begin{aligned}
\frac{\mathfrak{C}}{2} \left[V_c^2(T_s) - V_c^2(T_d) \right] &\geq (P_{Tx} - P_{req} \Gamma[P_{req}]) T_{Tx} \\
&= (P_{Tx} - P_{csp}) T_{Tx},
\end{aligned} \tag{4.8}
$$

where $\mathfrak{C}$ is the value of the capacitance and $V_c(t)$ is the voltage at the capacitor at time t as shown in Fig. 4.2 (b). Therefore, the minimum required capacitance $\mathfrak{C}_{min}$ can be calculated as

$$\mathfrak{C}_{min} = 2 T_{Tx} \frac{P_{Tx} - P_{csp}}{V_c^2(T_s) - V_c^2(T_d)}. \tag{4.9}$$

In Eq. (4.3), the output power of rectenna is averaged over the period of the cycle of artificial fading T_f. The cycle and the frequency offset should be designed as

$$1/\Delta f = T_f \ll T_d. \tag{4.10}$$

Therefore, the activation via MPCSD can be defined as the condition of power Eq. (4.3), energy Eq. (4.9) and cycle Eq. (4.10).

4.4 Development of battery-less sensor node

This section presents the developed battery-less sensor node based on the design criteria in the previous section and measures power consumption of the sensor node and RF/DC conversion circuit.

4.4.1 Prototype Hardware

Table 4.1, Figs. 4.3 and 4.4 describe the components of the prototype hardware. The battery-less sensor node mainly consists of a power receiving antenna in Fig. 4.4 (a), a rectifying circuit including a capacitor of 50 mF in Fig. 4.4 (b) [73], and a sensor node in Fig. 4.4 (c) including an RFIC, a MCU and an IR human detection sensor. The RF energy is received by the antenna and is converted to DC required for RF module by the rectifying circuit. The MCU in the RF module manages the data transmission, while reducing the power consumption. For the developed sensor node, the minimum value of capacitance is calculated as about $600\ \mu$F by substituting parameters measured in the next section (T_{Tx} = 10 ms, P_{Tx} = 13.8 mW, P_{csp} = 142 μW) and the typical and minimum operating voltage of the sensor node ($V_{\text{c}}(T_{\text{s}})$ =2.3 V, $V_{\text{c}}(T_{\text{d}})$ =2.2 V) into Eq. (4.9). However, our developed sensor node employs a 50 mF capacitor since we use a pre-implemented capacitor on the RF/DC conversion board. It is noted that because the actual size of RF/DC conversion circuit including DC/DC converter is much less than that of evaluation board, capacitor or power receiving antenna would be dominant for the whole size of rectenna as shown in Fig. 4.4.

Figure 4.5 shows the operation flow of sensor node to reduce consumed power. In the sleep mode, only the sensor is activated because the human detection sensor requires a long initialization time of 15 s while low power consumption is realized by sleeping the MCU and RFIC. After the MCU is activated by itself in the Tx mode, the MCU performs data transmission with carrier sensing. It is noted that even if the data transmission cannot be performed due to collision avoidance, the MCU returns to the sleep mode because the power consumption of the carrier sensing is almost the same as that of data transmission. In the developed sensor node, the duty cycle is set to 1 s since we assume an application of human detection.
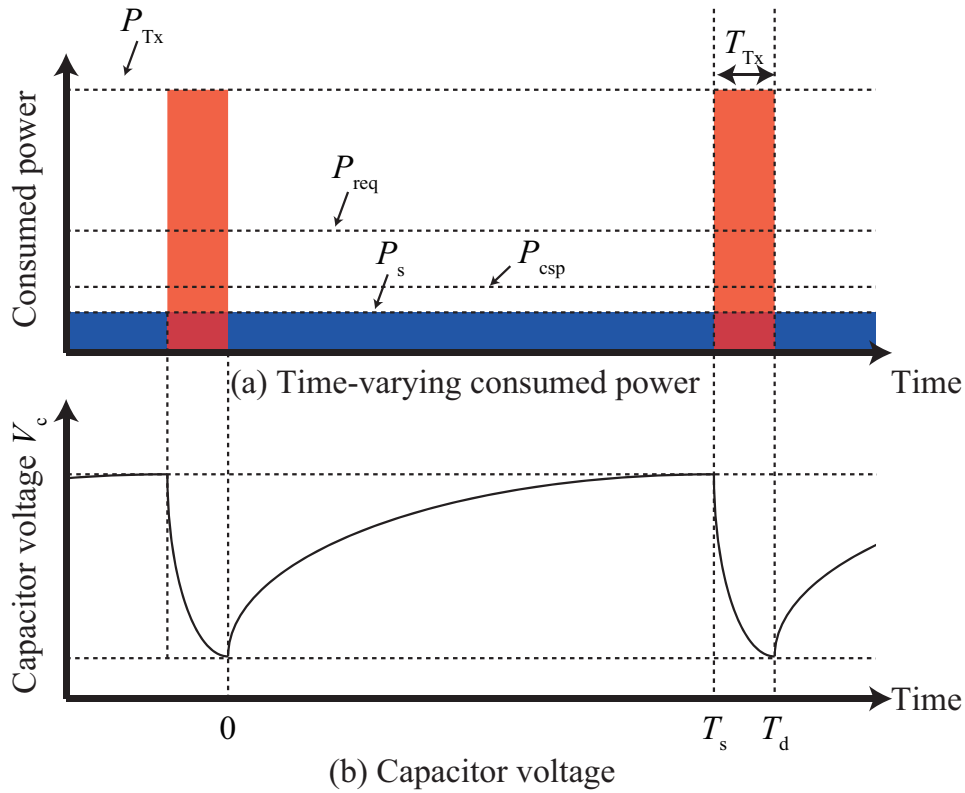
Figure 4.2 Concept of intermittent operation.

Table 4.1 Components of battery-less sensor node.

RF module	Custom made (TESSERA Technology)
RF device	ADF7023-J (Analog Devices)
MCU	R5F100GJ (Renesas Electronics)
Human detection sensor	EKMB1101111 (Panasonic)
RF/DC conversion circuit	P1110EVB (Powercast)
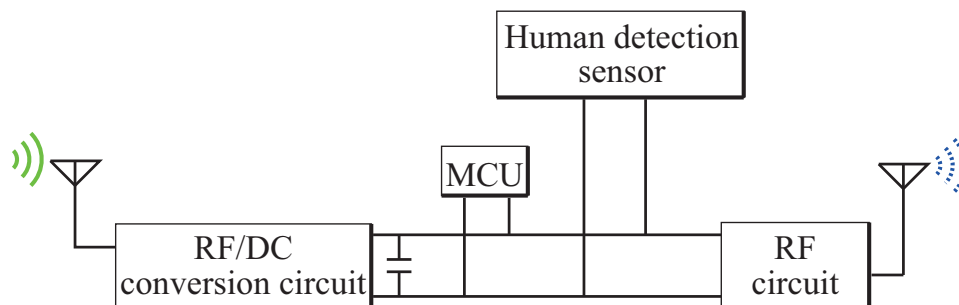
Figure 4.3   Architecture of battery-less sensor node.

Unit: mm
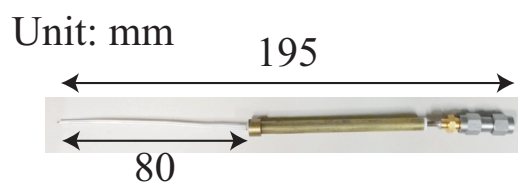
(a) Rx antenna
for power recieving
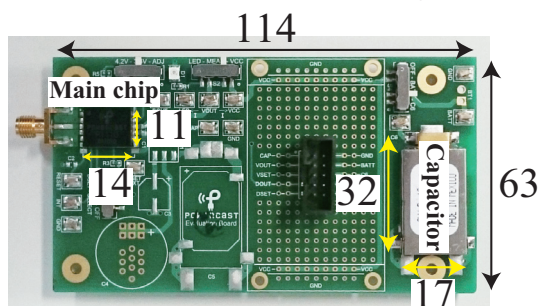
(b) Rectifying circuit (P1110EVA)
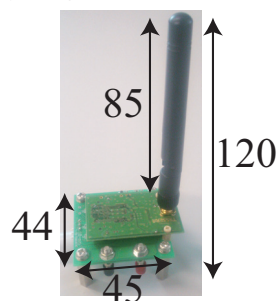
(c) Sensor node

Figure 4.4   Components of battery-less sensor node (Photo).
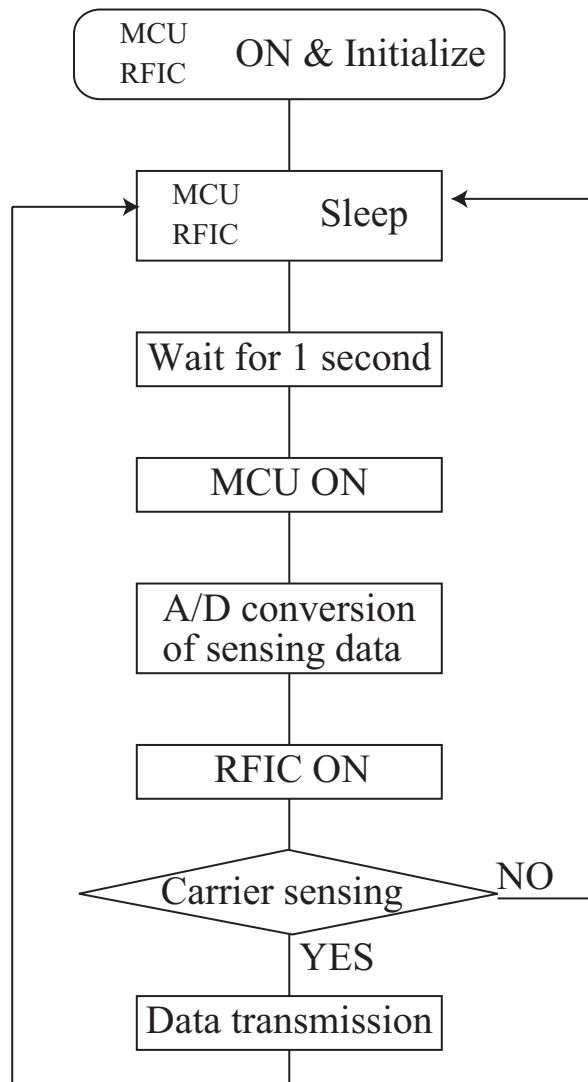
Figure 4.5 Activation flow of sensor node.

4.4.2 Measurement on power consumption

In order to understand the effectiveness of the intermittent operation and low Tx power of data transmission, the consumed current is measured. Figure 4.6 shows the measured consumed current of the sensor node in 3 s. As shown in Fig. 4.6, the data transmission is performed every 1 s. Figure 4.7 shows the consumed current of the sleep mode in 30 ms. In the sleep mode, the consumed power is about 4 μW. Figures 4.8-4.10 show the consumed current of the sensor node in Tx mode. In these figures, the red lines (*case0*) show the proposed operation in the case when both RF circuit and MCU employ sleep mode. The black lines in Figs. 4.8-4.10 show the consumed current in the case when both RF circuit and MCU do not employ the sleep mode (*case1*), when only MCU employs the sleep mode (*case2*) and when only RF circuit employs the sleep mode (*case3*) respectively. In these configurations, the average consumed powers are 140 μW (*case0*), 5.89 mW (*case1*), 2.35 mW (*case2*), and 3.72 mW (*case3*), respectively. As shown in the figures, Tx mode lasts for about 10 ms so that the duty factor is 1/100. Under the duty factor, the intermittent operation can reduce the consumed power to less than that of 1/10. It is noted that the voltage is set to a constant value of 2.3 V in the current measurement.

In Fig. 4.11, the red line shows the consumed current in the case when the Tx power of data transmission is set to -13 dBm (*case0*) while the black line shows that with 13 dBm (*case4*) which is the hardware limitation of maximum Tx power. As shown in Fig. 4.11, the data transmission is performed at the time around 15 ms and lasts for 4 ms. In addition, the consumed current of data transmission in *case0* can be reduced from about 45 mA to about 10 mA. In addition, Fig. 4.12 shows the consumed power of sensor node against the Tx power. The curve is similar to the data sheet of power amplifier of RF circuit [36]. It is noted that because the amplifier might have multiple functions depending on the output power, the curve is not smooth. By using sensor node of *case0* and the commercial product of rectifying circuit, the required power of battery-less sensor node becomes about 400 μW ($P_{\text{req}} \approx -4$ dBm) which is measured by employing a signal generator with a variable input power into the RF/DC circuit.

4.4.3 Measurement on RF/DC conversion efficiency

In order to understand the property of the RF/DC conversion efficiency, we setup a preliminary experiment to measure the efficiency by inputting signal with variable power generated by signal generator into the RF/DC conversion circuit and observing the voltage of the capacitor. Here, the output of RF/DC circuit is connected to a sensor node configured in sleep mode, knowing that in

actual situation an operating sensor node will spend most of its duty cycle in sleep mode. Because the difference between the output power of the RF/DC circuit and the consumed power in sleep mode should be stored in the capacitor, the following equation should be hold.

$$(P_{in}\Gamma[P_{in}] - P_s)T = \frac{\mathfrak{C}}{2}(V_c^2(T) - V_c^2(0)),\tag{4.11}$$

where P_{in} is the input power and T is the measurement time. From this equation, the RF/DC conversion efficiency can be derived as

$$\Gamma[P_{in}] = \left(\frac{\mathfrak{C}}{2T}(V_c^2(T) - V_c^2(0)) + P_s\right)/P_{in}.\tag{4.12}$$

Here, the capacitance $\mathfrak{C}$ of 50 mF is the same with the developed sensor node and the measurement time T of 20 s is the same as that of the experiment presented in the next section.

Figure 4.13 shows the result of the preliminary measurement. As shown in the figure, the efficiency has non-linearity against input power. However, the output power is monotonically increases against the input power, so that the required power can be defined as the threshold power to activate the sensor node. It is noted that when $P_{in} = P_{req} = -4$ dBm, the output power is almost the same with the average consumed power of the sensor node measured in the previous section. In addition, from this result, we have confirmed that the assumption $\partial^2\left(\Gamma[P_r(l)]P_r(l)\right)/\partial P_r(l)^2 \geq 0$ holds in the region where the output power is less than 1 mW (0 dBm).
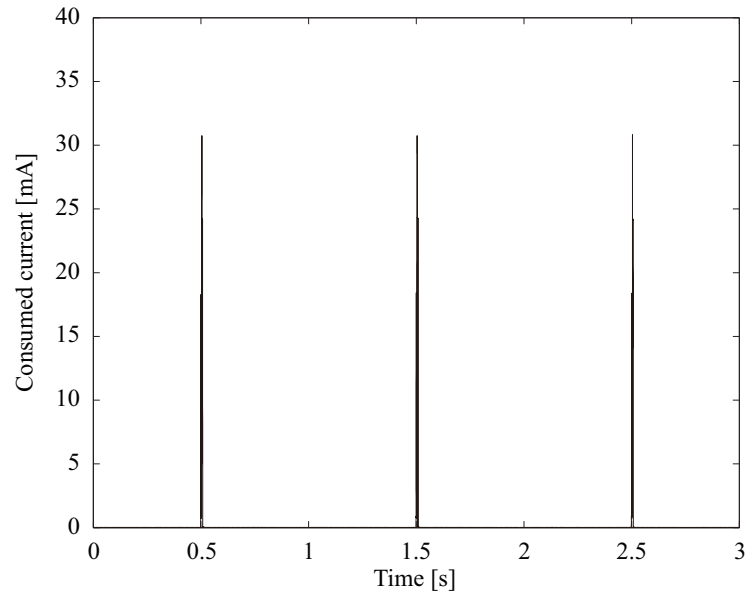
Figure 4.6   Measurement result of consumed current of battery-less sensor node in 3 s.
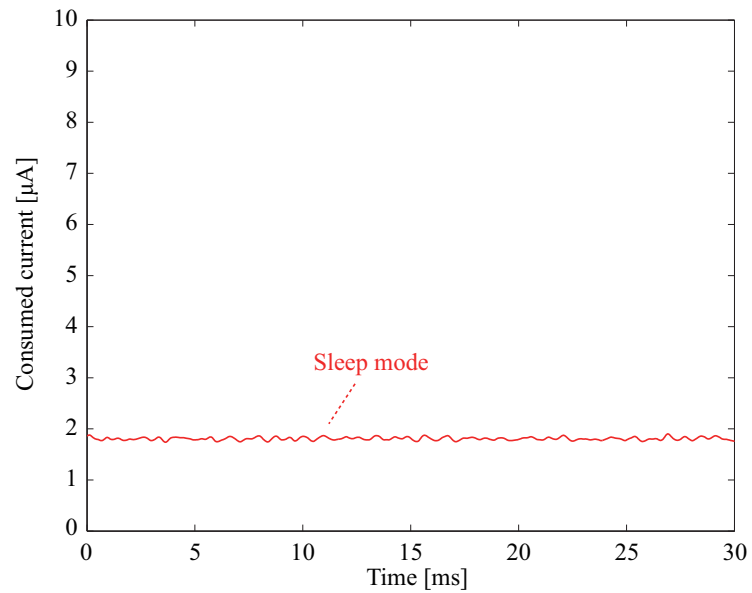
Figure 4.7   Measurement result of consumed current of battery-less sensor node in sleep mode.
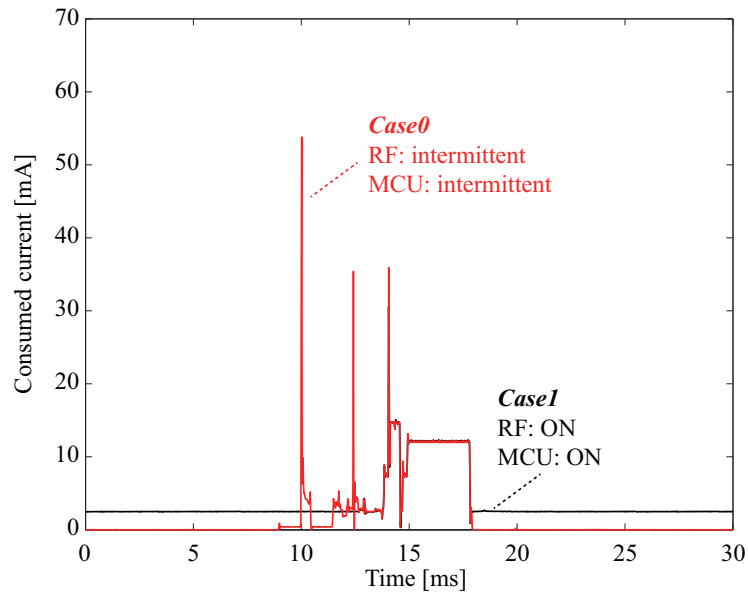
Figure 4.8   Measurement result of consumed current of battery-less sensor node in Tx mode (Case1: MCU and RFIC always ON).
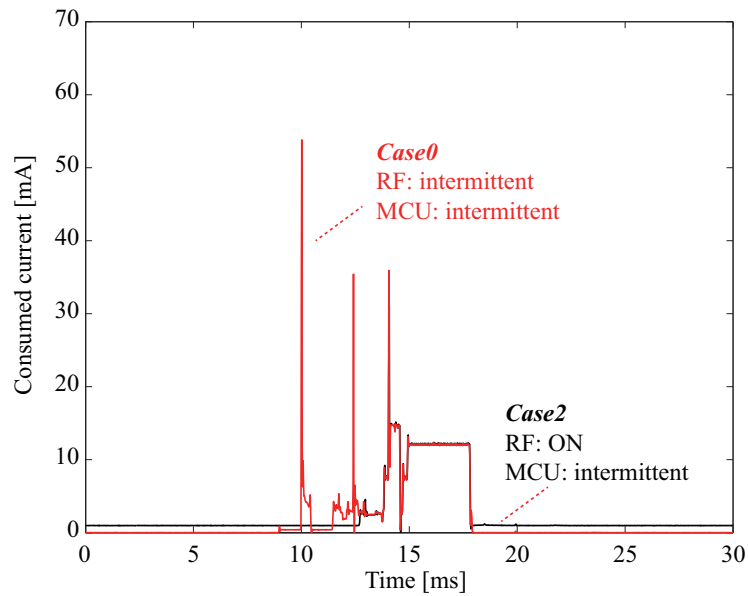
Figure 4.9   Measurement result of consumed current of battery-less sensor node in Tx mode (Case2: RFIC always ON).
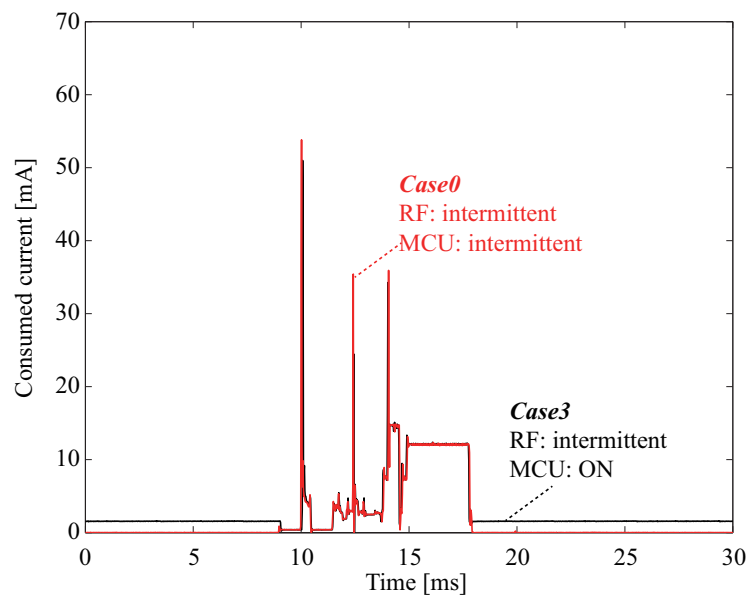
Figure 4.10 Measurement result of consumed current of battery-less sensor node in Tx mode (Case3: MCU always ON).
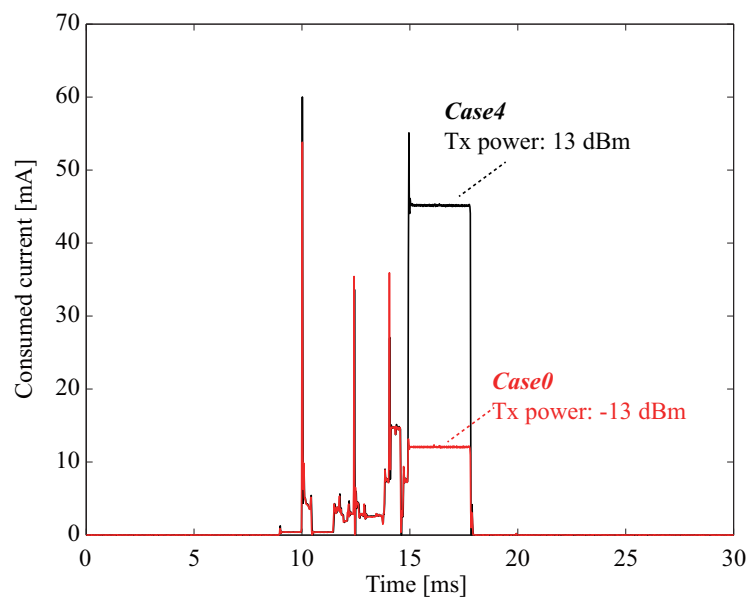
Figure 4.11 Measurement result of consumed current of battery-less sensor node in Tx mode (Case4: increase Tx power).
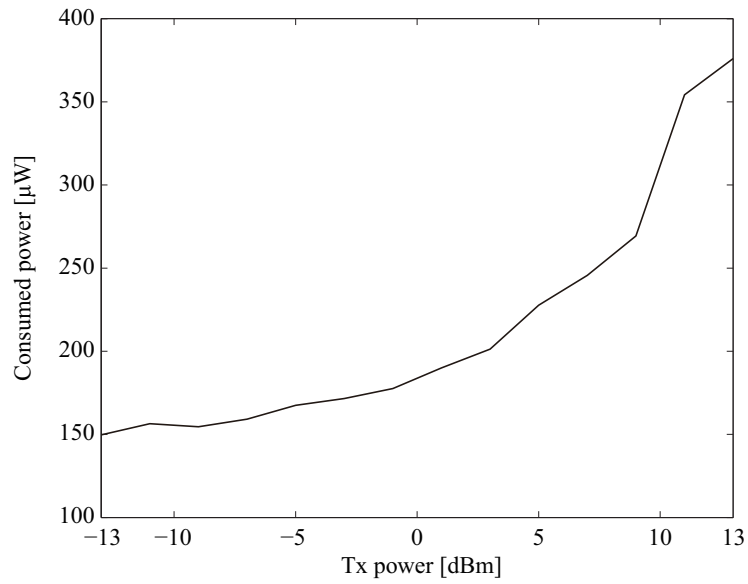
Figure 4.12   Measurement result of relationship between consumed power and Tx power of data transmission.
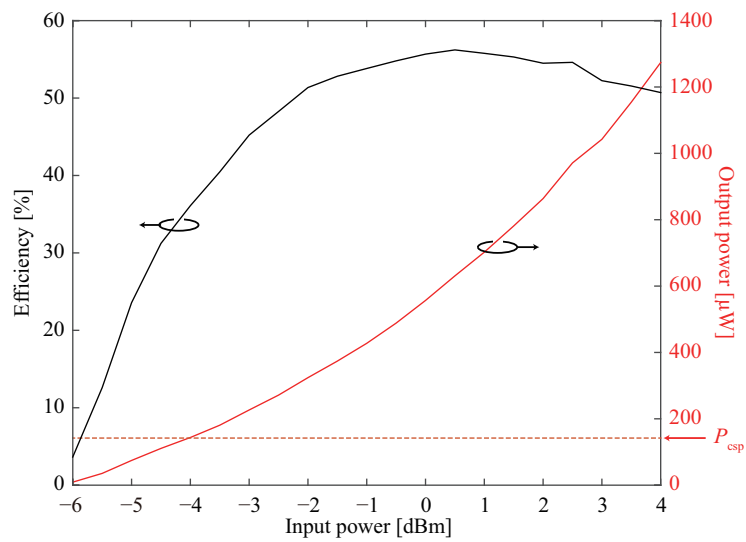
Figure 4.13   Measurement result of RF/DC conversion efficiency.

4.5   Experimental verification

In order to verify the activation possibility of the battery-less sensor node via MPCSD, we conduct indoor experiments as shown in Fig. 4.14, assuming an application of human detection system, where 2 transmitters and 1 receiver, which is moved between 2 transmitters, are set along the straight line as with the experiments in Ch. 3. Different from the experiments in Ch. 3, vertical polarization is employed to achieve 100% activation coverage of sensor node, real battery-less sensor node is employed, and the activation possibility is measured by observing the voltage of capacitor.

4.5.1   Experimental method

Table 4.2, Figs. 4.14 and 4.15 show the experimental parameters and the experimental environment respectively. At the Tx, EIRP is set to 36 dBm and the center frequency is set to 916.8 MHz at which transmission without carrier sensing is allowed. The carrier offset is set to 1 kHz to generate the cycle of artificial power fluctuation of 1 ms which is much faster than 1 s of the duty cycle. The measurement is performed along the straight line between Tx ♯1 and ♯2 as shown in Fig. 4.14. Both the Tx and Rx antennas are equipped at the same height of 0.82 m which is the same as that of desks. The height of the antennas might have the impact of the propagation due to the multipath effect. However, as Ch. 3 has already validated the effectiveness of our proposed method in terms of received power by experiments of horizontal and vertical planes, the conclusion of the experimental validation in this chapter for sensor activation can be generalized for the scenario. In the cases of MP and MPCSD, two transmitters are synchronized by the 10 MHz oscillator. Finally, in the configuration of the data transmission, the center frequency is set to be far from that of energy transmission to avoid interference. The data rate and modulation conform to IEEE 802.15.4 [20] [74].

Figure 4.16 shows the flowchart of the experiments. To keep the fairness for all measurement points, a capacitor is charged/discharged to be 2.3 V before the measurement. In the experiment, the definition of the activation is judged by whether the measured voltage is increased (active) or decreased (inactive) in 20 s. Figures 4.17 and 4.18 show examples of the capacitor voltage when the sensor node is active and inactive respectively. Since IR sensor takes several seconds for initial activation, at the first step of the measurements, a PC with data receiver checks whether sensor is activated or not. If sensor node is not activated, the measurement is stopped in 15 s until finishing the initialization of IR sensor. After the voltage setup, RF received power is measured and the voltage of the capacitor is measured in 20 s.

Figure 4.19 shows the receiver network. RF signal is received at the power receiving antenna and the signal is transfered to the RF/DC conversion circuit through a 20 dB directional coupler whose coupled line is connected to a spectral analyzer measuring the received power. The output of RF/DC conversion circuit is connected to the sensor node and a DC analyzer to measure the voltage of the capacitor. In general, the antenna port of the rectifying circuit connected to the output of the coupler is not designed for 50Ω network, while the power receiving antenna, directional coupler and S/A is designed for 50Ω network. Therefore, the impedance mismatch could occur between 50Ω and non-50Ω networks and results in the discrepancy between the real received power and the measurement value of S/A. In addition, the impedance of the non-50Ω network varies against the input power of the rectifying circuit due to the diode's non-linearity and against the voltage of the capacitor. In other words, the impedance is a function of the input power. [75] [76] have shown the degradation of the efficiency due to the impedance mismatch and proposed the adjustment of the impedance by controlling DC load to improve the efficiency for different power levels. In this experiment, because the rectifying circuit is designed to connect 50Ω antenna, the mismatch effect can be mitigated. In addition, the large value of the capacitor of 50 mF and the coupler isolation of 20 dB suppress the mismatch effect. By a test measurement, in which the rectifying circuit is directly input from a signal generator, it is confirmed that the measurement errors at the spectrum analyzer are less than 1 dB as shown in Fig. 4.20.

Table 4.2 Experimental parameters.

	Parameter	Value
Tx	Tx power	30 dBm
	Center frequency of energy transmission	916.8 MHz
	Carrier shift	1 kHz
	Antenna gain	6 dBi
	Distance between 2 Txs	6 m
Rx	Measurement point interval	3 cm $\approx \frac{\lambda}{10}$
	Center frequency of data transmission	927.6 MHz
	Data rate	100 kbps
	Modulation	Gaussian FSK
	Antenna gain	2.15 dBi
	Required power	400 μW (≈ -4 dBm)

10MHz
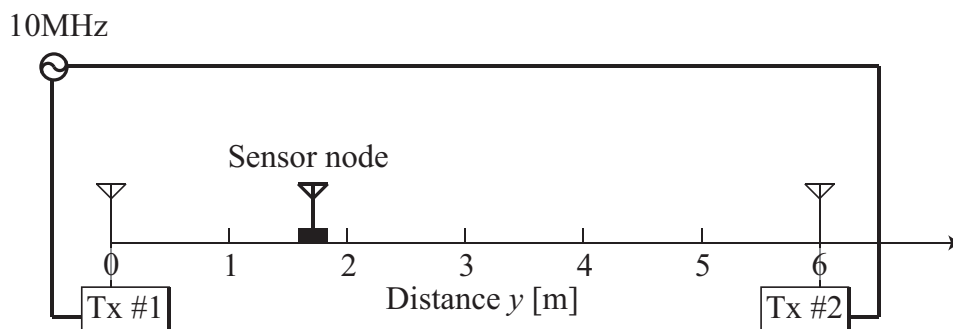
Figure 4.14 Experimental environment.
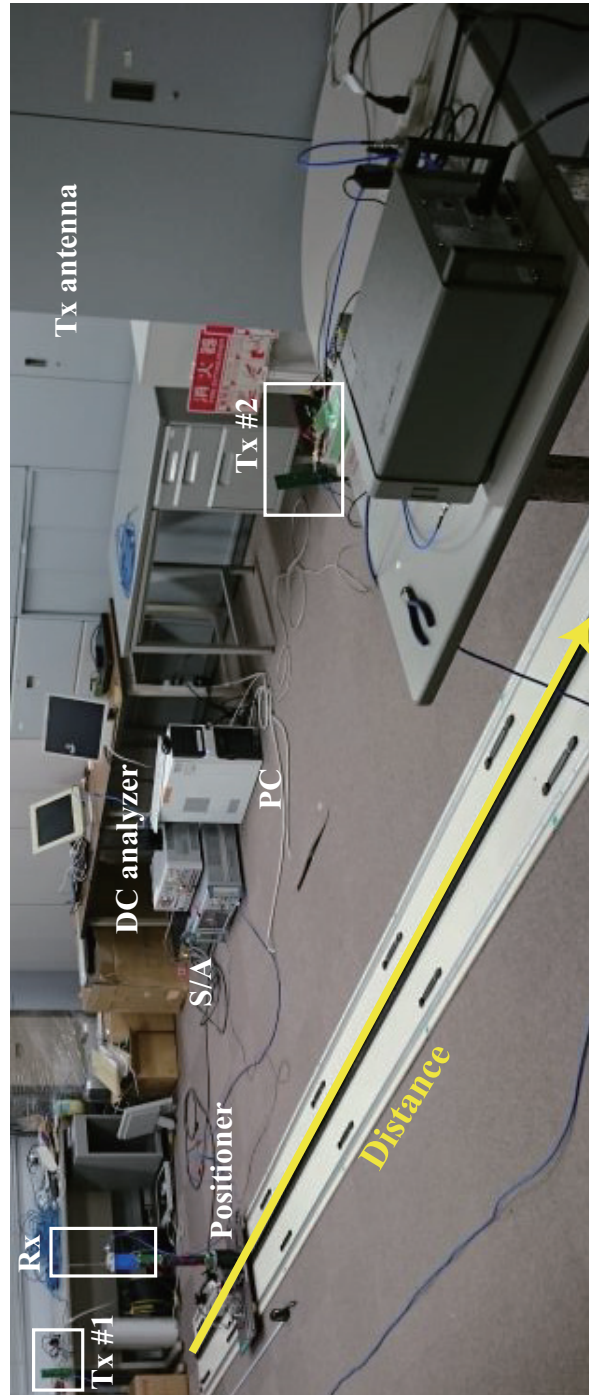
Figure 4.15 Experimental environment (Photo).

Begin

Receive sensing data ?

Yes

No

Charge or discharge capacitor

Charge or discharge capacitor

V_c = 2.3 V ?

No

Yes

V_c = 2.3 V ?

No

Yes

Wait 15 s

RF power measurement

V_c measurement for 20 s

Move positioner
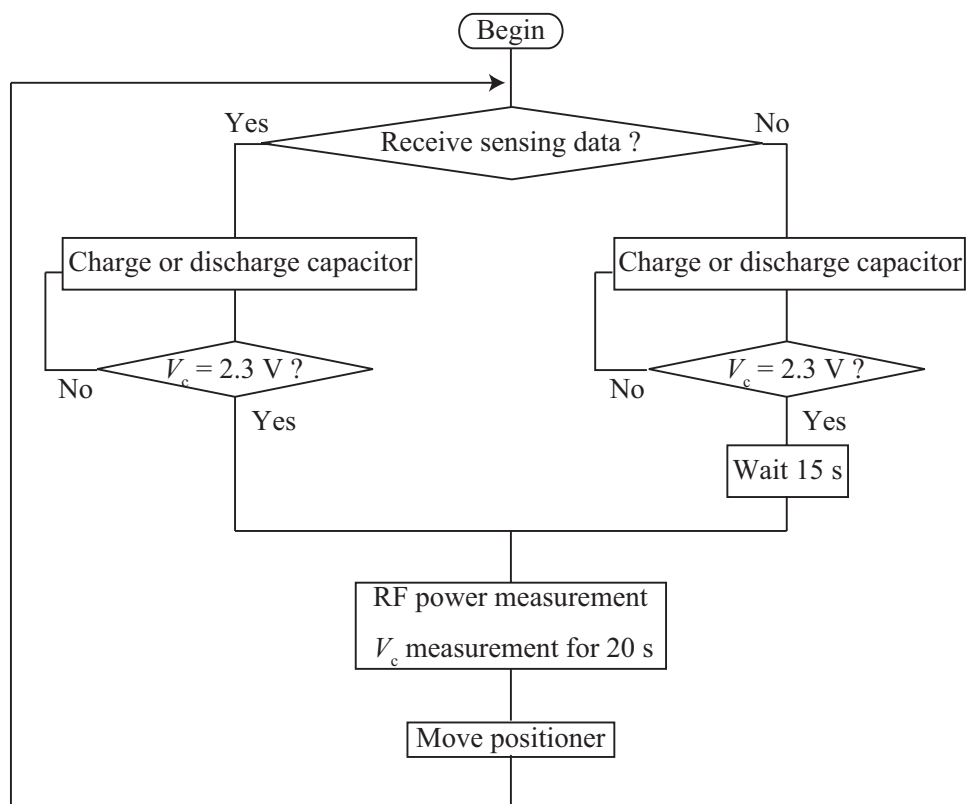
Figure 4.16 Experimental flow.
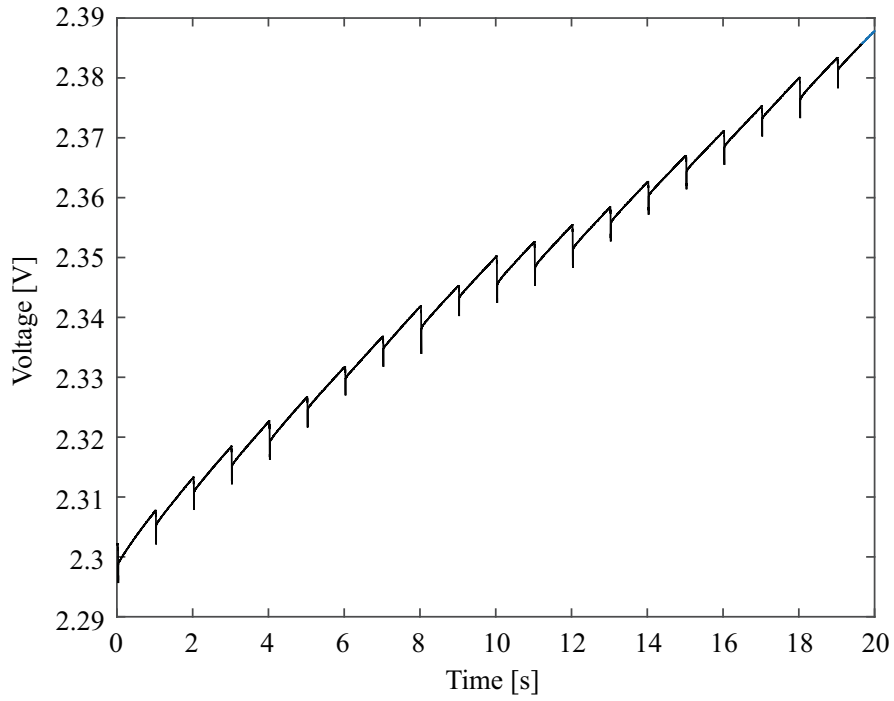
Figure 4.17   Example of increasing capacitor voltage.
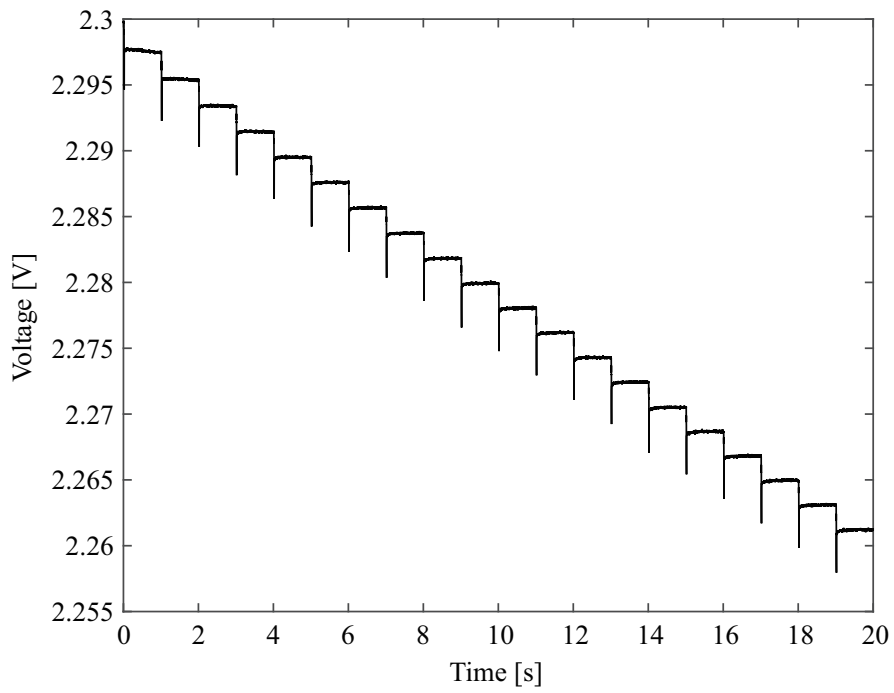
Figure 4.18   Example of decreasing capacitor voltage.
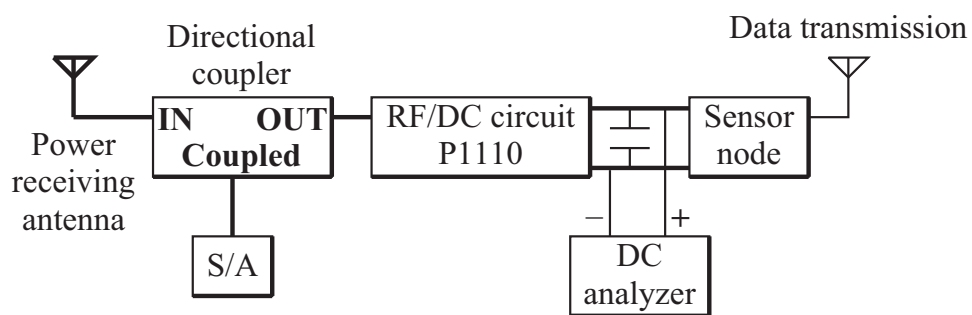
Figure 4.19   Receiver network.
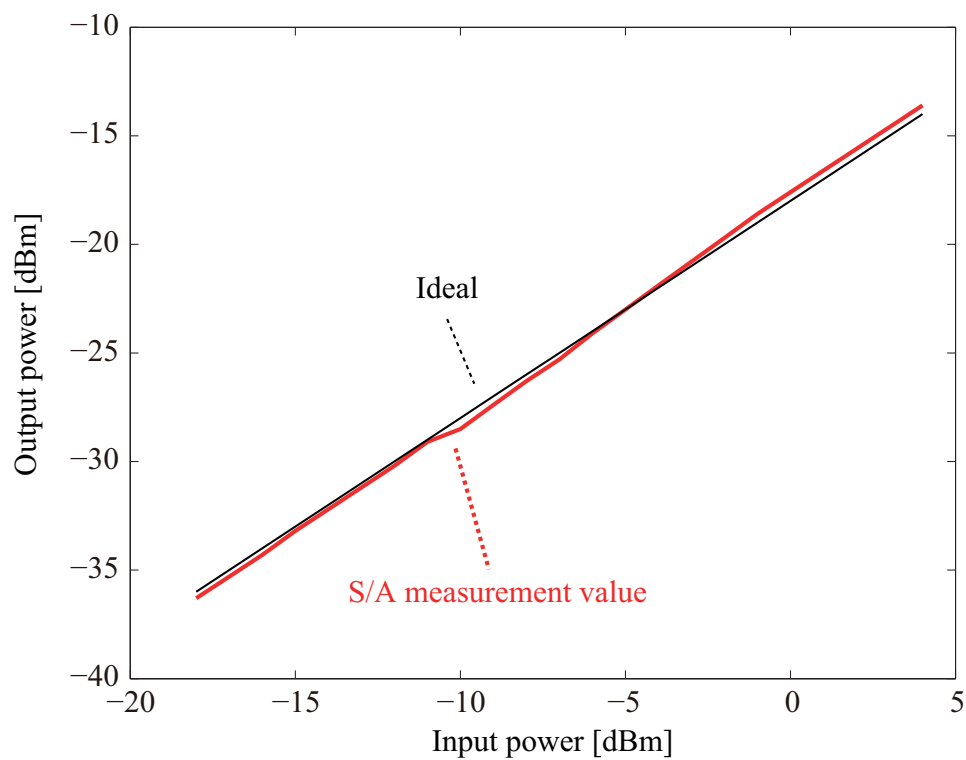
Figure 4.20   Difference between real power and measured power.

4.5.2 Coverage estimation

In this section, the coverage of each scheme is estimated assuming free space condition. The received power distribution can be calculated by substituting the experimental parameters shown in Table 4.2 and Fig. 4.14 into Eqs. (3.12)-(3.20) in the case of free space condition ($I = 1$). Then, the theoretical values of the coverage for SP, MP and MPCSD can be calculated by substituting the received power distribution into Eqs. (4.3) and (4.5) as

$$C^{\text{SP}} = 55.5\%, \quad C^{\text{MP}} = 90.9\%, \quad C^{\text{MPCSD}} = 100\%,$$

respectively. The estimated results show that the coverage of MPCSD achieves 100% which is about twice that of SP, while MP cannot achieve the full coverage due to the destructive interference.

4.5.3 Experimental Results

Figures 4.21-4.24 show the experimental results of power distribution and sensor activation. The symbols 'O' and 'X' correspond to the active and inactive status of the battery-less sensor node respectively. In the case of SP, when the sensor node is far from the corresponding Tx antenna, the received power attenuates and the number of active sensor nodes decreases in proportion to the distance between Tx and sensors as shown in Figs. 4.21 and 4.22. In these figures, the received power is fluctuated by multi-path such that some sensor nodes, which are close to Tx i.e. around 2.3 m in Fig. 4.21, cannot be activated due to destructive standing-wave, while some sensors, which are far from Tx i.e. around 4.5 m in Fig. 4.21, can still be activated owing to constructive standing-wave. In the case of MP, several deadspots exist due to destructive interference between multiple wave sources, especially at the central area between the two Txs as shown in Fig. 4.23. On the contrary, in MPCSD, the degraded received power at deadspots are remarkably improved and the sensor node can be activated at all locations as shown in Fig. 4.24.

The activation threshold is about -4 dBm which is as expected from P_{req}. However, there are discrepancy points where the sensor node can be activated by a received power even below -4 dBm, or where the sensor node cannot be activated by a received power even above -4 dBm. This is because the finite measurement time could result in a discrepancy of the activation status because, when the received power is almost the same as the required power, the voltage difference at the capacitor would fluctuate between plus and minus. The coverage of SP from Tx♯1 and Tx♯2 are, respectively, limited by 84.4% and 85.2%. In the case of MP, the coverage is still limited by 83.7%. On the other hand, the coverage of MPCSD can achieve a full coverage to activate the battery-less sensor node.

Table 4.3　Measured and estimated coverage.

	SP : Tx1	SP : Tx2	MP	MPCSD
Measured	84.4%	85.2%	83.7%	100%
Estimated	58.3%	58.3%	86.4%	100%

Here, because the measurement cannot be performed in the range of 0 m to 6 m due to the absolute maximum rating of RF/DC conversion circuit, the theoretical coverage calculated in the previous section is recalculated for the reduced range of 1 m to 5 m. The measured results and estimated results are shown in Table 4.3. In SP, the measured coverage is higher than the theoretical value because of the effect of constructive standing-wave created by multi-path. On the other hand, in MP, the measured coverage is almost the same as the theoretical value, so that the effect of multipath is not very dominant in MP as mentioned in Ch. 3. In addition, the measured coverage of MPCSD achieves 100% as expected.

Figure 4.25 shows the coverage against varying P_{req}. The function of the coverage can be calculated by Eq. (3.21). As shown in Fig. 4.25, at the required power $P_{\mathrm{req}} \approx -4$ dBm, the values of coverage are almost similar to the results of the activation. From this figure, MP can only realize 100% coverage with sensor node which consumes less than -20 dBm. In comparison to the estimated results, the system performance of SP and MPCSD decrease due to the multipath, while that of MP is almost the same because the destructive interference is dominant in MP. However, the amount of decreasing in MPCSD is less than that in SP because MPCSD can reduce the multipath effect.
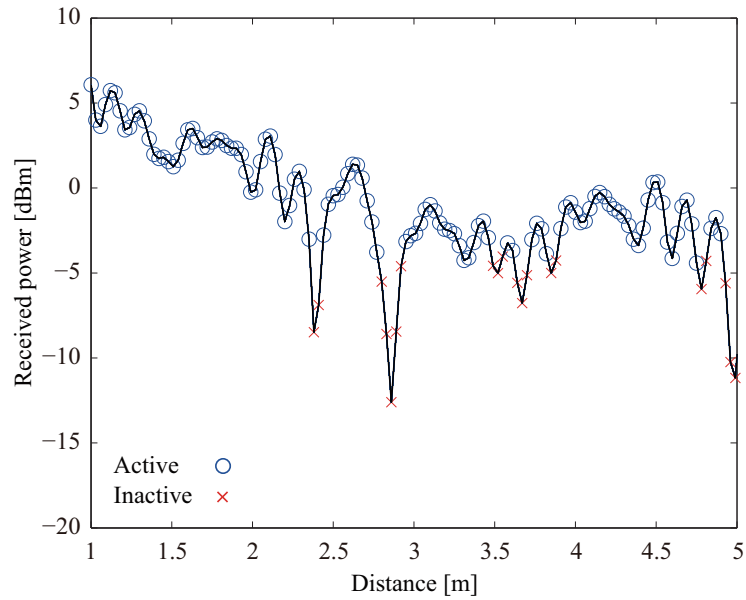
Figure 4.21 Experimental result of single-point wireless energy transmission (Tx♯1).
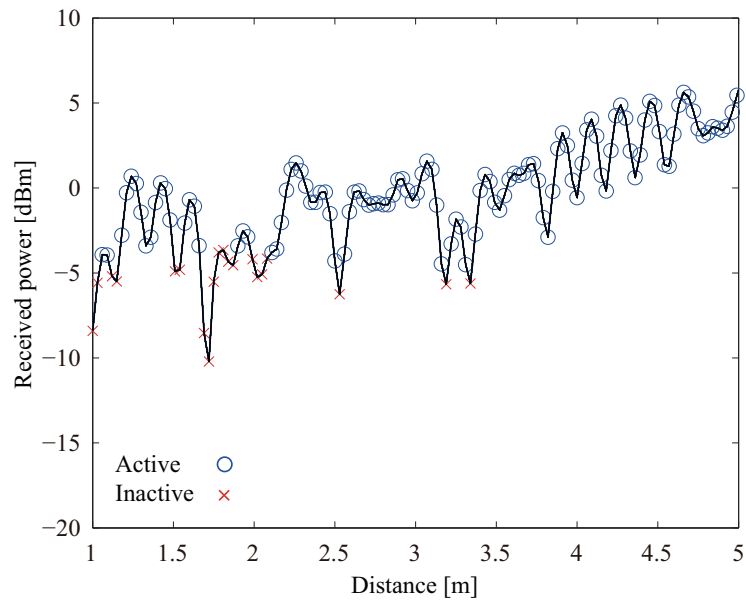
Figure 4.22 Experimental result of single-point wireless energy transmission (Tx♯2).
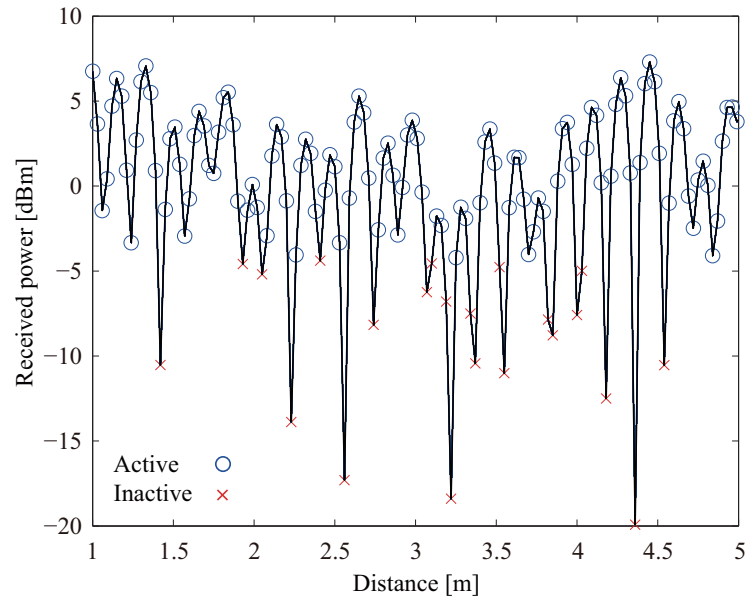
Figure 4.23   Experimental result of multi-point wireless energy transmission without carrier shift diversity.
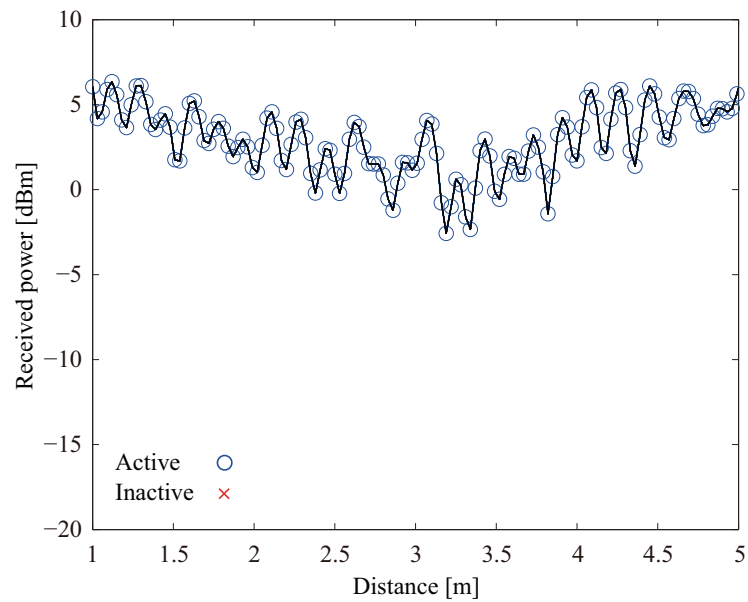
Figure 4.24   Experimental result of multi-point wireless energy transmission with carrier shift diversity.
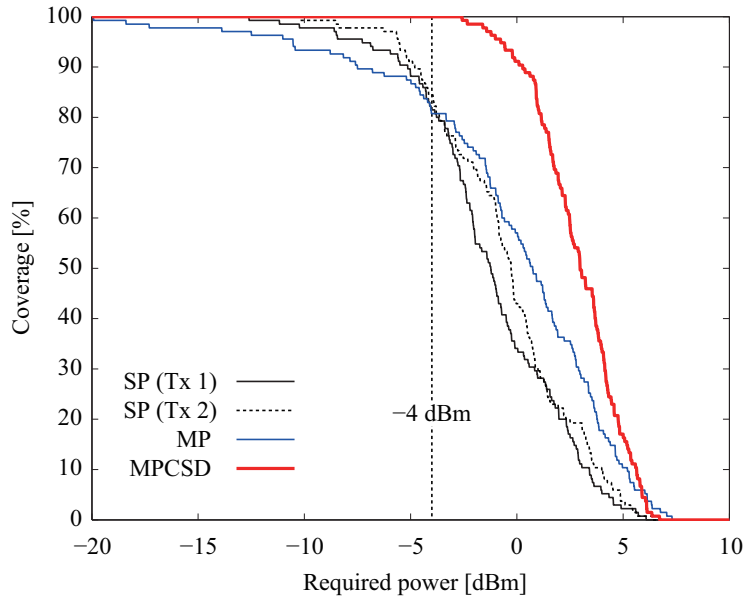
Figure 4.25 Coverage comparison of three energy transmission schemes.

4.6 Summary

This chapter provided theoretical analysis on the activation coverage of battery-less sensor nodes, developed real battery-less sensor nodes composed of off-the-shelf devices, performed measurements of consumed power of the developed sensor node and conversion efficiency of RF/DC conversion circuit, and conducted indoor experiments using the developed battery-less sensor. The developed sensor node with the duty cycle of 1 s consumed 140 μW while 400 μW was required to activate the sensor node by taking into account the RF/DC conversion efficiency of 35%. Experimental results showed that the coverage of single-point and simple multi-point energy transmission were limited to 84.4% and 83.7% respectively, while the proposed scheme achieved 100% coverage. Experiments on a real battery-less sensor node verified that the improvement of the activation coverage can be realized by the multi-point wireless energy transmission with carrier shift diversity.

Chapter 5

Implementation of wireless grid
in a real indoor environment

5.1   Introduction

Based on the fundamental works of Ch. 3 and 4, this chapter implements wireless grid into a real indoor environment. The application of wireless grid is to perform LED light control for reducing the consumed energy of the building. Different from the experiments conducted by Chs. 3 and 4, the Tx antennas are located on the ceiling and embedded in ceiling light to easily introduce the wireless energy transmission system in indoor environments. In addition, the Tx antenna directivity and polarization are designed to perform 2-D wireless energy supply extended from 1-D energy supply of Ch. 3 and 4. Furthermore, a light MAC and NW (NetWork) layer for data communication are introduced for the low-energy sensor node redesigned in this chapter by extending from prototype hardware of the sensor node in Ch. 4. To evaluate the developed system, we conduct indoor experiments to verify the design of 2-D wireless energy transmission. The experimental results show that MPCSD achieves 100% coverage of the activation in the office environment. In this thesis, details of the LED control system, which had been done in [77], are out of scope.

5.2   System architecture

The system architecture of the implemented LED control system using wireless grid as shown in Fig. 5.1 can be mainly divided into three parts, i.e. wireless energy transmitter embedded in LED ceiling light, low-energy battery-less sensor node, and communication network and control system.
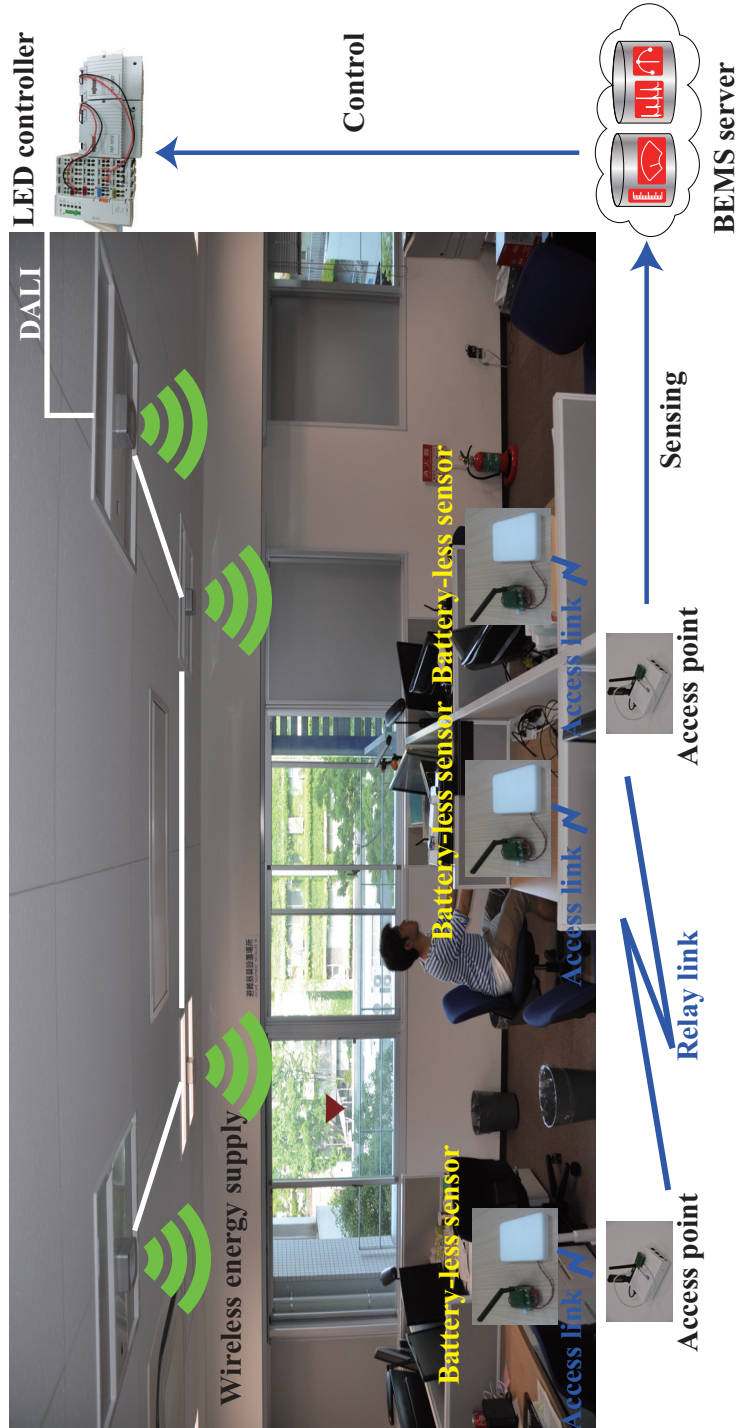
Figure 5.1 LED control system
activated by multi-point wireless energy transmission.

Multiple wireless energy transmitters embedded in the ceiling lights emit microwave to supply energy to battery-less sensor nodes. Each transmitter is connected to BEMS server, which controls the carrier frequency for CSD, via wired LAN (Local Area Network). Battery-less sensor nodes are activated by this wireless energy, sense human detection and transmit their sensing data to Access Point (AP) via wireless link. APs transfer the collected sensing data to the BEMS server through the APs via multi-hop transmission. BEMS server generates control command based on the sensing data and transmit them to the LED controller. Finally, the LED controller connected to all LED ceiling lights performs ON/OFF or dimmer control by using Digital Addressable Lighting Interface (DALI) protocol [78] [79].

The following two sections present wireless energy transmission coverage to guarantee the sensor activation and architecture of data communication.

5.2.1 2D wireless energy transmission

In order to introduce MPCSD into real indoor environments and guarantee the sensor activation anywhere, the received power distribution $P_{\mathrm{r}}(x, y, z)$ in the target space can be designed and should be larger than the required power. The received power can be generally expressed as

$$P_{\mathrm{r}}(x, y, z) = \sum_{n=1}^{N} P_{\mathrm{t},n} G_{\mathrm{t},n}(x, y, z) h_n(x, y, z) \eta_n(x, y, z) G_{\mathrm{r},n}(x, y, z), \tag{5.1}$$

where N is the number of transmitters, $P_{\mathrm{t},n}$ is transmit power of n-th Tx, $G_{\mathrm{t},n}(x, y, z)$ and $G_{\mathrm{r},n}(x, y, z)$ are Tx and Rx antenna gains from n-th transmitter to sensor node located in (x, y, z) respectively, $h_n(x, y, z)$ is the propagation channel including multipath and shadowing effects from n-th transmitter to the sensor node, and $\eta_{\mathrm{n}}(x, y, z)$ is polarization mismatch loss. To realize seamless energy supply and improve the uniformity, the minimum received power in (x, y, z) should be maximized under the radio regulation. Here, it is assumed that the Tx power of all transmitters are the same as P_{t} and the Tx antenna directivity of all transmitters are the same as $G_{\mathrm{t}}(\theta_n, \phi_n)$, where θ_n and ϕ_n $((0 \leq \theta_n \leq \pi, \ 0 \leq \phi_n \leq 2\pi))$ are the standard spherical coordinate angles. The relationship between two coordinate systems is shown in Fig. 5.2 and the equations exchanging two coordinate systems

are shown as follows.

$$G_t(\theta_n, \phi_n) = G_{t,n}(x, y, z) \tag{5.2}$$

$$r_n = \sqrt{(x - X_n)^2 + (y - Y_n)^2 + (z - Z_n)^2}, \tag{5.3}$$

$$\cos\theta_n = \frac{z - Z_n}{\sqrt{(x - X_n)^2 + (y - Y_n)^2 + (z - Z_n)^2}} \tag{5.4}$$

$$\cos\phi_n = \frac{x - X_n}{\sqrt{(x - X_n)^2 + (x - Y_n)^2}}, \quad \sin\phi_n = \frac{y - Y_n}{\sqrt{(x - X_n)^2 + (x - Y_n)^2}} \tag{5.5}$$

where (X_n, Y_n, Z_n) is the transmit point of n-th transmitter. In the parameters in Eq. (5.1), one of the designed parameters is Tx antenna directivity. Therefore, under the EIRP regulation P_{EIRP}, the Tx antenna directivity can be designed as

$$G_t(\theta, \phi) = \arg\max_{G_t} \min_{x,y,z} (P_r(x, y, z))$$
$$\text{s.t. } \max G_t P_t \leq P_{\text{EIRP}}. \tag{5.6}$$

In real situation, as the energy transmitters are often deployed in a grid shape, employing 4 transmitters is minimum configuration by considering the scalability. Figure 5.3 shows the 4 transmitter configuration. In the figure, Tx♯1-♯4 are deployed on the height of $Z = 0$ and formed as $X \times Y$ grid ($X \leq Y$), while sensor nodes are deployed at the height of Z. In addition, it is assumed that Rx antenna directivity is omni-directional $G_{r,n}(x, y, z) = 1$ and the polarization loss is ignored $\eta_n(x, y, z) = 1$. The received power of the sensor node located (x, y, Z) in free space condition can be described as

$$P_r(x, y, Z) = P_t \left(\frac{\lambda}{4\pi}\right)^2 \sum_{n=1}^{4} \frac{G_t(\theta_n, \phi_n)}{r_n^2} \tag{5.7}$$

As mentioned in Ch. 3, although different frequencies are used in all the transmitters, its difference Δf is very small compared with the carrier frequency f_c, such as $\Delta f = 1$ kHz and $f_0 = 916.8$ MHz. Thus, the difference on the wavelength is also negligible, and we denote it with a single parameter λ. Here, the antenna directivity is assumed to be ideal plane antenna, the minimum received power must be

$$\min_{x,y} P_r = \min (P_r(0, 0, Z), P_r(0, X, Z)). \tag{5.8}$$

In other word, the candidate of locations where minimum power can be received is the location at in between 4 transmitters ($\mathbf{L_a}$) or in between 2 transmitters ($\mathbf{L_b}$).

To activate sensor nodes, the point with minimum power must be larger than the required power. Therefore, the following inequality should hold.

$$\min\left(P_r(0, 0, Z), P_r(0, X, Z)\right) \geq P_{req}. \tag{5.9}$$

It is noted that the minimum received power should be estimated by considering the multipath, shadowing and polarization as mentioned in Eq. (5.1). In other words, the link margin should be designed. In this thesis, however, the minimum received power is estimated in free space condition for the sake of simplicity.
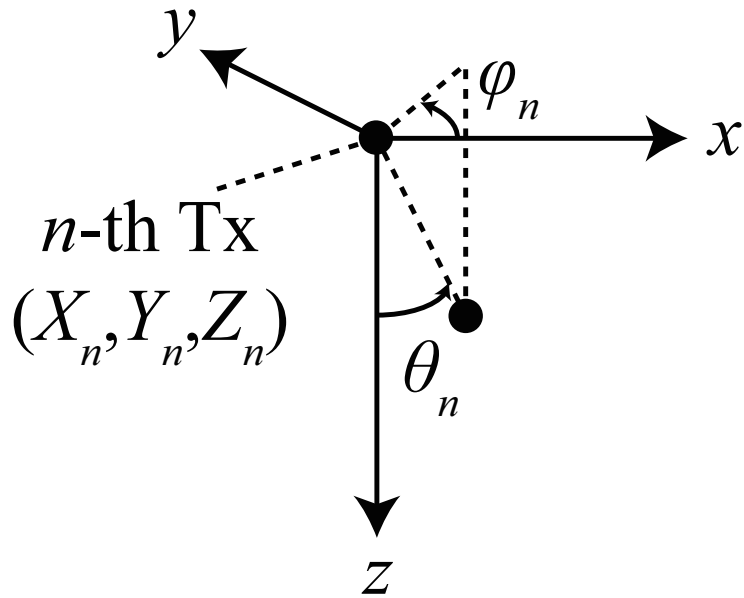
Figure 5.2 Relationship between Cartesian and Spherical coordinate systems.
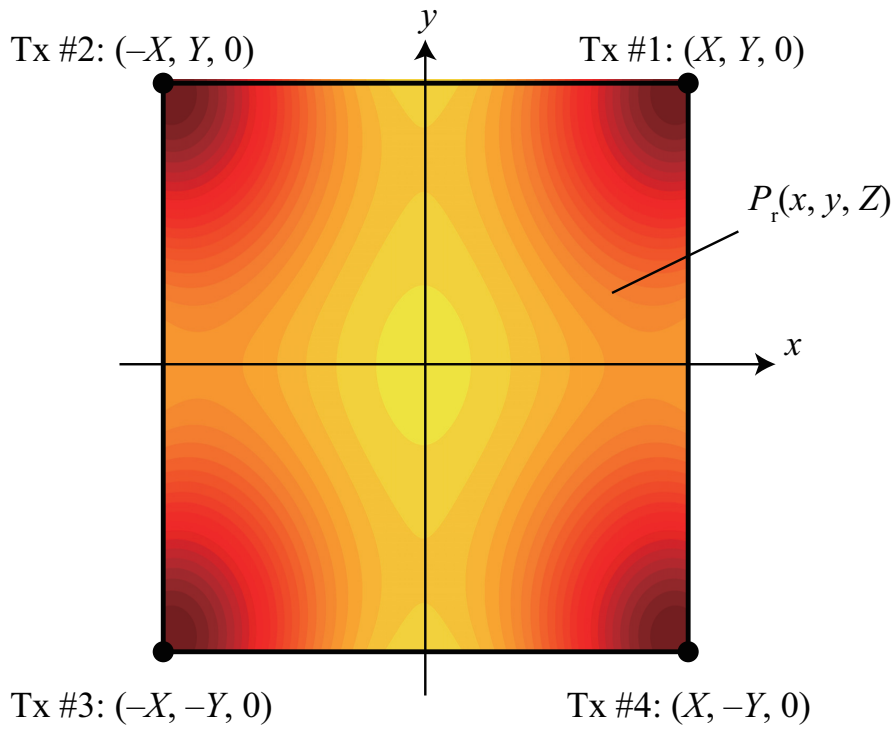
Figure 5.3 Four transmitter configuration.

5.2.2   Data communication for sensor networks

In the development of the sensor node of Ch. 4, in order to reduce the consumed power, intermittent operation, low Tx power transmission and broadcast transmission were employed. In this chapter, the following network architecture is assumed in the data communication to compensate the limited range due to low power transmission. To guarantee the coverage of data transmission, the Tx power of data transmission must be as high as possible. However, increasing the Tx power results in increasing the consumed power of the sensor node as shown in Figs. 4.11 and 4.12. A solution to save power as while maintaining coverage is to introduce multi-hop transmission, which has been used widely in WSNs. IEEE 802.15.4 [20] and 15.4g [21], which are generally employed for WSNs, has a dedicated multi-hop protocol among nodes in the network. However, since the MCU must manage routing and be always active, employing the multi-hop protocol for the sensor node results in increasing the consumed power of the sensor node. Therefore, in this implementation, only APs, which are supplied by electrical plug, employ this protocol to create a hierarchical backhaul network as shown in Fig. 5.4.

In addition, sensor nodes must perform the carrier sense before their transmission in the access link between sensor nodes and APs. However, the consumed power also increases if the channel is busy and sensor nodes need to wait until the channel is available. For the reason, when the channel is busy, sensor nodes transit to sleep mode without data transmission until the next duty cycle. Furthermore, sensor nodes broadcast their sensing data periodically in an opportunistic manner due to a very light network structure between sensor nodes to save power. Therefore, the sensing data can be received by some APs. However, it results in the data redundancy in the backhaul network. To deal with the redundancy, one predefined AP accepts the data while the others discard them. The predefined AP for each sensor node is configured at the initial installation stage of the network by clustering based on Received Signal Strength Indicator (RSSI) from sensor nodes observed by APs as shown in Fig. 5.5. While active MCUs which consume tens of mW, the low energy sensor node consumes only hundreds of μW as shown in the measurements of the previous chapter by employing the proposed architecture which can realize coverage extension of wireless energy transmission.
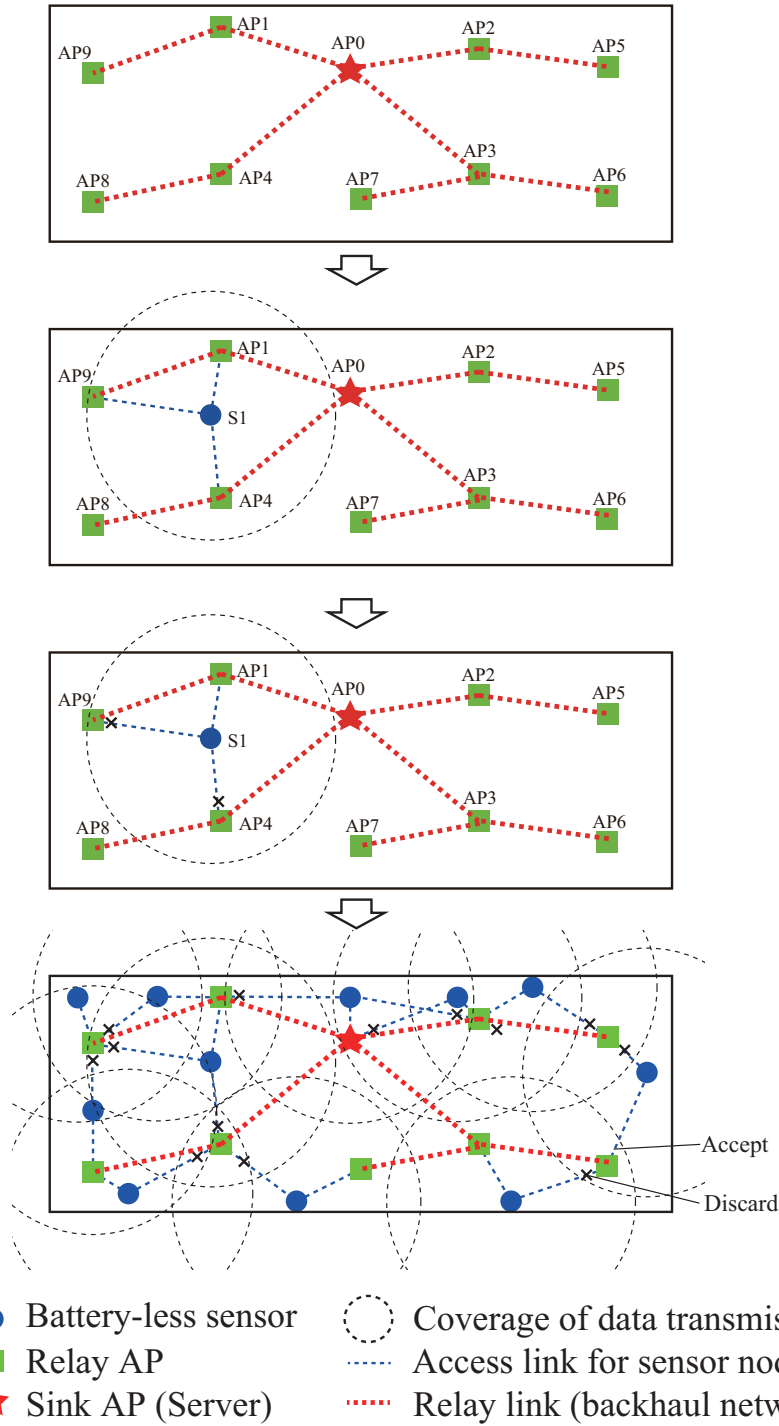
Figure 5.4 Network architecture of sensor network for data communication.

Sink node   Relay node

(Begin)   (Begin)

                                                    Decision of routing
                                                    to sink node

                                                    Rx sensing data
                                                    from all of sensor nodes

Rx RSSI of each sensor node   ····· Relay link ·······   Tx RSSI of each sensor node
from all of relay nodes   to sink node

Calculate association group

Tx association information   ······ Relay link ····▸   Rx association information

                                                    Rx sensing data

                                                    Sensing data
                                                    from associated sensor node?   no

                                                              yes

Rx sensing data   ◂······ Relay link ·············   Tx sensing data
without redundancy

              Refresh time?   Refresh time?   no
    no

                    yes   yes

Figure 5.5   Flow chart of network architecture for data communication.

5.3   Development of system components

To introduce wireless grid into real indoor environments according to the system architecture, this section provides key components of the development, i.e. wireless energy transmitter embedded in LED ceiling light performing wireless energy supply, low energy battery-less senor node activated by wireless energy transmission, and wireless multi-hop transmission for sensor network taking a role of gathering sensing data.

5.3.1   Wireless energy transmitter embedded in LED ceiling light

Table 5.1 and Fig. 5.6 show the components of wireless energy transmitter. To easily introduce wireless energy transmission system, the energy transmitter is embedded in LED ceiling light. The transmitter mainly consists of a Tx antenna [80], an RF synthesizer [81], a power amplifier [82], and a CPU board [83]. The RF synthesizer controlled by the CPU board which is connected to BEMS controller creates the RF signal with frequency shift required for carrier shift diversity. The signal is amplified 27 dB by the power amplifier. Finally, the signal of 30 dBm, which is limited by radio regulation of 920 MHz band in Japan, is transferred from Tx antenna. In this configuration, the total consumed power of wireless energy transmitter becomes several Watts, while the reduction of the consumed power by LED control system per light can be expected to be several tens of Watts.

In the employed Tx antenna, it is satisfied that the received power at the minimum point calculated in free space condition in the room is larger than the required power of the activation. In other words, Eq. (5.9) is satisfied in the area of $X = 0.955$ m $\times$ $Y = 1.065$ m on the height of sensor deployment from transmitters $Z = 2.56 - 0.72 = 1.84$ m. In addition, both the energy transmitter and the rectenna employ circular polarized antennas to install the sensor node without considering its orientation. Furthermore, to stably activate the sensor node, the cycle of the artificial fading created by multiple transmitters with CSD should be less than the duty cycle of the intermittent operation. In the developed system, the carriers of transmitters are 916.8 MHz±1 kHz, 916.8 MHz±2 kHz ... , to set the cycle to 1 ms.

5.3.2   Low energy battery-less sensor node

Table 5.2 and Fig. 5.7 show the components of the battery-less sensor node. The battery-less sensor node consists of a rectenna [62] including a power receiving antenna, an RF/DC conversion circuit, a capacitor taking a role of rechargeable battery, a DC/DC conversion circuit and voltage regulator,

an IR human detection [84], luminance and temperature sensor, and an RF module including a MCU [29] and an RFIC [36]. It is noted that the sensor node including an IR human detection sensor and RF module is the same configuration as the developed sensor node in Ch. 4. The RF energy, received by rectenna, is converted to DC by the RF/DC conversion circuit, the output of DC voltage is boosted to 4 V by the DC/DC converter and the output of the DC/DC converter is stored in capacitor. In the voltage regulator, the output voltage is converted to 2.3 V when the capacitor voltage rises more than 3 V, while the output of the regulator is switched to OFF state when the capacitor voltage falls less than 2.3 V as shown in Fig. 5.8. In other words, the voltage difference between 3 V and 2.3 V can be stored in the capacitor by the voltage regulator. In this development, the power receiving antenna is dominant for the whole size of rectenna as shown in Fig. 5.7.

The required capacitance is calculated as about 74 μF by substituting parameters measured in Ch. 4 (T_{Tx} = 10 ms, P_{Tx} = 13.8 mW, P_{csp} = 142 μW) and the voltages defined by the regulator ($V_c(T_s)$ =3 V, $V_c(T_d)$ =2 V) into Eq. (4.9). However, because the consumed energy in the initial activation is much more than the consumed energy of Tx mode, 2.5 mF capacitor is equipped in the sensor node.

Table 5.1 Components of wireless energy transmitter.

Tx antenna	RF-ATCP013 (Mitsubishi Electric)
Synthesizer	LMX2531 (Texas Instruments)
Power amplifier	RF3858 (RFMD)
CPU board	OpenBlocks A7 (Plathome)

Outside

Inside
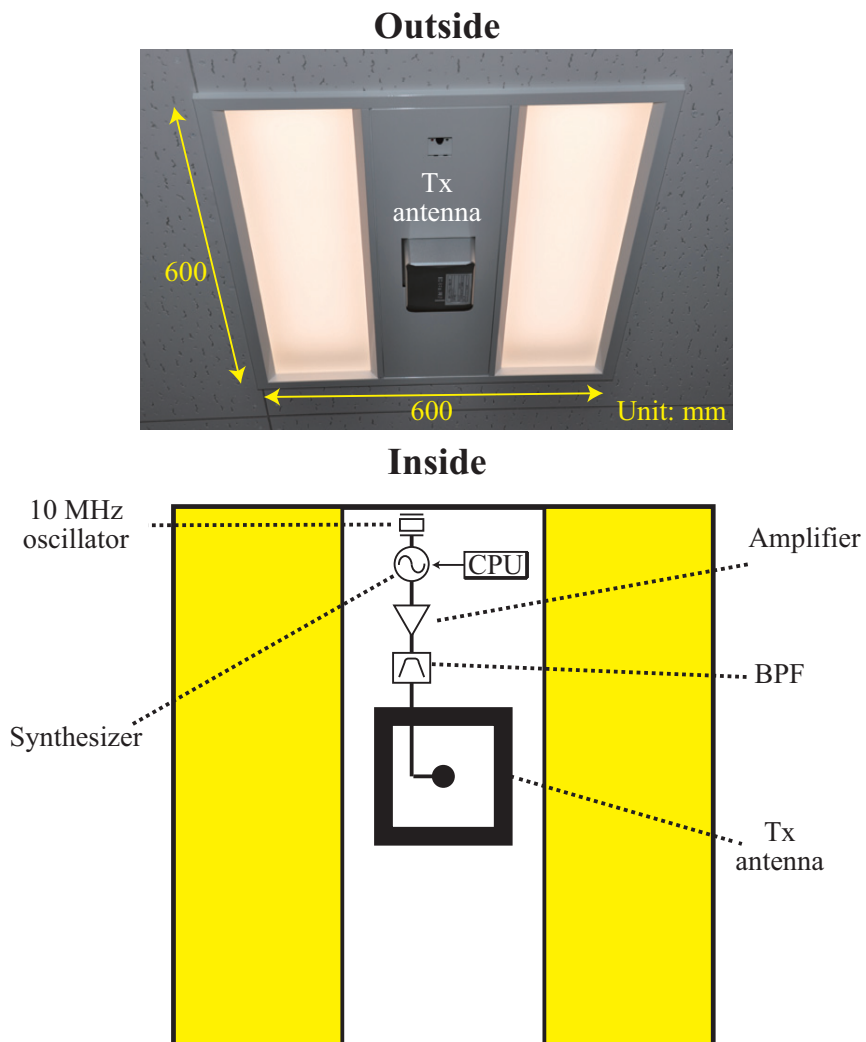
Figure 5.6 Structure of wireless energy transmitter.

Table 5.2   Components of battery-less sensor node.

Rectenna	Custom made (Nihon Dengyo Kosaku)
RF module	Custom made (Tessera Technology)
RF device	ADF7023-J (Analog Devices)
MCU	R5F100GJ (Renesas Electronics)
Human detection sensor	EKMB1101111 (Panasonic)
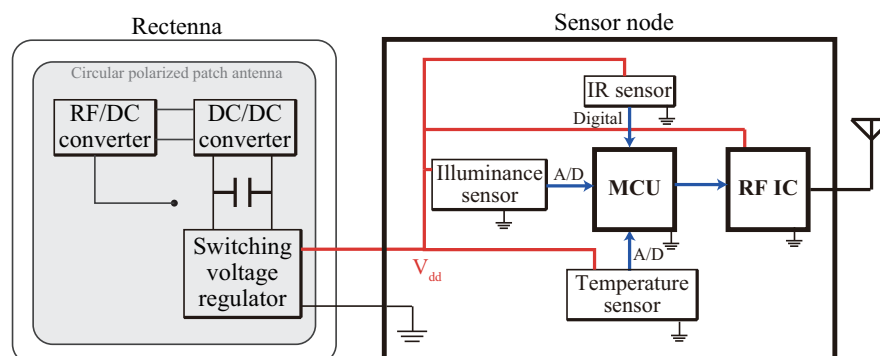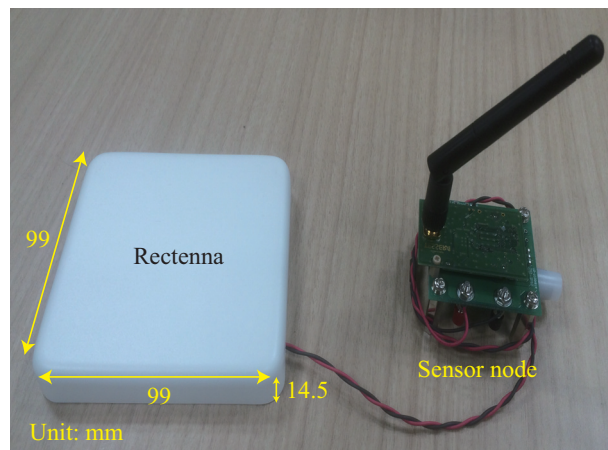
Figure 5.7   Structure of battery-less sensor node.

Voltage

DC/DC output

ON voltage of regulator

OFF voltage of regulator

Regulator output

T_d

Time

0

(a) Active sensor node

Voltage

DC/DC output

ON voltage of regulator

OFF voltage of regulator

T_d

Time

0

(b) Inactive sensor node
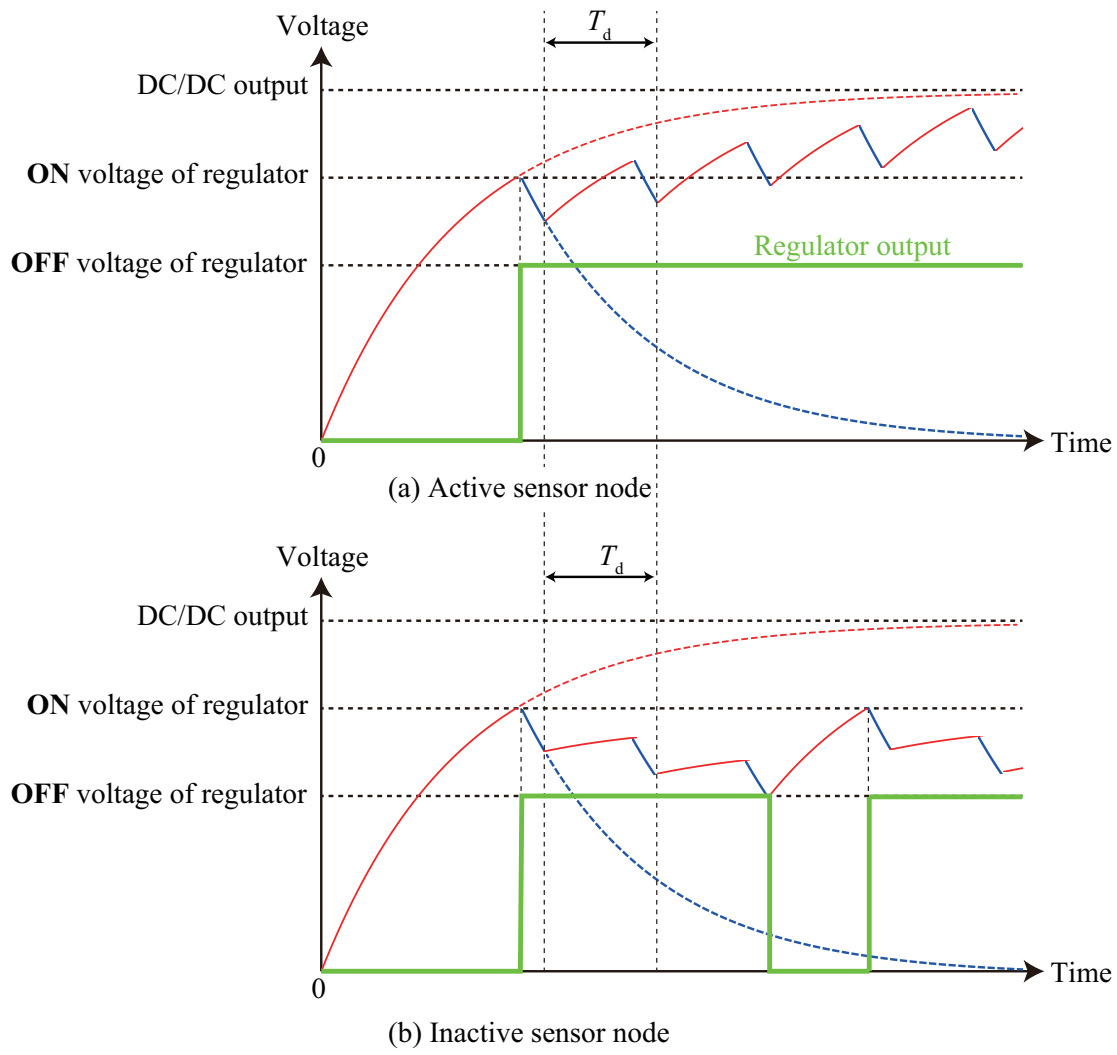
Figure 5.8 Relationship between rectenna output and capacitor voltage.

Table 5.3 Calculation of minimum received power in free space.

Parameter	$\mathbf{L_a}$	$\mathbf{L_b}$
Tx power	30 dBm	
Tx antenna gain	0 dB	1 dB
Path-loss	39 dB	38 dB
Multi-point gain	6 dB	3 dB
Rx antenna gain	1 dB	2 dB
Received power	−2 dBm	
Required power	−4 dBm	

5.3.3   Estimation of minimum received power

Here, the received power at $\mathbf{L_a}$ and $\mathbf{L_b}$ in free space can be calculated by substituting the parameters of the grid density, the configuration of transmitter and the consumed power of sensor node into Eqs. (5.2)-(5.8). Table 5.3 shows calculated parameters of the developed system at $\mathbf{L_a}$ and $\mathbf{L_b}$. Both Tx and Rx antenna gains of $\mathbf{L_a}$ are smaller than those of $\mathbf{L_b}$ because the seen angle from Txs to $\mathbf{L_a}$ (38 degrees) is wider than that of $\mathbf{L_b}$ (29 degrees). Path-loss of $\mathbf{L_a}$ is larger than that of $\mathbf{L_b}$ because the distance from Txs to $\mathbf{L_a}$ (2.1 m) are slightly larger than that of $\mathbf{L_b}$ (2.3 m). In addition, multi-point gain of $\mathbf{L_a}$ is higher than that of $\mathbf{L_b}$, because the number of nearest Txs at $\mathbf{L_a}$ (4) is larger than that at $\mathbf{L_b}$ (2). It is noted that the multi-point gain denotes the number of summation of received power from nearest transmitters, so that the gain at $\mathbf{L_b}$ is ignored from the other 2 transmitters. Finally, in the developed system, the received power at $\mathbf{L_a}$ and $\mathbf{L_b}$ are almost the same as −2 dBm which is 2 dB larger than the required power of −4 dBm.

5.3.4   Wireless multi-hop communication for sensor network

Table 5.4 and Fig. 5.9 show the components of AP. To realize both receiving sensing data and performing multi-hop transmission, the developed AP employs two RF modules. One is employed for access link to gather the sensing data and the other is used for relay link between APs. The sensing data transmitted by sensor nodes are gathered by RF module for access link, then delivered to the RF module for relay link, which performs multi-hop operation by DECENTRA II protocol [85], through the CPU board and finally transferred by the BEMS controller to manage LED controlling as shown in Fig. 5.9. It is noted that the CPU board manages the sensing data to avoid the redundancy in the backhaul link. The BEMS controller creates control data based on the sensing data and sends the data to LED controller. The LED controller connected to LED lights broadcast the control data by wired DALI link.

In the data communication system, the sensor nodes activated by wireless energy transmission are placed on all desks to detect human existence and transmit the sensing data 0/1 to the AP. Finally, the sensing data are transferred to the sink node connected to the BEMS controller. The BEMS controller calculates the control data and broadcasts LED lights based on the sensing data.

Table 5.4 Components of access point.

RF module (access link)	RL7023 Stick-L (Tessera Technology)
RF module (relay link)	MB-RL7023-06/D2 (Tessera Technology)
CPU board	OpenBlocks A7 (Plathome)
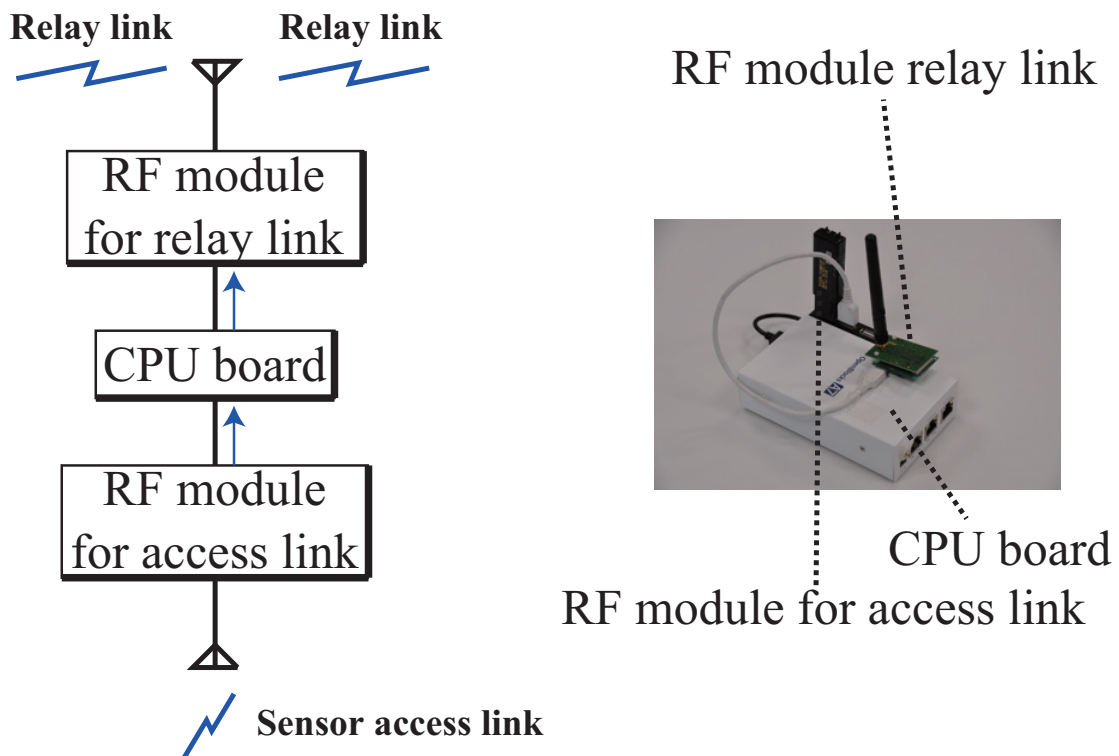
Figure 5.9 Structure of access point.

5.4　Experimental verification

In order to verify the activation possibility of the battery-less sensor node via our developed system design, we conduct indoor experiments which measure the activation status of the developed sensor nodes.

5.4.1　Experimental method

The experimental parameters and the environment are shown in Tab. 5.5, Fig. 5.10 and Fig. 5.11. At the Txs, the transmit power is set to 30 dBm and the center frequency is set to the 916.8 MHz at which transmission without carrier sensing is allowed. The carrier frequencies of the transmitters are set to ±1, 2 kHz apart from the center frequency to generate the cycle of artificial power fluctuation of 1 ms which is much faster than 1 s of the duty cycle. The transmitters are deployed on the ceiling at the height of 2.56 m from the floor, while that of the Rx antenna is 0.72 m which is the same as that of office desks. The measurement is performed in the 2-D plane among 4 transmitters. In the cases of MP and MPCSD, all the transmitters are synchronized by the 10 MHz oscillator. Figure 5.12 shows the flowchart of the experiment. To keep the fairness for all measurement points, a capacitor is charged/discharged to be 3 V before the measurement. In the experiment, the definition of the activation is judged by whether the measured voltage is increased (active) or decreased (inactive) in 5 s. Since IR sensor takes several seconds for initial activation, at the first step of the measurements, a PC with data receiver checks whether sensor is activated or not. If sensor node is not activated, the measurement is stopped in 15 s until finishing the initialization of IR sensor. After the voltage setup, RF received power is measured and the voltage of the capacitor is measured in 5 s. It is noted that the experiment flow is almost the same as the experiment while the measurement time is reduced due to a large number of measurement points and the received power is not measured because 50 Ω port is not equipped in the rectenna.
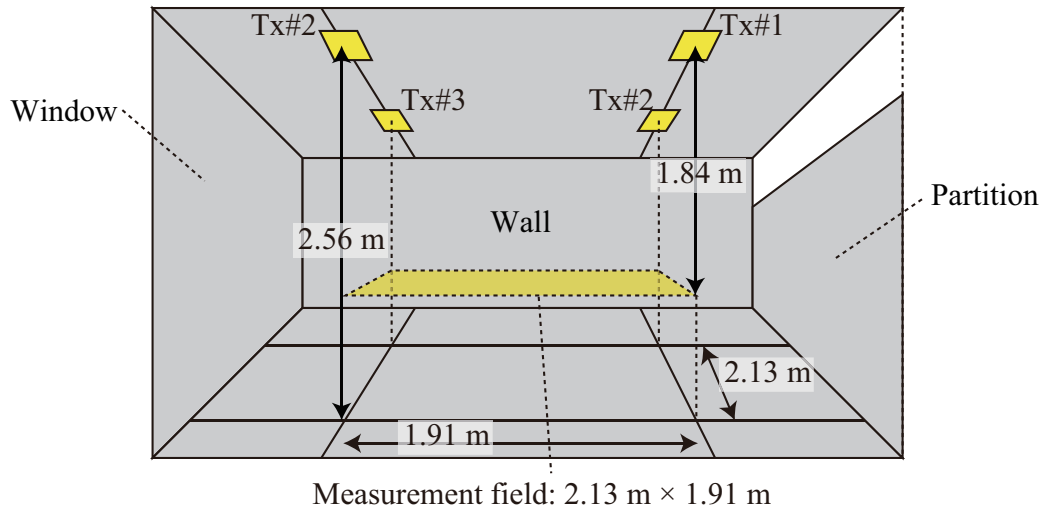
Figure 5.10 Experimental environment.
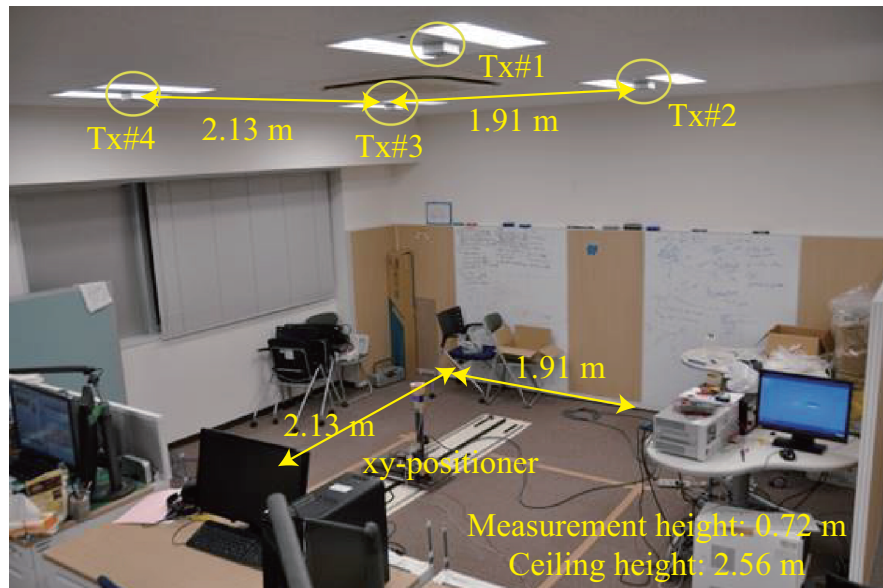
Figure 5.11 Experimental environment (Photo).

Table 5.5 Experimental parameters.

Parameter	Value
Transmit power per each antenna	30 dBm
Tx antenna gain	5.2 dBi
Center frequency	918 MHz $\pm 1, 2$ kHz
Rx antenna gain	2.9 dBi
Polarization for both Tx and Rx	Circular
Measurement point interval	3 cm$\approx \lambda/10$
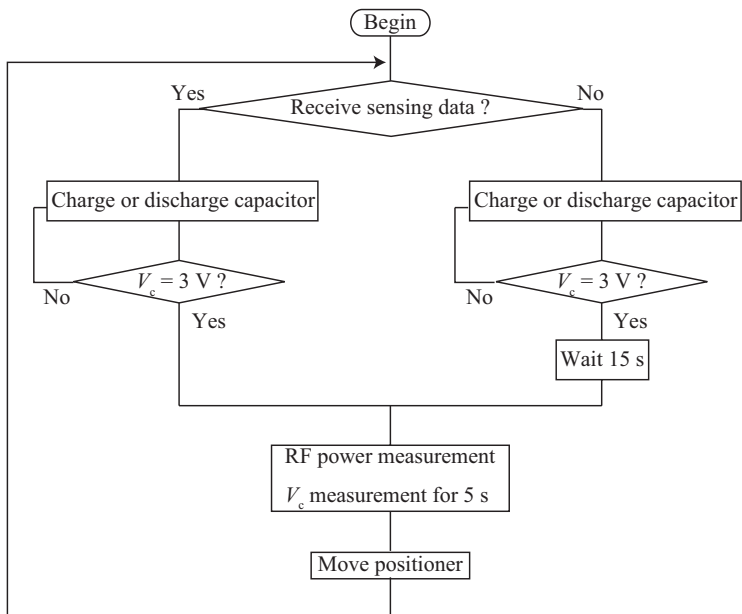
Figure 5.12 Experimental flow.

5.4.2   Experimental result

Table 5.6 and Figs 5.13-5.18 show the experimental results. In the figures, the white and black areas correspond to the active and inactive status of the battery-less sensor node respectively. In the cases of SPs, when the sensor node is far from the corresponding Tx antenna, the number of active sensor nodes decreases in proportion to the distance between Tx and sensors as shown in Figs. 5.13-5.16. In these figures, some sensor nodes far from Tx are still active and some sensors close to Tx are inactive due the constructive and destructive standing-wave created by multipath respectively. The results of the coverage in SP are 46.7%, 36.6%, 45.9% and 27.7%. The differences of the values also result from the effect of multipath because main obstacles, partition (Tx♯1-Tx♯2 side), wall (Tx♯2-Tx♯3 side), window (Tx♯3-Tx♯4 side), and desks (Tx♯4-Tx♯1 side) are different. In the case of MP, several deadspots exist due to destructive interference between multiple wave sources as shown in Fig. 5.17 and the coverage is limited by 93.6%. On the contrary, MPCSD removes the deadspots and achieves 100% coverage as shown in Fig. 5.18.

Since 50 Ω port is not equipped in the developed rectenna, RF received power cannot be directly measured. However, since time-varying voltage at capacitor is measured in 5 s, the DC received power including RF/DC conversion efficiency can be calculated by substituting experimental parameters and measured voltage into the following equation,

$$P_{\mathrm{r}}^{\mathrm{DC}} = P_{\mathrm{r}}\Gamma[P_{\mathrm{r}}] = \frac{\mathfrak{C}}{2T}(V_{\mathrm{c}}^2(T) - V_{\mathrm{c}}^2(0)) + P_{\mathrm{s}}, \tag{5.10}$$

which is extended from Eq. (4.12). Different from the configuration of the battery-less sensor node in Ch. 4, capacitor of the developed rectenna is not directly connected to the sensor node but connected through the regulator. Hence, the consumed power P_{s} might be the minimum value of the real consumed power. In other words, the calculation assumes that the efficiency of regulator is 100%.

Figure 5.19-5.24 show the distribution of the DC received power. In SP, the received power decreases in proportion to the distance from the transmitter. In addition, received power in some areas close to the Tx and far from the Tx, respectively, decreases and increases due to the multipath effect. In MP, interference fringes can be remarkably observed. On the other hand, in MPCSD, the received power in deadspots of MP is improved. It is noted that the calculated DC received power in some points is less that 0 W because of the assumption of the regulator. To convert W to dBm, therefore, the values of less than 0 W are altered to $-\infty$ dBm. Figure 5.25 shows the coverage of each transmission scheme calculated by DC received power. As seen from these results, MPCSD can seamlessly extend the coverage and improve the uniformity of power distribution. At the power

Table 5.6   Coverage of each scheme.

SP (Tx♯1)	SP (Tx♯2)	SP (Tx♯3)	SP (Tx♯4)	MP	MPCSD
46.7%	36.6%	45.9%	27.7%	93.6%	100%

consumption of the sensor node P_{csp} (-8.6 dBm), the values of the coverage are the same as those of Table 5.6. In addition, it is expected that MPCSD can achieve 100% with sensor node consuming up to about 220 μW (-6.6 dBm).

Tx#2 Tx#1

White: active, Black: inactive

1.91 m

Tx#3 Tx#4

2.13 m
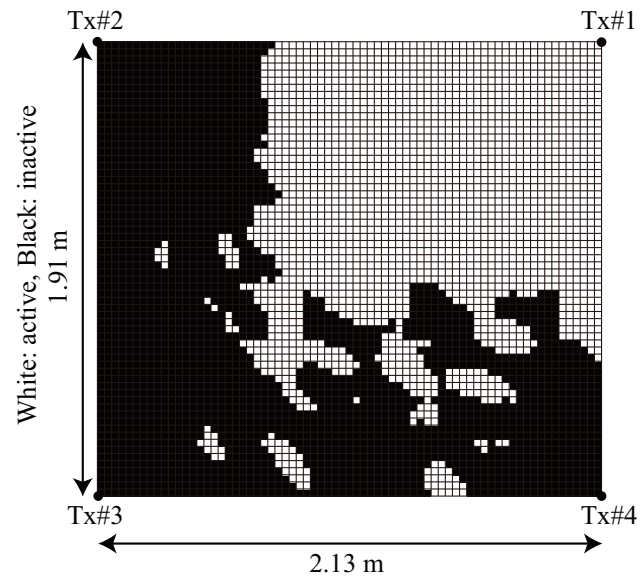
Figure 5.13   Experimental result of sensor activation
of single-point wireless energy transmission (Tx♯1).

Tx#2 Tx#1

White: active, Black: inactive

1.91 m

Tx#3 Tx#4

2.13 m
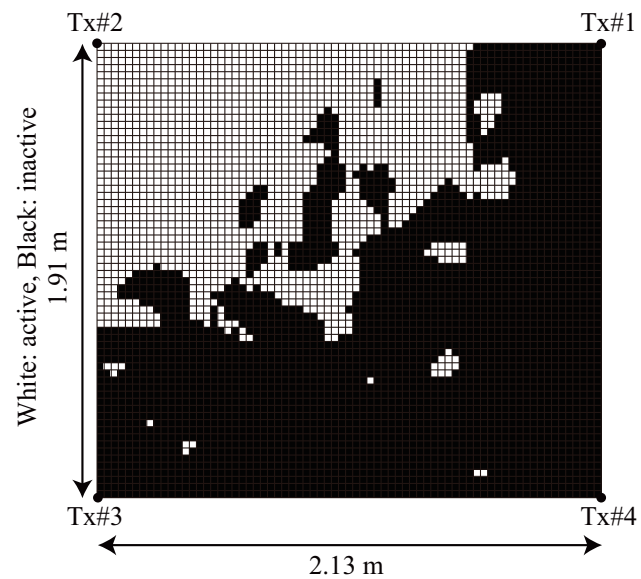
Figure 5.14   Experimental result of sensor activation
of single-point wireless energy transmission (Tx♯2).
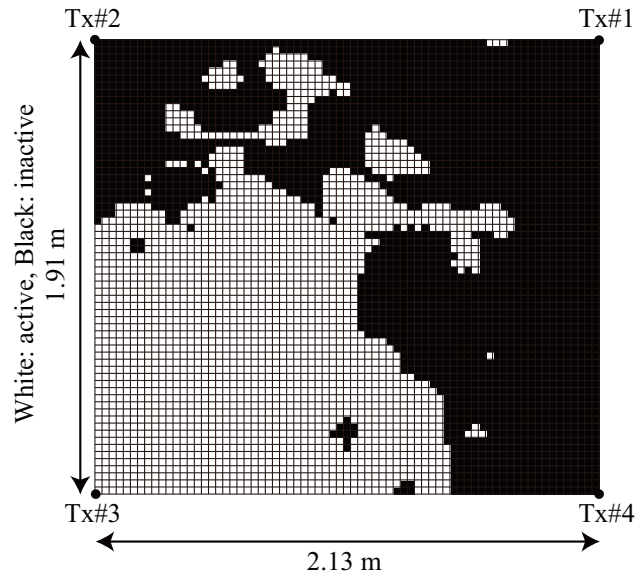
Figure 5.15   Experimental result of sensor activation
of single-point wireless energy transmission (Tx♯3).
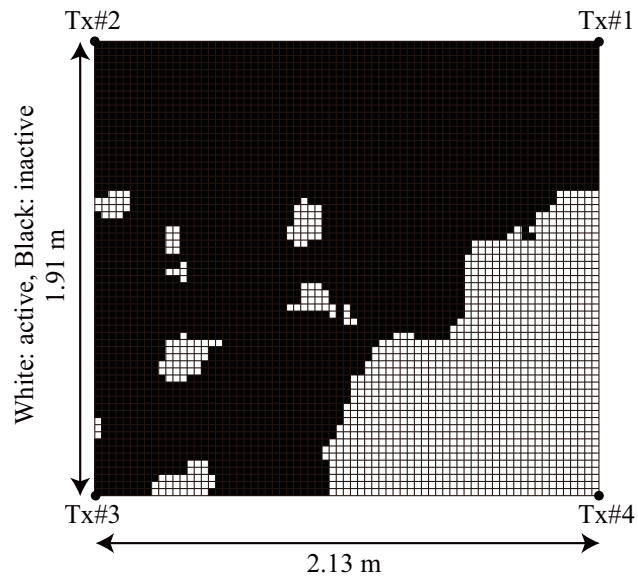
Figure 5.16   Experimental result of sensor activation
of single-point wireless energy transmission (Tx♯4).

Tx#2   Tx#1

White: active, Black: inactive
1.91 m

Tx#3   Tx#4

2.13 m
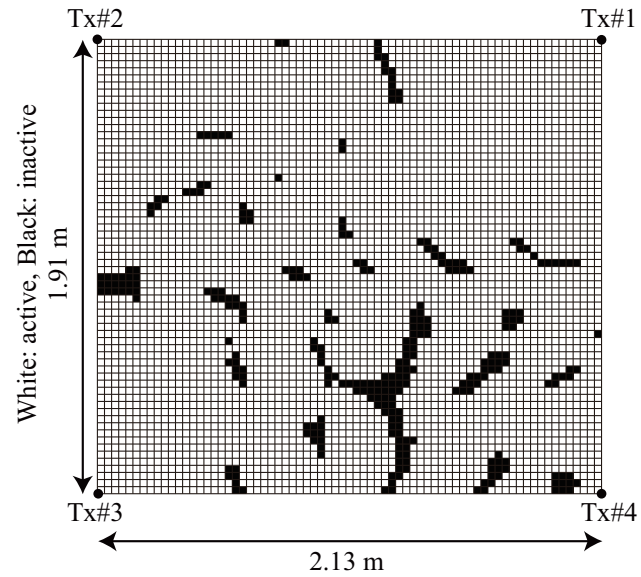
Figure 5.17   Experimental result of sensor activation
of multi-point wireless energy transmission
without carrier shift diversity.

Tx#2   Tx#1

White: active, Black: inactive
1.91 m

Tx#3   Tx#4

2.13 m
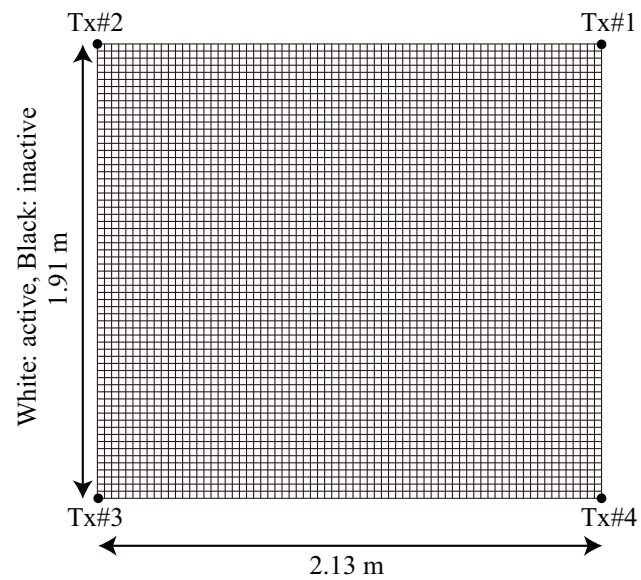
Figure 5.18   Experimental result of sensor activation
of multi-point wireless energy transmission
with carrier shift diversity.
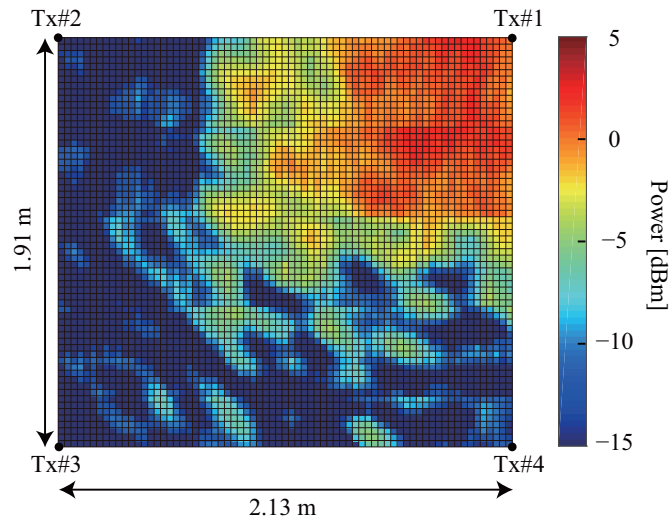
Figure 5.19   Experimental result of DC received power
of single-point wireless energy transmission (Tx♯1).
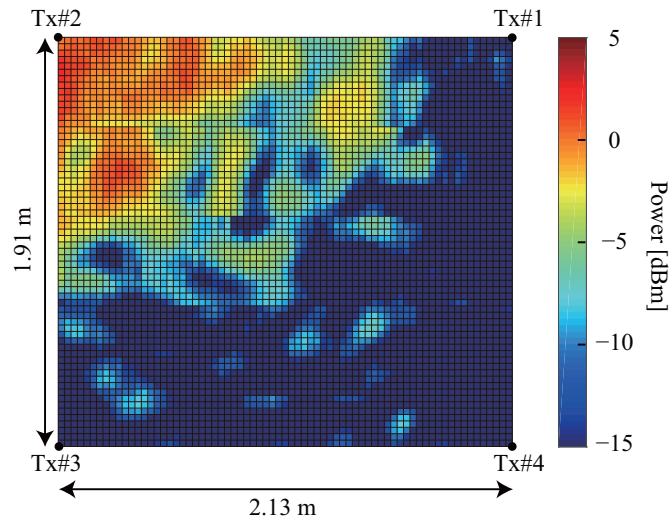
Figure 5.20   Experimental result of DC received power
of single-point wireless energy transmission (Tx♯2).
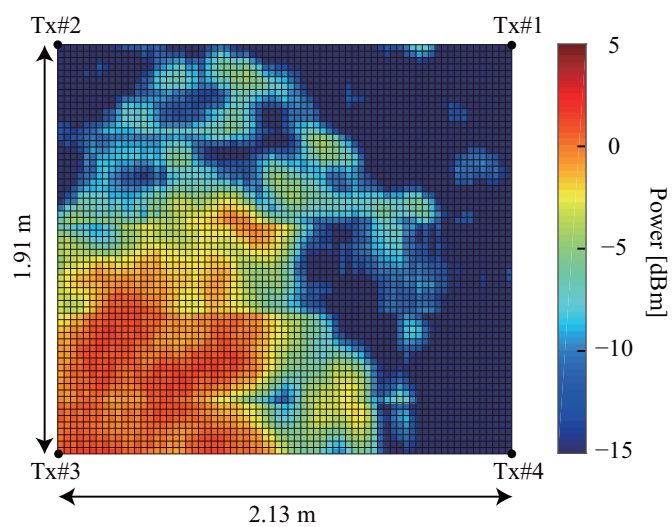
Figure 5.21 Experimental result of DC received power of single-point wireless energy transmission (Tx♯3).
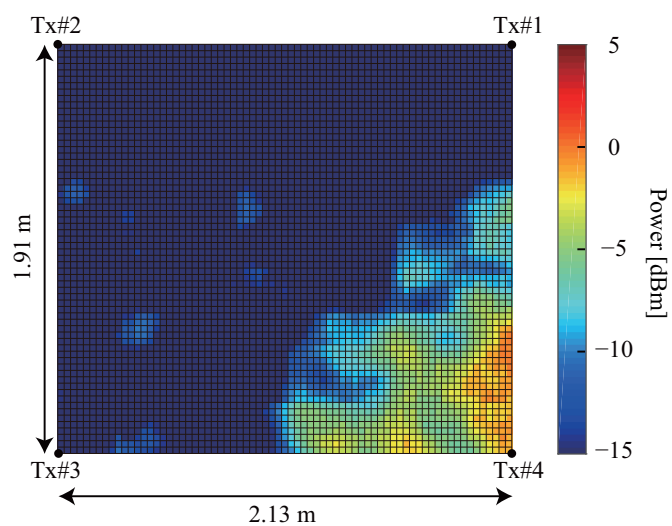
Figure 5.22 Experimental result of DC received power of single-point wireless energy transmission (Tx♯4).
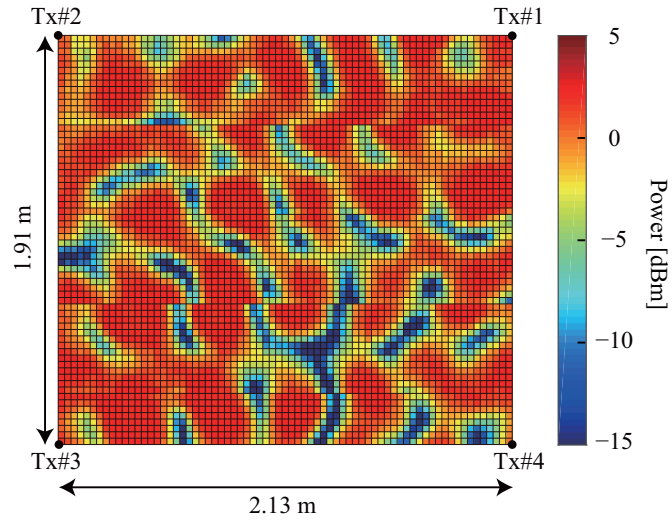
Figure 5.23 Experimental result of DC received power of multi-point wireless energy transmission without carrier shift diversity.
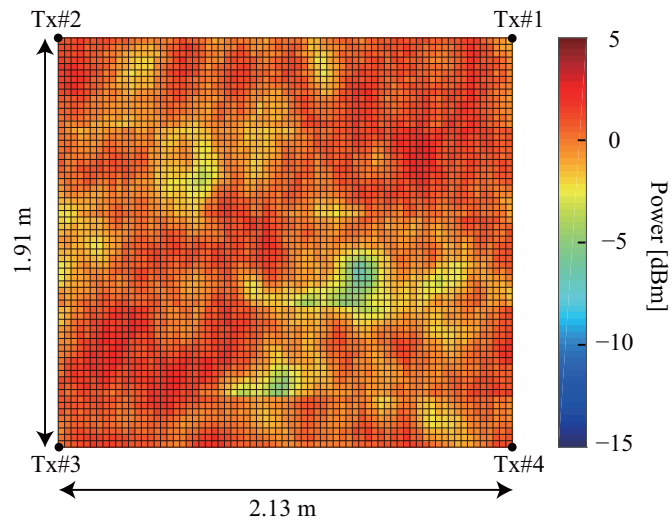
Figure 5.24 Experimental result of DC received power of multi-point wireless energy transmission with carrier shift diversity.
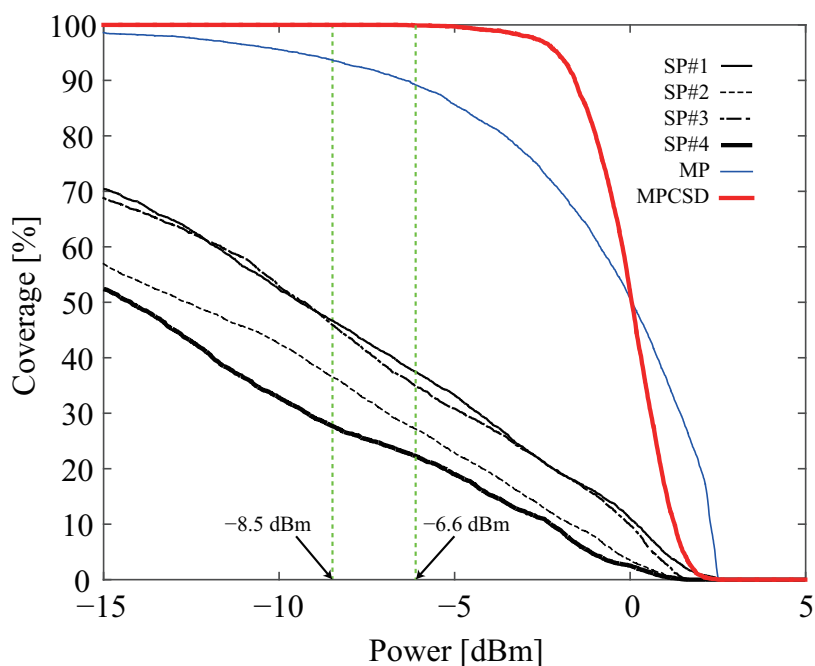
Figure 5.25   Coverage of each energy transmission scheme.

5.5   Summary

This chapter implemented wireless grid into a real office environment. The application of wireless grid performed LED light control to reduce the consumed energy of the room. To easily introduce wireless energy transmission system in real indoor environments, wireless energy transmitters were embedded in LED ceiling light. In addition, to supply wireless power to 2-D space, the antenna directivity and polarization were designed. To perform the data communication for low-energy sensor nodes, the sensor network was constructed with access links and a backhaul multi-hop network, where the access link employed very light MAC & NW layer. Finally, to verify the coverage design, we conducted indoor experiments in which 4 energy transmitters were employed by considering the scalability. The experimental results showed that the proposed system achieved 100% coverage so that numerous sensor nodes could be simultaneously activated in the office environment.

Chapter 6

Conclusion

6.1   Summary of the thesis

Power supplying for sensor nodes has been a critical issue in WSNs which are expected to perform many kinds of applications by employing a large number of sensor nodes. In WSNs, numerous sensor nodes are deployed in a target field and power-plugged nor battery-powered sensors are not preferable due to the installation cost and the limited lifetime, respectively. Energy harvesting from ambient energy is one of the solutions to activate sensor node without batteries. However, the ambient energy, such as light, can be easily involved by the surrounding environments. To alleviate this constraint, this thesis considered powering sensor nodes by microwave energy transmission and proposed battery-less sensor networks called wireless grid.

Chapter 2 introduced RFID systems as conventional systems of wireless energy transmission using microwave, compared the thesis with the other researches and illustrated the radio regulation of wireless energy transmission and WSNs. The critical issue of conventional RFID system was the coverage limitation due to path-loss attenuation of microwave.

Chapter 3 proposed multi-point wireless energy transmission scheme with carrier shift diversity to seamlessly extend the coverage of energy supply field and to activate a large number of sensor nodes arbitrarily distributed in indoor environments. To verify the effectiveness of the proposed scheme, this chapter also gave theoretical analysis on the RF received power and conducted indoor experiments to validate the effectiveness of the proposed system in terms of the RF propagation. In the experiments, RF received power was observed by using 2 transmitters. In addition, we compared the received power distribution and the coverage performance of different energy transmission schemes including conventional single-point, simple multi-point and our proposed multi-point

scheme. To easily observe the effect of standing-wave caused by multipath and interference between multiple transmitters, the measurements were performed in both horizontal and vertical planes and their corresponding simulations were also done in free space and 3 paths conditions. The results showed that standing-wave due to multipath and interference between multiple transmitters were dominant in the single-point scheme and in the simple multi-point scheme respectively. On the other hand, in the proposed multi-point scheme, the effect of standing-wave created by multipath and interference between multiple wave sources could be mitigated. In this experimental environment, the maximum available values of required power in the proposed scheme in horizontal and vertical planes were, respectively, 18.2 dB and 25.6 dB higher than those of the single-point scheme while the gain was 8.4 dB in free space simulation.

Chapter 4 provided the design concept of battery-less sensor nodes, developed real battery-less sensor nodes by off-the-shelf devices and conducted indoor experiments using the developed sensor node to validate the effectiveness of the proposed system in terms of the activation possibility of the battery-less sensor node. The developed sensor node with the duty cycle of 1 s consumed 140 μW while 400 μW was required to activate the sensor node by taking into account the RF/DC conversion efficiency of 35%. In the experiments, the RF received power and the activation of the sensor node were simultaneously observed by employing 2 transmitters. The experimental results showed that the coverage of single-point and simple multi-point energy transmission were limited to 84.4% and 83.7% respectively, while the proposed scheme achieved 100% coverage.

Chapter 5 provided design criteria of wireless energy transmission coverage in real indoor environments, implemented wireless grid into a real office environment with the developments of wireless energy transmitters, battery-less sensor nodes and wireless sensor network, and conducted indoor experiments to verify the activation of battery-less sensor nodes in a real indoor environment. The energy transmitters were embedded in LED ceiling lights to easily introduce the wireless energy transmission system. In addition, the Tx antenna and polarization were designed to realize a seamless coverage in 2-D space. The battery-less sensor nodes were extended from the development in Ch. 4. In the experiments, 4 transmitters were employed and the activation was observed at the height of desks among the transmitters. The experimental results showed that the proposed multi-point scheme achieved 100% coverage of the activation in 2.13 m × 1.91 m space.

By the fundamental analyses and researches in Chs. 3 and 4, the effectiveness of the proposed multi-point scheme was validated and by the extending investigations in Ch. 5, the thesis demonstrated the feasibility of battery-less sensor networks in indoor environments.

6.2 Suggestion for future works

There are still several remaining challenges.

- Miniaturization of sensor node:
  Because sensor nodes are required to be deployed anywhere such as on human skin for medical applications, the miniaturization should be taken into account. In the developed sensor node, the biggest component is the power receiving antenna. One of the most critical solutions is employing print antenna technology like ID tags in RFID sytems. In addition, the 920 MHz band was employed for both energy receiving and data communication in this thesis. However, in the developed sensor nodes, there were two antennas each for the energy receiving and the data communication. In the future, the two antennas should be integrated to miniaturize the sensor node.

- Increasing link margin:
  Chapter 5 mentioned that the link margin should be designed for the mitigation of received power due to multipath, shadowing and polarization mismatch. In particular, the received power can be easily affected by multipath in the area, where only a small number of transmitters have an influence to the power distribution, such as the edge of the grid. In order to increase the link margin, wireless grid can still improve the received power or the consumed power of sensor node. To increase the minimum received power, the density of Tx point should be increased or Tx antenna directivity should be more carefully designed to improve the uniformity of the power distribution. Increasing the density results in decreasing the multipath effect at the expense of system cost. Designing the antenna directivity in accordance with the environment results in improvement of the uniformity but low versatility. To decrease the required power, duty cycle of the data transmission should be increased. Increasing the duty cycle results in low consumed power of the sensor node but also low performance of WSNs. Therefore, proper solution should be determined in accordance with the applications of WSNs. In addition, more detailed link budget and antenna design should be taken into account in the future.

- Implementation of wireless grid for different scenarios:
  The implemented system focused on the LED control system using human detection sensors. The power consumption of the human detection sensor is several μW and the duty cycle of sensor node was 1 s. However, the developed sensor node cannot activate mW-consumed

sensors because the sensor itself was still active in the sleep mode. Therefore, if consumed power of sensor itself is too large to activate sensor node, sensor itself should be also configured to sleep mode and the power consumption of the sensor node should be designed by adjusting the duty cycle. Furthermore, the data communication network should be designed in accordance with the application demand, i.e. low delay time, low error rate and a large number of sensor nodes.

- Battery-less sensor nodes with energy harvesting:
  This thesis demonstrated feasibility of battery-less sensor networks using microwave energy transmission. Depending on the environments, energy harvesting from ambient energy may be more effective to activate sensor nodes. In order to more stably activate battery-less sensor nodes, hybrid of microwave energy transmission and energy harvesting should be considered in the future.

Appendix I

List of Publications

I.1   Journal papers

- D. Maehara, G. K. Tran, K. Sakaguchi, K. Araki, M. Furukawa, "Experiment Validating the Effectiveness of Multi-point Wireless Energy Transmission with Carrier Shift Diversity," *IEICE Trans. on Commun.,* vol. E97-B, no. 09, pp.1928-1937, Apr. 2014.

- D. Maehara, G. K. Tran, K. Sakaguchi, K. Araki, "Experimental Study on Battery-less Sensor Network Activated by Multi-point Wireless Energy Transmission," *IEICE Trans. on Commun.,* vol. E99-B, no.04, Apr. 2016.

I.2   International conferences

- D. Maehara, G. K. Tran, K. Sakaguchi, K. Araki, T. Miyamoto, M.Furukawa, "Experimental Study on Multi-point Wireless Energy Transmission at 950MHz Band," in Proc. *IEEE ISSSE2012,* Oct. 2012.

- D. Maehara, R. Akai, G. K. Tran, K. Sakaguchi, S. Sampei, K. Araki, H. Iwai, "Experiment on Battery-less Sensor Activation via Multi-point Wireless Energy Transmission," in Proc. *IEEE PIMRC2013,,* pp. 2336 - 2340, Sep. 2013.

- D. Maehara, G. Matsushita, Y. Kuki, K. Sakaguchi, S. Sampei, K. Araki, "[Requested Talk] Development of Battery-less Sensor Networks for LED Light Control System," in *IEICE Technical Report, (SmartCom2014,)* SR2014-78, vol. 114, no. 284, pp. 109-116, Oct. 2014.

I.3 Domestic conferences

- D. Maehara, K. Mizutani, K. Sakaguchi, K. Araki, T. Shirato, M. Furukawa, T. Miyamoto, M. Negishi, "Techniques for avoidance of standing wave problem in wireless power transmission at 950MHz band," in Proc. *IEICE General Conference,* B-1-3, Mar. 2011.

- D. Maehara, K. Sakaguchi, K. Araki, T. Miyamoto, M. Furukawa, T. Shirato, "Experimental Study on Multi-point Wireless Energy Transmission at 950 MHz band," in *IEICE Technical Report,* AP2011-201, vol. 111, no. 487, pp. 13-17, Mar. 2011.

- D. Maehara, R. Akai, K. Sakaguchi, S. Sampei, K. Araki, H. Iwai, "Experimental Verification of Battery-less Sensor Activation via Multi-point Wireless Energy Transmission," in *IEICE Technical Report,* AP2013-7, vol. 113, no. 3, pp. 37-42, Apr. 2013.

I.4 Awards

- Best Paper Award from IEICE Technical Committee on Software Radio in 2013.

- Best Paper Award from IEICE Communication Society in 2014.

Appendix II

Hardware development

This appendix gives technical supports for the development and shows the details of the development of wireless energy transmitter, sensor node and access point.

II.1   Wireless energy transmitter

For the sake of simplicity, Ch. 5 did not mention the structure of power supplying, the method of frequency control and the reference oscillator. Figure II.1 shows the detailed structure of the developed wireless energy transmitter. In the figure, green, blue and red lines denote cables for power supplying, data communication and RF respectively. AC/DC and DC/DC converters are employed for activating the RF devices, e.g. the synthesizer (3 V), the amplifier (3 V and 4 V), and the internal oscillator (5 V).

To operate the synthesizer [81], 10 MHz reference signal should be supplied since the synthesizer generates the required frequency by Phase Locked Loop (PLL) method. In the experiments, especially in the case of MP, all the synthesizers were synchronized by the external oscillator to clearly observe the interference, while the internal oscillators, in which the frequency of 10 MHz was set by adjusting the variable resistance, could be used to perform CSD. In addition, the synthesizer is controlled by a serial communication called Microwire. Texas Instruments (TI), which is a supplier of the synthesizer, provides a support device for converting Universal Serial Bus (USB) to Microwire for ease of controlling by PC. However, the device is only supported for an Operating System (OS) of Windows, while the developed energy transmitter employs the Linux CPU board for ease of remote operation from the server. Therefore, in order to perform USB/Microwire conversion, USB/Serial converter, whose main chip is FT232RL and drivers for Linux with C language

are supplied by [86], is employed to create arbitrary waveform. Figure II.2 shows the diagram of writing the frequency data to the chip of the synthesizer. The chip is controlled by 11 24-bit registers. Chip Enable (CE) must be always applied. Latch Enable (LE) must be applied before 1 data sequence of a register. The DATA can be generated by the software of CodeLoader 4 [87] supplied by TI and can be written upon the rising edge of CLocK (CLK). These 4 lines are controlled by the USB/Serial converter connected with the Linux CPU board to write the frequency.

In this development, since LED light had enough space to contain the transmitter, the size of the transmitter was out of scope and the evaluation boards are usually employed. However, the energy transmitter can be expected to be dramatically miniaturized by making original board. Furthermore, to design low-energy wireless energy transmitter, the output power of the synthesizer might reach saturation region of the amplifier. Therefore, BPF is employed to eliminate spurious.

II.2   Sensor node and access point

For the sake of simplicity, Ch. 4 and 5 did not show the receiver architecture and the development environment. Figure II.3 shows the data communication of the sensor node. The RF module including RF transceiver and MCU was custom-made by Tessera Technology to connect between MCU and sensors and to miniaturize its size, and was originally produced as [74] in which the MCU is supplied by Renesas Electronics [29]. The receiver also has the same MCU and RF transceiver implemented into the USB dongle [89], which is employed as RF module for access link in Ch. 5. In the development, the sensor node transmits its sensing data in addition to its ID. It is noted that human detection sensor is only activated in the experiments of Ch. 4 and 5 while the other sensors are equipped for the future application of BEMS. The receiver transmits the received data and the RSSI to PC by serial communication.

The program of the MCU can be edited and built by a software of CubeSuite+ [88] which is supplied by Renesas Electronics and Application Programming Interface (API) functions for controlling RF transceiver is supplied by Tessera Technology. The RF module can be programmed and emulated on the development kit [74] connected to PC through USB cable. In the software, we can overwrite its own ID, the duty cycle by a step of 0.5 s, the transmit power of the data communication from −13 dBm to 13 dBm by a step of 1 dB, the center frequency from 922.5 MHz to 927.9 MHz, 10-bit A/D or digital conversion, and the number of the retransmission in the case when the channel is not available.

In the development of AP, as mentioned in Ch. 5, the CPU board plays a role of connection of RF

modules for access and backhaul links. Both the modules can transmit and receive the data through serial communication with the CPU board. For the program of the development, Linux shell script is employed on the CPU board and 2 programs are created for sink and relay nodes respectively in order to realize the network architecture as shown in Fig. 5.5. It is noted that the developed system dealt with 10 sensor nodes and 3 APs (2 hops) at most. Future development is required to perform large scale network.
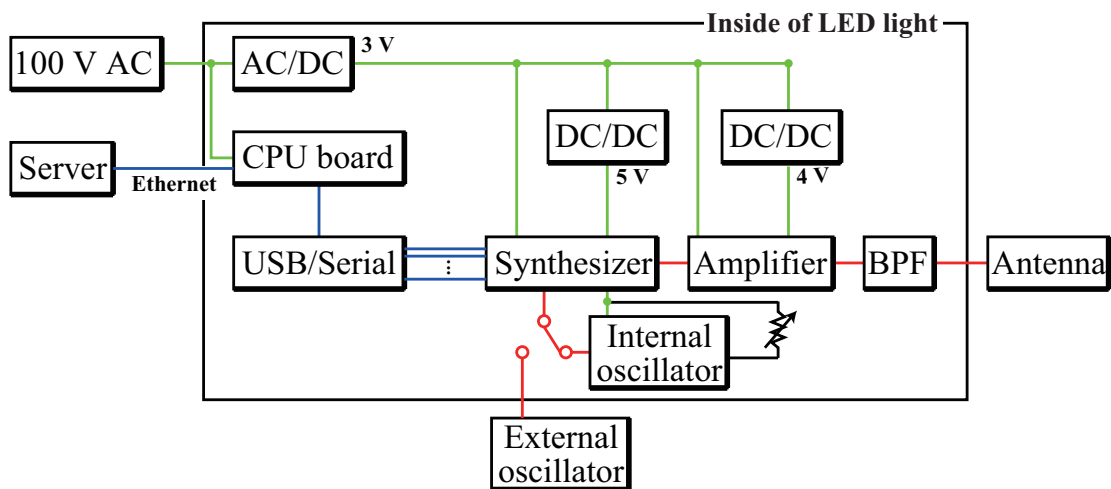
Figure II.1   Detailed structure of wireless energy transmitter.
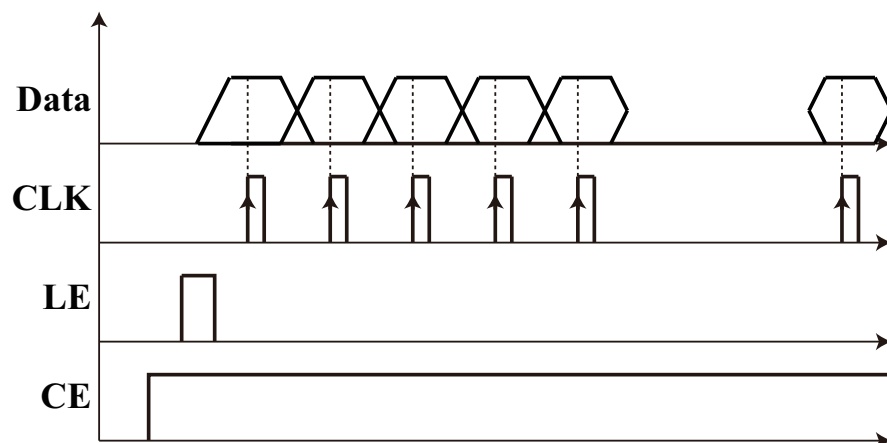
Figure II.2   Writing data for frequency setup.

PC

| ID |
| RSSI |
| Human detection |
| Temperature |
| Illuminance |

Serial

RF module

MCU ⟷ RF transceiver

Rx

Tx

Sensor unit

| Human detection |
| Temperature |
| Illuminance |

RF module

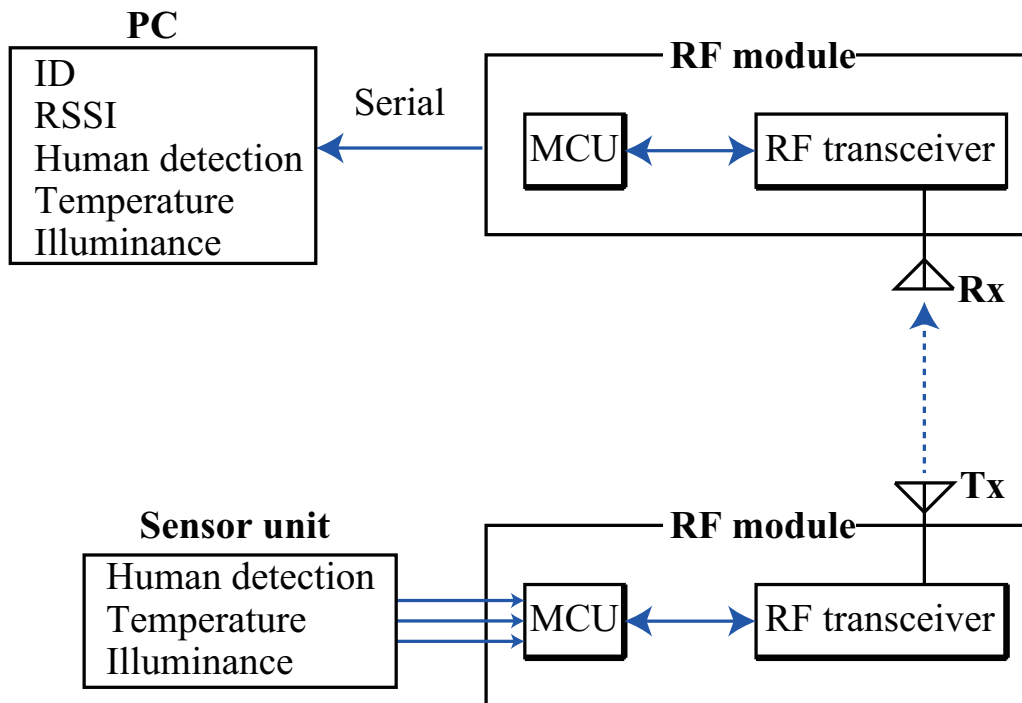MCU ⟷ RF transceiver

Figure II.3 Data communication of sensor node.

Reference

[1] N. D. Lane, E. Miluzzo, H. Lu, D. Peebles, T. Choudhury, A. T. Campbell, "A Survey of Mobile Phone Sensing," *IEEE Commun. Mag.,* vol. 48, no. 9, pp. 140-150, Sep. 2010.

[2] Arduino, [Online] Available: https://www.arduino.cc/

[3] Raspberry Pi, [Online] Available: https://www.raspberrypi.org/

[4] TSENSORS, "The TSensors Roadmap," *TSensors summit,* Oct. 2013.

[5] D. Evans, "The Internet of Things How the Next Evolution of the Internet Is Changing Everything," *Cisco Internet Business Solutions Group,* Apr. 2011.

[6] L. M. Borges, F. J. Velez, and A. S. Lebres, "Survey on the Characterization and Classification of Wireless Sensor Networks Applications," *IEEE Commun. Surveys & Tutorials,* Apr. 2014.

[7] "Smart Metering for Electric and Gas Utilities," *An Oracle White Paper,* Jan. 2011.

[8] V. C. Gungor, D. Sahin, T. Kocak, S. Ergut, C. Buccella, S. Member, C. Cecati, Gerhard P. Hancke, "A Survey on Smart Grid Potential Applications and Communication Requirements," *IEEE Trans. on Industrial Informatics,* vol. 9, no. 1, pp. 28-42, Feb. 2013.

[9] C. Talon, "Next-Generation Building Energy Management Systems," *Intel White Paper,* 2015.

[10] D. Han, J. Lim, "Smart Home Energy Management System using IEEE 802.15.4 and ZigBee," *IEEE Trans on Consumer Electronics,* vol. 56, no. 3, pp. 1403-1410, Aug. 2010.

[11] M. Li, H. Lin, "Design and Implementation of Smart Home Control Systems Based on Wireless Sensor Networks and Power Line Communications," *IEEE Trans. on Industrial Electronics,* vol. 62, no. 7, pp. 4430-4442, Jul. 2015.

[12] H. Ochiai, H. Ishizuka, Y. Kawakami, H. Esaki, "A DTN-Based Sensor Data Gathering for Agricultural Applications," *IEEE Sensor Journal,* vol. 11, no. 11, pp. 2861-2868, Nov. 2011.

[13] A. Pantelopoulos, N. G. Bourbakis, "A Survey on Wearable Sensor-Based Systems for Health Monitoring and Prognosis," *IEEE Trans. on Syetems, Man, and Cybernetics, Part C: Applications and Reviews,* vol. 40, no. 1, pp. 1-12, Jan. 2010.

[14] "Wearable Technology," *An Oracle White Paper,* Apr. 2015.

[15] C. Yang, H. Shao, "WiFi-Based Indoor Positioning," *IEEE Commun. Mag.,* vol. 53, no. 3, pp. 150-157, Mar. 2015.

[16] J. Macaulay, L. Buckalew, G. Chung, "INTERNET OF THINGS IN LOGISTICS," *A collaborative report by DHL and Cisco on implications and use cases for the logistics industry,* 2015.

[17] Y. Chen, J. Hwang, "A Power-Line-Based Sensor Network for Proactive Electrical Fire Precaution and Early Discovery," *IEEE Trans. on Power Delivery,* vol. 23, no. 2, pp. 633 - 639, Apr. 2008.

[18] M. Radford, "Airport Security White Paper," *Blighter Surveillance Systems,* BSS-1502, 2015.

[19] I. N. Junejo, X. Cao, H. Foroosh, "Autoconfiguration of a Dynamic Nonoverlapping Camera Network," *IEEE Trans. on System, Man, and Cybernetics,* vol. 37, no. 4, pp. 803-816, Aug. 2007.

[20] *IEEE Standard for Local and metropolitan area networks - Part 15.4: Low-Rate Wireless Personal Area Networks (LR-WPANs)*, IEEE Std. 802.15.4-2011, 2011.

[21] *IEEE Standard for Local and metropolitan area networks–Part 15.4: Low-Rate Wireless Personal Area Networks (LR-WPANs) Amendment 3: Physical Layer (PHY) Specifications for Low-Data-Rate, Wireless, Smart Metering Utility Networks,* IEEE Std. 802.15.4g-2012, 2012.

[22] *IEEE Standard for Local and metropolitan area networks–Part 15.4: Low-Rate Wireless Personal Area Networks (LR-WPANs) Amendment 1: MAC sublayer,* IEEE Std. 802.15.4e-2012, 2012.

[23] *IEEE Standard for Information technology– Local and metropolitan area networks– Specific requirements– Part 15.1a: Wireless Medium Access Control (MAC) and Physical Layer (PHY) specifications for Wireless Personal Area Networks (WPAN),* IEEE Std. 802.15.1, 2015.

[24] STMicroelectronics, Accelerometers, Temperature sensors, [Online] Available. http://www.st-japan.co.jp/web/en/catalog/sense_power/FM89

[25] Intersil, Optoelectronics, [Online] Available. http://www.intersil.com/en/parametricsearch.html?g=optoelectronics&sg=ambient-light-and-proximity-sensors♯g=optoelectronics

[26] STMicroelectronics, Ultra low power MCUs, [Online] Available. http://www.st.com/web/catalog/mmc/FM141/SC1544

[27] Maxim Integrated, Low-power microcontrollers, [Online] Available. https://para.maximintegrated.com/en/results.mvp?fam=micros&1233=Low%20Power

[28] Analog Devices, MEMS accelerometers, Temperature sensor, [Online] Available. http://www.analog.com/en/index.html

[29] *Datasheet* RL78/G13, Renesas, [Online]. Available: http://www.renesas.com/products/mpumcu/rl78/Documentation.jsp

[30] *Datasheet* MSP430F1101A, Texas Instruments [Online]. Available: http://www.tij.co.jp/lsds/ti_ja/microcontrollers_16-bit_32-bit/msp/products.page

[31] *Datasheet* MAXQ617, Maxim, [Online]. Available: https://para.maximintegrated.com/en/search.mvp?fam=micros&1233=Low%20Power

[32] *Datasheet* CC1120, Texas Instruments, [Online]. Available: http://www.ti.com/product/CC1120/datasheet

[33] *Datasheet* CC2500, Texas Instruments, [Online]. Available: http://www.ti.com/product/CC2500/description

[34] *Datasheet* ML7396A/B/E, LAPIS semiconductor, [Online]. Available: http://www.symmetron.ru/news/files/pdf/rohm/rohm-lapis-ML7396.pdf

[35] *Datasheet* TCM300, Enocean, [Online]. Available: https://www.enocean.com/en/enocean_modules/tcm-300-data-sheet.pdf

[36] *Datasheet* ADF7023, Analog Devices, [Online]. Available: http://www.analog.com/static/imported-files/data_sheets /ADF7023.pdf

[37] *Datasheet* blueNRG, STMicroelectronics, [Online]. Available: http://www.st.com/st-web-ui/static/active/en/resource/technical/document/datasheet/ DM00092683.pdf

[38] D. Brunelli, C. Moser, L. Thiele, and L. Benini, "Design of a Solar-Harvesting Circuit for Batteryless Embedded Systems," *IEEE Trans. Circuits and Systems I*, Vol.56, No.11, pp.2519-2528, Feb. 2009.

[39] *Information technology – Home Electronic Systems (HES) – Part 3-10: Wireless Short-Packet (WSP) protocol optimized for energy harvesting – Architecture and lower layer protocols*, ISO/IEC Std. 14543-3-10, 2012.

[40] N. Shinohara, "Power Without Wires," *IEEE Microwave Mag.,* vol. 12, pp. S64-S73, Dec. 2011.

[41] *Identification cards – Contactless integrated circuit cards – Proximity cards –* ISO/IEC Std. 14443 , 2008.

[42] A. Kurs, A. Karalis, R. Moffatt, J. D. Joannopoulos, P. Fisher, M. Soljacic, "Wireless Power Transfer via Strongly Coupled Magnetic Resonances," *Science Mag.,* vol. 317, no. 5834, pp. 83-86, Jun. 2007.

[43] S. Li, C. C. Mi, "Wireless Power Transfer for Electric Vehicle Applications," *IEEE journal of Emerging and Selected Topics in Power Electronics,* vol. 3, pp. 4-17, Mar. 2015.

[44] H. Matsumoto, "Research on solar power satellites and microwave power transmission in Japan," *IEEE Microwave Mag.,* vol. 3, pp. 36-45, Dec. 2002.

[45] N. Tesla, "The Transmission of Electric Energy Without Wires," *Electrical World and Engineer,* Mar. 1904.

[46] N. Tesla, "Experiments with Alternate Current of High Potential and High Frequency," *McGraw-Hill Publishing Company,* 1904.

[47] W. C. Brown, "Free-space Transmission," *IEEE Spectrum,* vol. 1, no. 10, 1964.

[48] M. Roberti, "The History of RFID Technology," *RFID Journal,* Jan. 2005.

[49] N. Shinohara, "Power Without Wires," *IEEE Microwave Mag.,* vol. 12, pp. S64-S73, Dec. 2011.

[50] P. E. Glaser, "Power from the Sun: Its Future," Science, vol. 162, no. 3856, pp. 857-861, Nov. 1968.

[51] D. M. Dobkin, "The RF in RFID," Newnes, 2008.

[52] EPCglobal, "Specification for RFID Air Interface Protocol for Communications at 860 MHz - 960 MHz" *EPC ^{TM} Radio-Frequency Identity Protocols Class-1 Generation-2 UHF RFID Protocol,* Version 2.0.1, Apr. 2015.

[53] C. R. Valenta and G. D. Durgin, "Harvesting Wireless Power Survey of Energy-Harvester Conversion Efficiency in Far-Field, Wireless Power Transfer Systems," *IEEE Microwave Magazine,* vol.15, pp.108-120, Jun. 2014.

[54] N. Shinohara, "Rectennas for microwave power transmission," *IEICE Electronics Express,* vol. 10, no. 21, Nov. 2013.

[55] C. R. Valenta, M. M. Morys, G. D. Durgin, "Theoretical Energy-Conversion Efficiency for Energy-Harvesting Circuits Under Power-Optimized Waveform Excitation," *IEEE Trans. on Microwave Theory and Techniques,* vol. 63, no. 5, pp. 1758-1767, Apr. 2015.

[56] S. Yamashita, N. Imoto, T. Ichihara, K. Yamamoto, T. Nishio, M. Morikura, Naoki Shinohara, "Implementation and Feasibility Study of Co-channel Operation System of Microwave Power Transmissions to IEEE 802.11-Based Batteryless Sensor," *IEICE Trans. on commun.,* vol. E97-B, no. 9 pp.1843-1852, Sep. 2014.

[57] N. Imoto, S. Yamashita, T. Ichihara, K. Yamamoto, T. Nishio, M. Morikura, Naoki Shinohara, "Experimental Investigation of Co-channel and Adjacent Channel Operations of Microwave Power and IEEE 802.11g Data Transmissions," *IEICE Trans. on commun.,* vol. E97-B, no. 9 pp.1835-1842, Sep. 2014.

[58] R. Shigeta, T. Sasaki, D. M. Quan, Y. Kawahara, R. J. Vyas, M. M. Tentzeris, T. Asami, "Ambient RF Energy Harvesting Sensor Device With Capacitor-Leakage-Aware Duty Cycle Control," *IEEE Sensors Journal,* Aug. 2013.

[59] Y. Li and V. Jandhyala, "Design of Retrodirective Antenna Arrays for Short-Range Wireless Power Transmission," *IEEE Trans. on Antennas and Propagation,* vol. 60, no. 1, Jan. 2012.

[60] S. Rahimizadeh, S. Korhummel, B. Kaslon, Z. Popovic, "Scalable adaptive wireless powering of multiple electronic devices in an over-moded cavity," *IEEE Antenna and Propagation Magazine,* vol. 53, no. 1, Feb. 2011.

[61] Powercast, [Online]. Available: http://www.powercastco.com/

[62] Nihon Dengyo Kosaku, [Online]. Available: http://www.den-gyo.com/english/

[63] KDDI cooperation, "New Investments in Two Technology Companies via KDDI Open Innovation Fund," News Release, 2015. [Online]. Available:
http://news.kddi.com/kddi/corporate/english/newsrelease/2015/01/27/besshi896.html

[64] Ossia, [Online]. Available: http://www.ossia.com/

[65] "950MHz-BAND RFID EQUIPMENT FOR PREMISES RADIO STATION," Association of Radio Industries and Businesses ARIB STD-T89, Jul. 2010.

[66] "950MHz-BAND RFID EQUIPMENT FOR SPECIFIED LOW POWER RADIO STATION," Association of Radio Industries and Businesses ARIB STD-T90, Jul. 2010.

[67] "950MHz-BAND TELEMETER, TELECONTROL AND DATA TRANSMISSION RADIO EQUIPMENT FOR SPECIFIED LOW POWER RADIO STATION," Association of Radio Industries and Businesses ARIB STD-T96, Jul. 2010.

[68] "950MHz-BAND RFID EQUIPMENT FOR CONVENIENCE RADIO STATION," Association of Radio Industries and Businesses ARIB STD-T100, Jul. 2010.

[69] "920MHz-BAND RFID EQUIPMENT FOR PREMISES RADIO STATION," Association of Radio Industries and Businesses ARIB STD-T106, Feb. 2012.

[70] "920MHz-BAND RFID EQUIPMENT FOR SPECIFIED LOW POWER RADIO STATION," Association of Radio Industries and Businesses ARIB STD-T107, Feb. 2012.

[71] "920MHz-BAND TELEMETER, TELECONTROL AND DATA TRANSMISSION RADIO EQUIPMENT," Association of Radio Industries and Businesses ARIB STD-T108, Feb. 2012.

[72] "Regulatory status for using RFID in the EPC Gen 2 band (860 to 960 MHz) of the UHF spectrum," Global Standard One (GS1), Oct. 2014.

[73] *Datasheet* P1110EVB, Powercast, [Online]. Available: http://www.powercastco.com/PDF/P1110-EVB.pdf

[74] *Datasheet* TK-RL7023+SB-L, Tessera Technology, [Online]. Available: http://www.tessera.co.jp/tk-rl7023+sb.html

[75] E. Falkenstein, M. Roberg, and Z. Popovic, "Low-power Wireless Power Delivery," *IEEE Trans. on Microwave Theory and Techniques*, vol.60, no.7, pp.2277-2286, Jul. 2012.

[76] T. Paing, J. Shin, R. Zane, and Z. Popovic, "Resistor Emulation Approach to Low-Power RF Energy Harvesting," *IEEE Trans. on Power Electrons*, vol.23, no.3, pp.1494-1501, Jul. 2008.

[77] T. Yu, Y. Kuki, G. Matsushita, D. Maehara, S. Sampei, K. sakaguchi, "Deployment of LED light control system using battery-less wireless human detection sensor networks," in Proc. *IEEE RFID-TA 2015*, pp. 14-19, Sep. 2015.

[78] *AC and/or DC-supplied electronic control gear for tubular fluorescent lamps - Performance requirements* IEC Std. 60929 , May 2014.

[79] *Digital addressable lighting interface* IEC Std. 62386, under deliberation.

[80] RF-ATCP013, Mitsubishi Electric, [Online]. Available: http://www.mitsubishielectric.co.jp/device/rfid/catalog/pdf/catalog5.pdf

[81] *Datasheet*, LMX2531LQ1742 Evaluation Board, Texas Instruments, [Online] Availlable: http://www.ti.com/lit/ug/snau033/snau033.pdf

[82] *Datasheet,* RF3858PCK-410, RFMD, [Online] Availlable: http://www.rfmd.com/store/downloads/dl/file/id/27936/rf3858_data_sheet.pdf

[83] *Datasheet,* OpenBlocks A7, Plathome, [Online] Availlable: http://ftp.plathome.co.jp/pub/OBSA7/Documents/OBSA_UsersGuide_1.2.0.pdf

[84] *Datasheet,* EKMB1101111, Panasonic, [Online] Availlable:
http://www3.panasonic.biz/ac/e/dl /
catalog /index.jsp?series_cd=2480&part_no=EKMB1101111

[85] Skyley NETWORKS, [Online]. Available:
http://www.skyley.com/english/index.html

[86] *Datasheet* FT232R, FTDI, [Online]. Available:
http://www.ftdichip.com/Support/Documents/DataSheets/ICs/DS_FT232R.pdf

[87] *User's Guide*, CodeLoader 4 Operating Instructions, Texas Instruments, [Online] Availlable:
http://www.ti.com/lit/ug/snau083a/snau083a.pdf

[88] CubeSuite+, Renesas Electronics, [Online] Availlable:
http://www.renesas.com/products/tools/ide/csp/index.jsp

[89] *Datasheet* RL7023 Stick-L, Tessera Technology, [Online]. Available:
http://www.tessera.co.jp/rl7023stick.html